Cognitive and Autonomous Software-Defined Open Optical Networks

Politecnico di Torino

ScuDo
Scuola di Dottorato ~ Doctoral School
WHAT YOU ARE, TAKES YOU FAR

Doctoral Dissertation
Doctoral Program in Telecommunications Engineering (35^{th}cycle)

Cognitive and Autonomous Software-Defined Open Optical Networks

By

Giacomo Borraccini

******

Supervisor:
Prof. Vittorio Curri

Doctoral Examination Committee:
Prof. Metodi Plamenov Yankov, Referee, Technical University of Denmark
Prof. Oskars Ozolins, Referee, Research Institutes of Sweden
Prof. Paolo Serena, Università degli Studi di Parma
Prof. Roberto Proietti, Politecnico di Torino
Dr. Antonio Napoli, Infinera

Politecnico di Torino
2023

Declaration

I hereby declare that, the contents and organization of this dissertation constitute my own original work and does not compromise in any way the rights of third parties, including those relating to the security of personal data.

Giacomo Borraccini
2023

* This dissertation is presented in partial fulfillment of the requirements for **Ph.D. degree** in the Graduate School of Politecnico di Torino (ScuDo).

To my family

Acknowledgements

As often happens in the world of research (almost always), the realization of this work saw the possibility of evolving in infinite different ways in each moment that took part in its process. More often than not, the free will puts us in front of this chaotic vision from which it is not easy to extricate ourselves, obscuring the achievement of those small goals we set or, more simply, those short but intense moments of happiness. In addition to our ability to hinder ourselves, everyday there are unexpected difficulties, challenges and events that inevitably contribute to our present and future. In this continuous flow that stubbornly pushes us forward without stopping, I wanted to warmly thank those who have helped me on this journey up to now, interpreting what was happening and trying to define the next steps, in work and in life. Also, there are many other people I would like to thank simply for making me who I am today, at the end of this cycle. In any case, I am extremely grateful to all of them and briefly mention them in this way. I would like to underline that the order in which these thanks are mentioned is a pure artifice which allows us to maintain clarity of communication. For me, their thinking coexists in the same unique dimension.

First of all, I would like to thank Prof. Vittorio Curri for the opportunity and the trust he has given me, for his teachings and vision of the world of research, and for the style with which challenges are faced. I would mention also the researchers of LINKS Foundation, Stefano Straullu, Francesco Aquilino and Antonino Nespola, with who we carried out bunch of experiments, spending a lot of time and effort, but also having fun and achieving many satisfactions. I want to thank all my fellow adventurers during the PhD course, for the good time spent together, the jokes, the disagreements, the travels: Andrea D'Amico, Renato Ambrosone, Rocco D'Ingillo, Bruno Vinicius, Rasoul Sadeghi, Elliot London, Fehmida Usmani, Ihtesham Khan, Umar Masood, Emanuele Virgillito, Hasan Awad, and Alessio Ferrari.

Next, I want to thank my lifelong friends, both from college, music and high school. Each of us has taken a different way, but despite this, in the few moments in which we manage to hear each other, every word or look is always the confirmation that in this chaos there are also some singularities: Giorgio, Manfredi, Roberta, Paolo, Marco, Arian, Paul, Lorenzo, Arianna, and Giulio.

Finally, I want to thank those who are the constants of my life, my beloved family, to whom I dedicate this work.

Abstract

Driven by the increasing and greedy Internet data traffic request, optical network operators are working to satisfy this need, improving the already installed resources, or updating them with the introduction of new technological discoveries. In this context, boosted by the progressive process of opening and standardization, the most relevant support for service capacity increase and system management is conferred by optical network automation, implying the implementation of Software-Defined Networking (SDN) approaches. Another important characteristic for an efficient usage of optical networks is the capability of the infrastructure to be agnostic with respect to the adopted vendor equipment. Starting from the last decade, cognition has been introduced and theorized as an emerging feature of the next generation of optical networks, implying the autonomous and prompt control of a network at each abstraction layer operating decisions and strategies based on the processing of information related to the status of the system. The response to the increasing complexity of the infrastructure is given by the possibility to probe the condition of the network through monitoring devices and to efficiently analyze the extracted information using flexible software modules. In addition, the proper control, based on an accurate physical layer modeling, of active network elements, such as optical amplifiers – Erbium-Doped Fiber Amplifiers (EDFAs) or Raman amplifiers – and Re-configurable Optical Add & Drop Multiplexers (ROADMs), results to be a key point within the described scenario.

The aim of this work is to deepen cognition and automation applied on optical networks at the physical layer, defining vendor agnostic control procedures and architectures capable of autonomously maximize the capacity of the optical infrastructure. The latter implies a larger exploitation of the installed resources, even in case of lack of knowledge about equipment specifications. In particular, it has been proved that the performance of a ROADM-to-ROADM optical link can be optimized maximizing and flattening the Quality-of-Transmission (QoT) over all the channels

propagating through the link. The developed methodologies have been applied to different use-cases, properly defining each architecture of the corresponding controller: single-span Raman amplifier system; multi-span EDFA-amplified Optical Line System (OLS); complete optical network with triangular and linear topology. The adopted methodology that brings the considered system to maximize the its capacity can be summarized with a two-step optimization process applied during the provisioning phase of an optical network. The core of this approach is the use of a physical layer model able to simulate the behavior of the considered system. Firstly, the physical layer is completely characterized retrieving in-field the needed features through the available telemetry in order to estimate the corresponding physical layer parameters. Then, on the basis of the tuned physical layer model, the working point of the system is properly designed. During the first step, the system is set under defined conditions and the physical layer model is tuned in order to match the optical transmission behavior reported by the telemetry, then according to the network controller targets, the working point of the system is optimized manipulating the softwarized representation of the optical system.

As a continuation of the research activity, the orchestration and the management of an optical network within the control system can be improved in terms of flexibility and adaptability with respect to several scenarios. Also, ad-hoc artificial intelligence techniques can be implemented and their impact investigated within various frameworks in order to face soft/hard failures and support the system reaction with proper automatic re-optimization strategies.

Contents

List of Figures

List of Tables

List of Abbreviations

ACO	Analog Coherent Optics
Adam	Adaptive Moment Estimation
ADC	Analog-to-Digital Converter
ANN	Artificial Neural Network
API	Application Programming Interface
ASE	Amplified Spontaneous Emission
AWGN	Additive White and Gaussian Noise
B2B	Back-to-Back
BER	Bit Error Rate
BST	Booster
CAGR	Compound Annual Growth Rate
CAPEX	Capital Expenditures
CD	Chromatic Dispersion
CFP	C Form-factor Pluggable
CLI	Command-Line Interface
CMA-ES	Co-variance Matrix Adaptation Evolutionary Strategy
CPE	Carrier Phase Estimation
CUT	Channel Under Test
CW	Continuous Wave
DAC	Digital-to-Analog Converter
DCO	Digital Coherent Optics
DFB	Distributed Feed-Back

DGE	Dynamic Gain Equalization
DP	Dual Polarization
DRA	Distributed Raman Amplifier
DSP	Digital Signal Processing
DT	Digital Twin
DWDM	Dense Wavelength Division Multiplexing
EDFA	Erbium-Doped Fiber Amplifier
EON	Elastic Optical Network
FEC	Forward Error Correction
GFF	Gain Flattening Filter
GGN	Generalized Gaussian Noise
GN	Gaussian Noise
GNPy	Gaussian Noise Model in Python
HFA	Hybrid Raman-EDFA Amplifier
IEEE	Institute of Electrical and Electronics Engineers
IETF	Internet Engineering Task Force
ILA	In-Line Amplifier
IP	Internet Protocol
ITU	International Telecommunication Union
L-PCE	Light-Path Computation Engine
LOGO	Local-Optimization Global-Optimization
LP	Lightpath
MAE	Maximum Absolute Error
ML	Machine-Learning
MSA	Multi-Source Agreement
NE	Network Element
NETCONF	Network Configuration

NFV	Network Function Virtualization
NLI	Non-Linear Interference
NOS	Network Operating System
OADM	Optical Add-Drop Multiplexer
OCM	Optical Channel Monitor
OcNOS	Network Operating System for Telecom & Operators
ODE	Ordinary Differential Equation
ODL	OpenDayLight
OIF	Optical Internetworking Forum
OLC	Optical Line Controller
OLS	Optical Line System
ONC	Optical Network Controller
ONF	Open Networking Foundation
ONOS	Open Network Operating System
OONC	Open Optical Network Controller
OOS	Out-Of-Service
OPEX	Operational Expenditures
OSA	Optical Spectrum Analyzer
OSFP	Octal Small Form-factor Pluggable
OTDR	Optical Time Domain Reflectometer
PDG	Polarization-Dependent Gain
PDL	Polarization-Dependent Loss
PHY	Physical Layer
PLAON	Physical Layer Aware Optical Network
PLASE	Physical Layer Aware Simulation Environment
PM	Polarization Multiplexed
PMD	Polarization Mode Dispersion
PRE	Pre-amplifier
PSD	Power Spectral Density
QAM	Quadrature Amplitude Modulation
QoT	Quality-of-Transmission

QoT-E	Quality-of-Transmission Estimation
QPSK	Quadrature Phase Shift Keying
QSFP	Quad Small Form-factor Pluggable
QSFP-DD	Quad Small Form-factor Pluggable Double Density
RCU	Raman Control Unit
RDU	Raman Design Unit
ReLU	Rectified Linear activation Unit
REST	REpresentational State Transfer
RMSE	Root-Mean-Square Error
ROADM	Re-configurable Optical Add & Drop Multiplexer
RRC	Root-Raised Cosine
RSA	Routing and Spectrum Assignment
SD	Software-Defined
SDM	Space Division Multiplexing
SDN	Software-Defined Networking
SLSQP	Sequential Least Squares Programming
SMF	Single Mode Fiber
SNR	Signal-to-Noise Ratio
SRS	Distributed Raman Amplifier
SSH	Secure Shell
SSMF	Standard Single-Mode Fiber
TIP	Telecom Infra Project
TRX	Transceiver
VNI	Visual Networking Index
VOA	Variable Optical Attenuator
WDM	Wavelength Division Multiplexing
YANG	Yet Another Next Generation

List of Symbols

a	Fiber Core Radius
A	Rayleigh Scattering Slope Parameter
A_1	Independent Loss Coefficient Parameter
A_{eff}	Effective Area
A_{eff}^{ov}	Overlapping Effective Area
α	Loss Coefficient
B	Rayleigh Scattering Offset Parameter
B	EDFA Tilt Bandwidth
β	Mode-Propagation Constant
β_2	Chromatic Dispersion Coefficient
B_n	Noise Bandwidth
C_R	Raman Gain Coefficient
c_R	Normalized Raman Gain Coefficient
D	Dispersione Parameter
Δ	Core-Cladding Interface Relative Index Step
Δf	Frequency Shift
ΔG	Gain Ripple
ΔG_{OO}	On-Off Gain Maximum Deviation
ε	Tolerance
F	Generic Objective Function
f_0	EDFA Tilt Pivot Frequency

f	Frequency
G	Gain
γ	Non-Linear Coefficient
γ_R	Mode Intensity Raman Gain Coefficient
$\mathrm{G_{ASE}}$	ASE Power Spectral Density
G_{OO}	On-Off Gain
$\overline{G_{OO}}$	On-Off Gain Average
$\overline{G_{OO,cor}}$	On-Off Gain Average Correction Parameter
$\partial_{P^{\pm}_{opt}} \overline{G_{OO}}$	On-Off Gain Average Gradient vs. Perturbated Optimal Raman Pump Power
$\overline{G_{OO,opt}}$	On-Off Gain Average using Optimal Raman Pump Power Configuration
$\overline{G_{OO,opt\pm var}}$	On-Off Gain Average using Perturbated Optimal Raman Pump Power Configuration
GSNR	Generalized Signal-to-Noise Ratio
$\overline{\mathrm{GSNR}}$	Generalized Signal-to-Noise Ratio Average
σ_{GSNR}	Generalized Signal-to-Noise Ratio Standard Deviation
$\mathrm{G_{tar}}$	Gain Target
h	Planck Constant
κ	Rayleigh Back-Scattering Coefficient
K_{IR}	Infrared Absorption Parameter
k_{pol}	Polarization State
K_R	Raman Gain Coefficient Scaling Factor
K_{UV}	Ultraviolet Absorption Parameter
l	Lumped Loss
L_{eff}	Effective Length
L_S	Fiber Span Length
M	Cardinality

$m_{G_{OO}}$	On-Off Gain Linear Regression Angular Coefficient
$m_{G_{OO},cor}$	On-Off Gain Tilt Correction Parameters
n_1	Core Refractive Index
n_c	Cladding Refractive Index
NF	Noise Figure
n_{sp}	Spontaneous Emission Factor
OSNR	Optical Signal-to-Noise Ratio
P	Signal Power
P_{ASE}	Amplified Spontaneous Emission Noise Power
P_{NLI}	Non-Linear Interference Noise Power
P_{opt}	Optimal Raman Pump Power Configuration
$p\%$	Perturbation Percentage
P_R	Reflected Signal Power
P^{SAT}	Saturation Total Output Power
ρ	Roll-Off
R_s	Symbol Rate
$S_P^{\overline{G_{OO}}}$	On-Off Gain Average Sensitivity vs. Raman Pump Power
SNR_{NL}	Non-Linear Signal-to-Noise Ratio
T_{tar}	Tilt Target
V	Normalized Frequency
w	Optical Mode Radius
λ	Wavelength
z	Spatial Coordinate

List of Scientific Contributions

Peer-Reviewed Journals

1. **Giacomo Borraccini**, Stefano Straullu, Stefano Piciaccia, Alberto Tanzi, Antonino Nespola, Gabriele Galimberti, Vittorio Curri. "Autonomous Raman amplifiers using standard integrated network equipment." IEEE Photonics Technology Letters 33.16 (2021): 868-871.

2. Andrea D'Amico, Stefano Straullu, **Giacomo Borraccini**, Elliot London, Stefano Bottacchi, Stefano Piciaccia, Alberto Tanzi, Antonino Nespola, Gabriele Galimberti, Scott Swail, Vittorio Curri. "Enhancing lightpath QoT computation with machine learning in partially disaggregated optical networks." IEEE Open Journal of the Communications Society 2 (2021): 564-574.

3. **Giacomo Borraccini**, Andrea D'Amico, Stefano Straullu, Antonino Nespola, Stefano Piciaccia, Alberto Tanzi, Gabriele Galimberti, Stefano Bottacchi, Scott Swail, Vittorio Curri. "Cognitive and autonomous QoT-driven optical line controller." Journal of Optical Communications and Networking 13.10 (2021): E23-E31.

4. **Giacomo Borraccini**, Stefano Straullu, Andrea D'Amico, Antonino Nespola, Stefano Piciaccia, Alberto Tanzi, Gabriele Galimberti, Vittorio Curri. "Autonomous Raman amplifiers in multi-band software-defined optical transport networks." Journal of Optical Communications and Networking 13.10 (2021): E53-E62.

5. **Giacomo Borraccini**, Stefano Straullu, Stefano Piciaccia, Alberto Tanzi, Gabriele Galimberti, Vittorio Curri. "Cognitive Raman amplifier control using

an evolutionary optimization strategy." IEEE Photonics Technology Letters 34.4 (2022): 223-226.

6. Andrea D'Amico, Bruno Correia, Elliot London, Emanuele Virgillito, **Giacomo Borraccini**, Antonio Napoli, Vittorio Curri. "Scalable and disaggregated ggn approximation applied to a C+L+S optical network." Journal of Lightwave Technology 40.11 (2022): 3499-3511.

7. **Giacomo Borraccini**, Andrea D'Amico, Stefano Straullu, Fehmida Usmani, Arsalan Ahmad, Vittorio Curri. "Iterative supervised learning approach using transceiver bit-error-rate measurements for optical line system optimization." Journal of Optical Communications and Networking 15.2 (2023): 111-118.

8. **Giacomo Borraccini**, Stefano Straullu, Alessio Giorgetti, Renato Ambrosone, Emanuele Virgillito, Andrea D'Amico, Rocco D'Ingillo, Francesco Aquilino, Antonino Nespola, Nicola Sambo, Filippo Cugini, Vittorio Curri. "Experimental Demonstration of Partially Disaggregated Optical Network Control Using the Physical Layer Digital Twin." IEEE Transactions on Network and Service Management (2023).

Contributions to International Conferences

1. Alessio Ferrari, **Giacomo Borraccini**, Vittorio Curri. "Observing the Generalized SNR Statistics Induced by Gain/Loss Uncertainties." 45th European Conference on Optical Communication (ECOC 2019). IET, 2019.

2. Emanuele Virgillito, Rasoul Sadeghi, Alessio Ferrari, **Giacomo Borraccini**, Antonio Napoli, Vittorio Curri. "Network Performance Assessment of C+L Upgrades vs. Fiber Doubling SDM Solutions." Optical Fiber Communication Conference. Optica Publishing Group, 2020.

3. **Giacomo Borraccini**, Stefano Straullu, Alessio Ferrari, Stefano Piciaccia, Gabriele Galimberti, Vittorio Curri. "Flexible and Autonomous Multi-Band Raman Amplifiers." 2020 IEEE Photonics Conference (IPC). IEEE, 2020.

4. **Giacomo Borraccini**, Alessio Ferrari, Stefano Straullu, Antonino Nespola, Andrea D'Amico, Stefano Piciaccia, Gabriele Galimberti, Alberto Tanzi, Silvia

Turolla, Vittorio Curri. "Softwarized and Autonomous Raman Amplifiers in Multi-Band Open Optical Networks." 2020 International Conference on Optical Network Design and Modeling (ONDM). IEEE, 2020.

5. **Giacomo Borraccini**, Stefano Straullu, Alessio Ferrari, Emanuele Virgillito, Stefano Bottacchi, Scott Swail, Stefano Piciaccia, Gabriele Galimberti, Gert Grammel, Vittorio Curri. "Using QoT-E for Open Line Controlling and Modulation Format Deployment: an Experimental Proof of Concept." 2020 European Conference on Optical Communications (ECOC). IEEE, 2020.

6. **Giacomo Borraccini**, Stefano Staullu, Alessio Ferrari, Stefano Piciaccia, Gabriele Galimberti, Alberto Tanzi, Vittorio Curri. "Autonomous Raman Amplifiers in Software-Defined Optical Transport Networks." GLOBECOM 2020-2020 IEEE Global Communications Conference. IEEE, 2020.

7. **Giacomo Borraccini**, Stefano Straullu, Andrea D'Amico, Emanuele Virgillito, Lalit Kumar, Stefano Piciaccia, Stefano Bottacchi, Scott Swail, Gabriele Galimberti, Vittorio Curri. "QoT-E Driven Optimized Amplifier Control in Disaggregated Optical Networks." 2021 Optical Fiber Communications Conference and Exhibition (OFC). IEEE, 2021.

8. **Giacomo Borraccini**, Stefano Straullu, Andrea D'Amico, Antonino Nespola, Stefano Piciaccia, Alberto Tanzi, Gabriele Galimberti, Vittorio Curri. "Autonomous Physical Layer Characterization in Cognitive Optical Line Systems." 2021 Optical Fiber Communications Conference and Exhibition (OFC). IEEE, 2021.

9. **Giacomo Borraccini**, Andrea D'Amico, Andrea Carena, Vittorio Curri. "Statistical Analysis of GSNR Fluctuations Due to Physical Layer Uncertainties." 25th International Conference on Optical Network Design and Modelling (ONDM 2021).

10. **Giacomo Borraccini**, Stefano Straullu, Alessio Giorgetti, Rocco D'Ingillo, Davide Scano, Andrea D'Amico, Emanuele Virgillito, Antonino Nespola, Nicola Sambo, Filippo Cugini, Vittorio Curri. "QoT-Driven Optical Control and Data Plane in Multi-Vendor Disaggregated Networks." Optical Fiber Communication Conference. Optica Publishing Group, 2022.

11. Toru Mano, Andrea D'Amico, Emanuele Virgillito, **Giacomo Borraccini**, Yue-Kai Huang, Kei Kitamura, Kazuya Anazawa, Akira Masuda, Hideki Nishizawa, Ting Wang, Koji Asahi, Vittorio Curri. "Accuracy of Nonlinear Interference Estimation on Launch Power Optimization in Short-Reach Systems with Field Trial." 2022 European Conference on Optical Communication (ECOC). IEEE, 2022.

12. Rocco D'Ingillo, **Giacomo Borraccini**, Emanuele Virgillito, Stefano Straullu, Rocco Siano, Michele Belmonte, Vittorio Curri. "Simulative Analysis of InP-based Dual Polarization IQ Mach-Zehnder Modulators." Asia Communications and Photonics Conference 2022. Optica, 2023.

13. Andrea D'Amico, **Giacomo Borraccini**, Stefano Straullu, Francesco Aquilino, Stefano Piciaccia, Alberto Tanzi, Gabriele Galimberti, Vittorio Curri. "Statistical Analysis of PDL Penalty on Coherent Transmission Technologies Based on WSS Experimental Characterization." Asia Communications and Photonics Conference 2022. Optica, 2023.

14. **Giacomo Borraccini**, Renato Ambrosone, Alessio Giorgetti, Stefano Straullu, Francesco Aquilino, Emanuele Virgillito, Andrea D'Amico, Rocco D'Ingillo, Nicola Sambo, Filippo Cugini, Vittorio Curri. "Disaggregated Optical Network Orchestration Based on the Physical Layer Digital Twin." Optical Fiber Communication Conference. Optica Publishing Group, 2023.

15. Andrea D'Amico, **Giacomo Borraccini**, Stefano Straullu, Francesco Aquilino, Stefano Piciaccia, Alberto Tanzi, Gabriele Galimberti, Vittorio Curri. "Experimental Probing and Modeling of the PDL Impact on the Optical Signal-to-Noise Ratio." Optical Fiber Communication Conference. Optica Publishing Group, 2023.

16. **Giacomo Borraccini**, Andrea D'Amico, Stefano Straullu, Francesco Aquilino, Stefano Piciaccia, Alberto Tanzi, Gabriele Galimberti, Vittorio Curri. "Local vs. Global Optimization for Optical Line System Control in Disaggregated Networks." 2023 International Conference on Optical Network Design and Modeling (ONDM). IEEE, 2023.

17. Toru Mano, Andrea D'Amico, Emanuele Virgillito, **Giacomo Borraccini**, Yue-Kai Huang, Kazuya Anazawa, Hideki Nishizawa, Ting Wang, Koji Asah,

Vittorio Curri. "Modeling Transceiver BER-OSNR Characteristic for QoT Estimation in Short-Reach Systems." 2023 International Conference on Optical Network Design and Modeling (ONDM). IEEE, 2023.

Chapter 1

Introduction

In recent decades, the world population has experienced rapid growth and is projected to reach 9.7 billion by 2050, according to the United Nations [1]. This demographic trend has been accompanied by an increasing demand for digital connectivity, as more people use the Internet for various purposes. As of 2021, more than 4.9 billion people, or 63.2% of the world population, are Internet users, according to Internet World Stats [2]. Furthermore, the COVID-19 pandemic has accelerated the adoption of digital technologies, as companies have had to adapt to remote work and digital business models to stay afloat without losing competitiveness [3].

This surge in Internet usage has led to a significant growth in Internet Protocol (IP) data traffic, which is expected to continue in the coming years. Cisco's visual Networking Index (VNI) forecasts that global IP traffic will triple from 2018 to 2023, with a Compound Annual Growth Rate (CAGR) of 26% [4]. This growth is driven by various factors, such as the proliferation of connected devices, including machine-to-machine connections, and the increasing popularity of streaming media and cloud-based services. Moreover, the use of bandwidth-intensive applications, such as virtual reality and artificial intelligence, further contributes to the growth of IP data traffic.

An optical network is a telecommunications network that uses optical fibers to transmit data encoded as light signals through a point-to-point path from a source node to a destination node. Optical networks have been widely used to cover long-haul distances because of their high capacity and low attenuation. They have evolved rapidly over the years since their introduction in the 1980s, with advances

in technology improving their capacity and efficiency [5–8]. In the early stages of optical networks, capacity was limited and multiple fibers were required to transmit data. However, the use of Wavelength Division Multiplexing (WDM) technology allowed the transmission of multiple signals over a single fiber, thereby increasing the capacity of optical networks.

In order to have a flavor of how rapid (and therefore pervasive) the development of optical fiber systems has been, it is enough to briefly retrace a limited portion of the milestones that led to modern optical infrastructures from a historical point of view. Even if its genesis is independent, the invention of the laser [9] was crucial to the beginning of the use and experimentation of optical fibers [10]. The combined use of the two elements – the laser as a light source, and the optical fiber as a means of propagation – and then their refinement have allowed the birth of a new way of communicating, which today is the basis of most interactions between humans and machines. In addition to the communication system itself, subsequently, a third element becomes fundamental in implementing what are properly the operations of a communication network: the optical switches [11].

In 1977, the first point-to-point optical links for live telephone traffic were installed in Turin, Italy [12], and Long Beach, California [13]. In 1988, the first transatlantic fiber optic cable, called TAT-8, was installed, connecting the United States and Europe with a capacity of 280 Mb/s [14]. In the 1990s, the use of fiber optic cables became more widespread and their capacity increased significantly. In 1997, the first undersea fiber optic cable connecting the United States and Asia was installed, called SEA-ME-WE 3, achieving a capacity of 40 Gbps [15]. In 2002, the first 10 Gbps Ethernet fiber optic system was standardized [16], and then the first 100 Gbps Ethernet system in 2008 [17]. In 2014, Google announced the installation of the "Faster" cable, a fiber optic cable that links Japan and the United States, with a capacity of 60 Tb/s [18, 19]. Remaining on submarine connections, which represent the most optimized but also the most expensive solutions, the current trend is to reach capacities of the order of a few Pb/s per submarine cable [20, 21].

Up to the present day, the capacity and complexity of systems have continued to grow at an exponential rate that can be described as an equivalent Moore law for optical communications [22, 23]. There are several innovations that have led to these results. Recent advancements in the development of high-speed Analog-to-Digital Converter (ADC) and Digital-to-Analog Converter (DAC) technology have enabled

the usage of coherent receiver technology, achieving a more efficient Digital Signal Processing (DSP) [24, 25]. Together with dual-polarization multilevel formats, this technology has achieved the highest bit rates in optical networks [26]. Currently, the highest bit rates have been achieved using 800 Gb/s and 1.6 Tb/s transmission rates [27–29]. The introduction of Erbium-Doped Fiber Amplifiers (EDFAs) in the 1990s also revolutionized the usage of optical networks [30, 31]. EDFA are used to amplify optical signals without converting them into electronic signals, enabling longer transmission distances without the need for costly regenerators.

Another important development in optical networks has been the transition from the use of Optical Add-Drop Multiplexers (OADMs) to Re-configurable Optical Add & Drop Multiplexers (ROADMs) [32]. OADMs were used to add and drop optical signals at specific points in the network, but their configuration was fixed or static, making it difficult to reconfigure the network to accommodate changing traffic demands. With the introduction of ROADMs, network operators can remotely reconfigure the network to add or remove signals at any point, making the network more flexible and adaptable.

To increase the capacity of optical networks, researchers are exploring the use of Space Division Multiplexing (SDM) and multiband approaches. SDM involves transmitting multiple signals over different spatial modes in a single fiber [33]. Multiband approaches involve transmitting signals over different frequency bands to increase the capacity of optical networks [34].

Despite these advances, optical networks are currently approaching the fundamental information limit proposed by Claude Shannon in 1948, stating that the maximum amount of information that can be transmitted over a channel is limited by the channel's bandwidth and the noise in the channel [35]. Furthermore, new transceivers are increasing the bit rates without improving the spectral efficiency, and further research is required to address this challenge, continuing to improve the efficiency of the optical infrastructure.

Concurrently, as the amount of data transmitted over optical networks increases, network operators have to face different challenges trying to progressively expand their network capacity to keep up with demand. The main one is represented by the capacity crunch, or the lack of sufficient network capacity to meet the growing demand for digital connectivity [36]. However, the costs associated with network expansion can be significant, leading to revenue compression [37]. Furthermore, the

cost per bit, which measures the cost of transmitting one bit of data over the network, has been declining but not fast enough to keep up with demand growth [38]. As a result, network operators need to find ways to improve the cost effectiveness of their networks, while maintaining or improving the performance of the network [39, 40]. Additionally, as failures and cyber-attacks become more frequent and sophisticated, network reliability and security have also become important concerns [41, 42].

In view of the issues described above, one potential solution is the use of open and disaggregated optical networks that offer greater flexibility and scalability in order to cope with the growing demand for digital connectivity. Unlike traditional optical networks, which are built as integrated systems using proprietary hardware and software, open and disaggregated optical networks are based on open standards and use off-the-shelf components, allowing for greater flexibility and scalability and making them an attractive option for network operators in terms of long-term cost savings.

The placement or replacement of optical fiber is a costly operation, and operators prefer to maximize the infrastructure capacity using the already deployed resources. The adoption of open and disaggregated solutions brings multivendor solutions, implying that the infrastructure operation must be vendor-agnostic and allow interoperability between Network Elements (NEs)s of different providers. Therefore, open and disaggregated optical networks must be designed with the ability to maintain high levels of performance, even under adverse conditions, such as fiber cuts, equipment failures, or power outages. This requires careful planning and design to ensure that the network architecture and components can withstand these challenges and recover quickly in case of failures.

Furthermore, open and disaggregated optical networks enable the adoption of cognitive techniques, which can maximize network performance in terms of efficiency, energy consumption, and quality of service, among other factors. These techniques leverage optimization algorithms, artificial intelligence, and machine learning to dynamically optimize network resources and traffic routing, enabling operators to proactively address potential issues and ensure optimal performance at all times. Furthermore, network automation plays a crucial role in the operation and maintenance of open and disaggregated optical networks. By automating network processes, network operators can reduce operational costs, accelerate service deployment, and improve network resilience. Network automation also facilitates the

deployment of new services and applications, enabling network operators to respond promptly to changing customer demands.

In the next sections, the fundamental concepts and technologies behind open and disaggregated optical networks will be introduced in more detail, focusing on the latest trends and developments of open optical networking, software-defined optical networking and the possible network disaggregation models, and the application of cognitive techniques on optical networks. Following the motivations that led to this thesis work, the chapter will end with the exposition of the questions this work aims to answer, the contributions, and the objectives achieved.

1.1 Towards the Opening of Optical Networks

The creation of standards that ensure different devices and technologies working together seamlessly in a vendor-agnostic context is promoted by several standardization bodies and consortia, aiming to the development of open, interoperable optical networks. In particular, the idea is to remove the compatibility gap between the control system and the NEs involved in the open infrastructure to make them visible as white-boxes by the control software module, consequently pushing in the direction of a disaggregated and modular approach. This vision is in contrast to the previous approach of aggregated infrastructure control, or black box, in which the entire network or some portions of the network containing multiple devices were managed at the level of the control system as unitary elements. In doing so, these organizations help to cut costs and spur innovation, allowing new products and services to enter the market more easily thanks to guaranteed compliance, giving the possibility to the operators to customize their solutions and equipment according to various needs.

However, each organization takes a different approach to achieving this goal. International Telecommunication Union (ITU), for example, is a United Nations agency that sets international standards for telecommunications, responsible for the G-series of recommendations that cover everything from optical fiber to network architecture [43]. On the other hand, Institute of Electrical and Electronics Engineers (IEEE) is a professional association that develops standards across a wide range of technologies, including optical networking [44]. The Internet Engineering Task Force (IETF) is a grassroots organization that develops and promotes Internet standards, including those related to optical networking [45].

Consortia like the Optical Internetworking Forum (OIF), Open Networking Foundation (ONF), and Telecom Infra Project (TIP) are typically industry-led organizations that bring together manufacturers, vendors, service providers, operators, and other stakeholders to create standards that meet their specific needs. For example, OIF focuses on developing interoperable optical networking solutions for the transport of data [46], while the ONF is more concerned with promoting the adoption of open-source networking software [47]. Then TIP is focused on improving connectivity in emerging markets by developing new technologies and business models [48].

Other consortia, such as the Open ROADM Multi-Source Agreement (MSA) and OpenConfig, are more focused on specific technologies or aspects of optical networking. The Open ROADM MSA is focused on developing open standards for ROADM but is expanding to everything related to the physical layer of optical networks [49]. Meanwhile, OpenConfig aims to develop vendor-neutral data models and protocols for network devices [50]. In fact, in a wide variety of respects, Open ROADM MSA explicitly states that it uses OpenConfig templates.

Despite these differences in focus and approach, all of these organizations play an important role in promoting the development of open, interoperable optical networks. By working together, they can help to ensure that the networks of the future are flexible, scalable, and cost-effective while still meeting the diverse needs of different stakeholders in the industry.

A considerable amount of effort is going into creating standardized data models that vendors and operators can all utilize. A first approach has been attempted with OpenFlow, which is a protocol that allows centralized management of network devices such as switches and routers [51]. It enables a network controller to determine how data packets should be forwarded based on predefined rules or policies. For a broader and more general network management, Network Configuration (NETCONF) and Yet Another Next Generation (YANG) are two related standards used to facilitate interoperability between different NEs in a multi-vendor context [52, 53]. NETCONF, maintained by the IETF, is a standardized protocol for controlling network devices and provides a programmatic interface for vendor-neutral management, reducing the need for proprietary interfaces [54]. On the other hand, YANG is a data modeling language also maintained by the IETF emerged as the preferred language for interacting with the control and management system, describing the structure and

content of network device configurations and data [55]. YANG models are then used in combination with NETCONF to provide a standardized and interoperable way to manage network devices from different vendors in a consistent and interoperable way, reducing the risk of vendor lock-in and simplifying network operations [56].

Another important aspect within the process towards open optical networks is related to pluggable transceiver devices, providing network operators with a wider range of hardware options. This trend is driving innovation, competition, and lower costs in the industry. One of the key benefits of open optical transceiver pluggables is the scalability of the system, allowing for an easy expansion or modification of the network infrastructure as required.

The first open plug-in optical transceiver standard to emerge was C Form-factor Pluggable (CFP) in 2010, a pluggable optical transceiver used for applications up to 100G Ethernet providing a significant improvement over existing transceiver modules and enabling higher data rates and a smaller form factor [57]. Following the CFP standard, CFP2, CFP4, and CFP8 were progressively introduced with a smaller form factor and lower power consumption, achieving higher bit rates up to 400G. Then Quad Small Form-factor Pluggable (QSFP) was introduced as a more compact and hot-swappable alternative to CFP, providing an improvement in terms of power consumption and port density [58]. Subsequently, other standards derived from QSFP (QSFP+, QSFP28, QSFP56) were introduced as smaller versions of the QSFP transceiver, achieving a maximum bit rate of 200G. In 2018, two new open optical transceiver pluggable standards were released that support 400G data rates: Octal Small Form-factor Pluggable (OSFP) [59] and Quad Small Form-factor Pluggable Double Density (QSFP-DD) [60]. QSFP-DD has a the same dimension of the previous standards with denser form factor, having twice as many ports. OSFP has a slightly larger dimension than QSFP-DD and a higher power consumption, but supports 400G and also 800G. Recently, Open ZR and then Open ZR+ were released as an open standard for long-distance optical links using Dense Wavelength Division Multiplexing (DWDM) technology [61]. It supports data rates up to 400G and supports various modulation formats, providing a cost-effective solution for long-distance optical links and enabling high-speed data unrepeated transmission over a range of up to 120 km.

In conclusion, in the context of open optical networking, operators can reduce their Capital Expenditures (CAPEX) by using open hardware and software, which

can be less expensive than proprietary solutions. In the same cases, they may also be able to reduce Operational Expenditures (OPEX) by simplifying network management and reducing the need for expensive technical support. This aspect is linked above all to the strategy adopted to manage the optical infrastructure. In particular, beyond the improvement in flexibility and cost efficiency, the utilization of Software-Defined (SD) network management in combination with open standards allows to effectively maintain and troubleshoot, but also customize and upgrade the system.

1.2 Software-Defined Optical Networking

For the reasons mentioned above, network operators service providers are showing interest in disaggregated optical networks, vendor-neutral control and management, and multivendor interoperability as a way to overcome vendor lock-in and save capital outlay [62, 63] as data traffic is constantly increasing in various network segments ranging from core/metro networks to 5G/6G front-hauling [64]. Disaggregation and automation can help operators overcome vendor lock-in at the control plane level when used in conjunction with transponder, transceiver, and ROADM control and management specifications. Thus, the goal is to achieve a more dynamic level of infrastructure management, which allows the system to be easily configured and updated, both from a software and hardware point of view, integrating the structure with additional devices and features.

In recent years there has been a significant push towards the use of open and disaggregated solutions in a context of Software-Defined Networking (SDN), in which the entire network is supervised by a single central controller capable of interfacing with different NEs that are part of the physical layer [65]. This evolution allows for apparatus sharing and slicing, besides offering cost-effective and efficient solutions and facilitating the implementation of resilient optical network infrastructure with the highest capacity utilization. In conjunction with the SDN approach, Network Function Virtualization (NFV) has allowed a further step forward from the point of view of interoperability and disaggregated control of the various NEs [66]. Replacing traditional network appliances with software-based virtualized network functions, the network functions following the NFV approach are implemented as software

running on virtual machines or containers hosted on commodity hardware, pushing in the direction of opening and standardizing optical networks.

Following the SDN and NFV approaches in the context of optical communication infrastructure, the network is viewed as a set of programmable resources that can be dynamically allocated and reconfigured based on changing traffic demands and network conditions [67]. The framework consists of three main actors, which are the IP/Ethernet layer, the SDN controller and the various NEs that compose the physical layer of the network [68, 69]. At the northbound interface of the SDN architecture is the IP/Ethernet layer, which represents the higher-level network protocols and applications that are responsible for generating and consuming network traffic. The northbound interface provides a standardized set of Application Programming Interfaces (APIs) and protocols that allow these higher-level applications to interact with the SDN controller, submitting requests for network services and receiving responses to those requests. In the middle is the SDN controller, which acts as the central point of control for the network, being responsible for collecting information about the state and topology of the network from the various NEs, and making decisions about how to allocate network resources based on network policies and traffic demands. At the southbound interface, the SDN controller interacts with the NEs, both at each optical node (transceivers, transponders and ROADM) and at each optical line (optical amplifiers), relying on standard interfaces and protocols, such as OpenFlow, NETCONF and REpresentational State Transfer (REST) APIs, to communicate with these NEs and to control their behavior.

Given the properties of the described architecture, the decoupling of the optical control plane from the data plane operation represents one of the most significant benefits of SDN approach since it allows greater functional flexibility and control in the management of the optical system, unlike traditional network architectures where the control and data planes are tightly coupled [70]. Following the SDN approach, the control plane and the data plane are separated, and the data plane is solely responsible for the forwarding of data packets, freeing up NEs to focus only on optical propagation. Separation of the two control planes results in simplified network management thanks to the location of the single and centralized controller, greater agility and flexibility in reconfiguring network resources in real time, and improved scalability of the entire network [71].

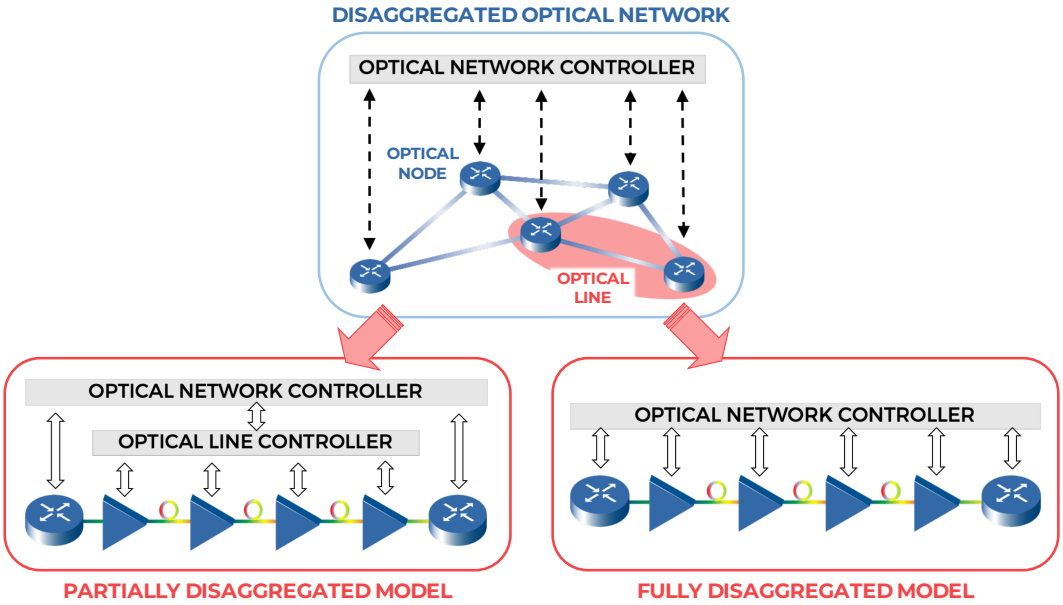

Fig. 1.1 Representation of a disaggregated optical network following two different models: the partially disaggregated network and the fully disaggregated network.

Operating an overview on the development of open SD networks, the two solutions that have stood out in recent years are Open Network Operating System (ONOS) [72] and OpenDayLight (ODL) [73]. Both ONOS and ODL are open source SDN controllers designed to provide redundancy and scalability in large-scale network environments, including fault handling. The two controllers provide large flexibility and programmability, allowing to cover many different use-cases. A substantial difference is represented by an architectural choice related to distributed implementation. In a distributed architecture, ONOS can run on multiple nodes, communicating with each other to maintain consistency and distribute updates to the network state as needed. On the contrary, ODL defines a master controller that receives input from the other controller instances and uses this information to maintain a global view of the network.

Considering the market trend towards the deployment of multiband optical transmission [74], expanding SDN controllers to include also optical amplifiers is a required feature to cope with scalability and performance challenges. From this point of view, making the optical lines interfaceable with the SDN controller in a multi-vendor context in order to obtain information from the physical layer does not appear to be a viable way yet, leading to the adoption of partially disaggregated

solutions in which each proprietary optical line is managed by a specific controller instead of a fully disaggregated system (see Fig. 1.1).

In light of the scenario described above and the challenges to be undertaken, the role and architecture of the general control structure are crucial to achieve the maximization of the optical network capacity and determining its robustness and resilience, especially at the physical layer.

1.3 Cognitive Optical Networks

Referring to the needs and interests of network operators, in addition to creating a flexible, autonomous, resilient optical infrastructure that can allow a certain degree of scalability in data traffic management, maximizing capacity appears to be another crucial point. The latter can be traced back to two main aspects, which are the optimization of the optical propagative performance of the NEs, which is related to the Quality-of-Transmission (QoT), and the Routing and Spectrum Assignment (RSA) strategy of the point-to-point connections in terms of both the physical path along the network and the choice of the channel wavelength within the propagating WDM comb. Clearly, the final result depends on the success of both functions, implemented independently in a context of SDN by the optical control plane and by the data plane.

In this regard, in the last few decades, various methodologies and techniques have been developed aiming at optimizing the transmission properties of a given network and improving efficiency in the dynamic management of connections, also considering cases of traffic restoration or recovery in the event of different types of failure. These functionalities can be classified according to three main types of optical networks, which are Elastic Optical Networks (EONs), Physical Layer Aware Optical Networks (PLAONs), and cognitive optical networks. Proceeding in order, EONs are designed to support dynamic allocation of the optical spectrum, adapting the optical channel bandwidth to the data rate requirements of the traffic or services [75, 76]. This flexibility allows optimizing spectrum utilization and increasing network capacity in contexts that can be fixed or flexible both for the data rates and the used WDM grid [77]. Then PLAONs resort to the properties of the physical layer of the transmission medium by exploiting the related modeling

to improve the performance of the network according to the chosen transmission strategy [78].

From the last decade, cognition has been introduced and theorized as an emerging feature of the next generation of optical networks [79, 80]. Cognition implies the autonomous and prompt control of a network in each abstraction layer, operating decisions and strategies based on the processing of information related to the status of the system [81]. The response to the increasing complexity of the infrastructure is given by the possibility of probing the condition of the network through monitoring devices and efficiently analyzing the information extracted using flexible software modules [82]. Cognitive optical networks incorporate cognitive computing techniques such as optimization algorithms or artificial intelligence to optimize network performance, learning from in-field network data with the aim of improving network efficiency and preventing network failures.

Beyond the different functionality and purpose of each family of optical networks, the main difference lies in the degree of automation and intelligence that they require. In fact, the first two types of networks allow the system to be adaptable and programmable without having an exchange of information between the control unit and the physical layer, which improves these properties. On the other hand, cognitive optical networks are based on advanced automation mechanisms that allow periodic collection and processing of data from the physical layer in order to then determine the configuration that allows optimizing the behavior of the infrastructure, making them effective for dynamic and unpredictable network environments.

Focusing on the operation of cognitive optical networks, telemetry and monitoring devices play a fundamental role, since they allow retrieving information from the field to address different tasks and operations [83]. Taking into account the range of the different NEs, the telemetry data collected by the physical layer come mainly from the transceivers, the ROADMs and the various amplification sites. In addition, other information can be obtained from devices external to the NEs installed to increase the knowledge of specific physical properties, such as Optical Spectrum Analyzers (OSA), Optical Channel Monitors (OCMs), Optical Time Domain Reflectometers (OTDRs), polarimeters, or dedicated sensors. Telemetry data commonly monitored in this regard are the power levels for all NEs, then specifically the accumulated chromatic dispersion and Bit Error Rate (BER) are exploited for the transceivers, and the filtering properties for ROADM.

Returning to the concept of maximizing the capacity of an optical network, a fundamental property on which the control plane and the data plane operations depend is QoT. In particular, the latter is optimized by tuning the operating point of the optical amplifiers and the launch power of the channels composing the WDM spectrum, and then the provisioning and maintenance operations of Lightpaths (LPs) are determined based on the QoT reached. A LP is a transmission channel in the optical domain, defined by the physical path between a source and a destination node, which does not include any optical-electronic-optical conversion, and the frequency slot used, which implies the wavelength continuity. As far as coherent transmission technology is concerned, the receiver DSP ability to recover the constellation phase noise by means of Carrier Phase Estimation (CPE) algorithms and the linear mapping between the optical field and the electric received signals have contributed to the model of optical transmission as Additive White and Gaussian Noise (AWGN) channels, enabling optical transmission through transparent LP using coherent technology [84–86].

When this condition is satisfied, the generalized signal-to-noise ratio, GSNR, can be used as a unique merit figure to carry out Quality-of-Transmission Estimation (QoT-E) [87, 88]. Considering the main contributions that allow its estimation, the GSNR related to the channel associated with the specific central wavelength, λ, is determined by dividing the signal power, P, being tested by the total of the accumulated Amplified Spontaneous Emission (ASE) noise, P_{ASE}, caused by optical amplifiers and the Non-Linear Interference (NLI) impairment, P_{NLI}, due to signal propagation through the optical fiber span:

$$\mathrm{GSNR}_{\lambda} = \frac{P_{\lambda}}{P_{\mathrm{ASE};\lambda} + P_{\mathrm{NLI};\lambda}} = \left(\frac{P_{\mathrm{ASE};\lambda}}{P_{\lambda}} + \frac{P_{\mathrm{NLI};\lambda}}{P_{\lambda}} \right)^{-1} = \frac{1}{\left(\mathrm{OSNR}_{\lambda}^{-1} + \mathrm{SNR}_{\mathrm{NL};\lambda}^{-1} \right)} . \tag{1.1}$$

The GSNR expression can be rephrased in terms of signal-to-noise ratios, where the non-linear signal-to-noise ratio, $\mathrm{SNR}_{\mathrm{NL}}$, includes the effect of the NLI noise power, and the optical signal-to-noise ratio, OSNR, refers to the ASE noise generated by optical amplifiers. Both the noise power ASE and NLI refer to the same bandwidth, B_n. For completeness, the latter coincides with the value of the symbol rate, R_s, since the GSNR is defined by referring to the equalized signal constellation.

Observing what may be other contributions to the performance degradation of a real network, they are multiple and attributable to each element present in a point-to-point optical connection. First, the quality of the modulated optical signal

produced by a transmitter is not ideal [89]. Moving on to the coherent receiver side, it suffers from various transmission issues in a way that significantly depends on the DSP implementation [90]. In fact, the receiver compensation mechanism allows no penalties up to a certain threshold declared by the manufacturer on the basis of each degradation contribution. This is the case of Chromatic Dispersion (CD) and Polarization Mode Dispersion (PMD) introduced by the optical fiber. Other QoT penalties are related to filtering and the Polarization-Dependent Loss (PDL), or Polarization-Dependent Gain (PDG), introduced during propagation by ROADM and EDFA. Furthermore, to ensure the correct functioning of each established LP and to avoid Out-Of-Service (OOS), it is necessary to take into account further degradation that can vary over time, such as aging of the components or fluctuations in signal power and noise, completely defining what the margins of the system [91].

In contexts dominated by the contributions derived from the propagation of the optical fiber, for example, as occurs in backbone networks, the use of a Digital Twin (DT) of the physical layer is functional for an automated and efficient management of the infrastructure, allowing QoT estimator to exploit the suitable models produced as a result of processing the information collected from the physical layer [92–94]. According to the definition, implementing a DT requires that this virtual representation or model of a physical object, system, or process is connected to its physical counterpart through sensors, devices, and other data sources, enabling bidirectional communication and synchronization [95]. For this reason, the automation of the entire infrastructure and the compatibility of the interfaces between the individual NEs and control units reserve a further added value, allowing physical models to evolve in the direction of a DT.

1.4 Goal, Work Structure & Premise

Downstream of the process that leads to the affirmation of open and disaggregated solutions in the world of optical networks, the implementation of cognitive computing techniques within the control units appears to be one of the most advanced strategies. The telemetry process, which uses data related to the physical layer, allows efficient use of resources and the maintenance of a high level of accuracy and dependability in the face of increasing complexity of the infrastructure.

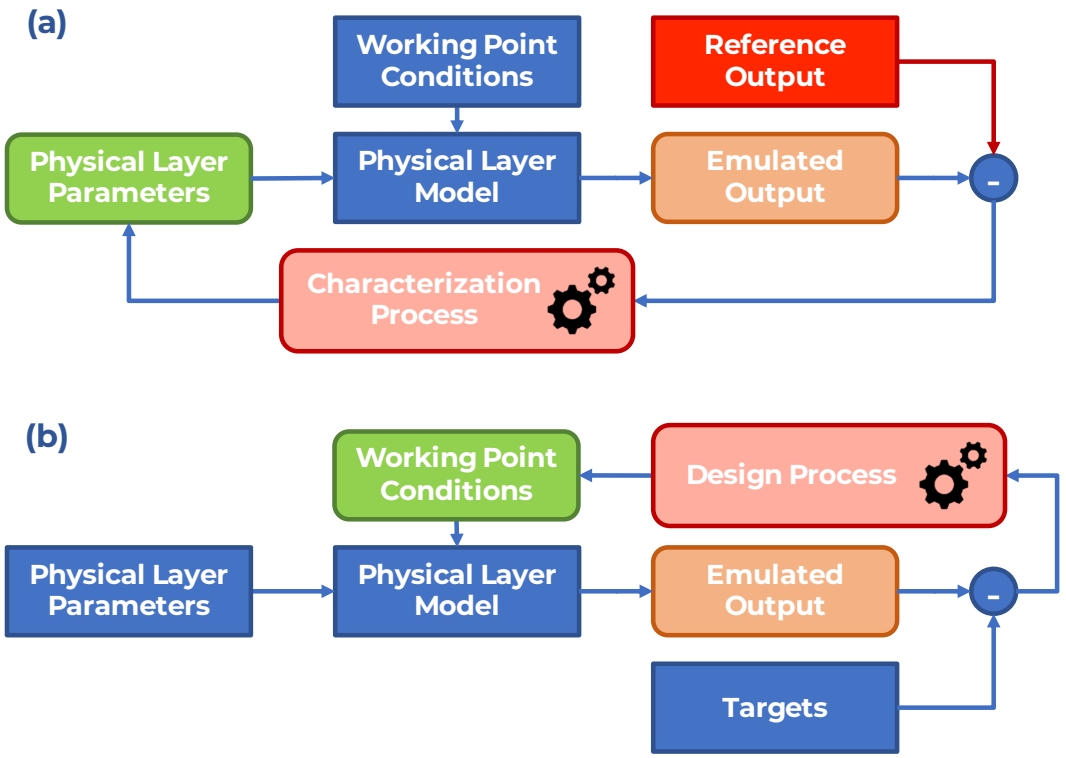

Fig. 1.2 Block diagram of the two-step cognitive methodology from a general point of view: (a) physical layer characterization, (b) design process.

For these reasons, the goal of this work is to investigate the topic of cognitive techniques within the scope of optical networks previously described, by optimizing the performance of the considered system. The developed methodologies have been put into practice across various use-cases of increasing complexity and extension, where each corresponding controller architecture was appropriately defined:

- single-span Raman amplifier system;
- multi-span EDFA-amplified optical line system;
- complete optical network (triangular and linear topology).

The general methodology adopted to maximize the capacity of the system can be summarized through a two-step optimization process, implemented during the provisioning phase of an optical network (see Fig. 1.2). The nodal point of this approach is centered around the use of a physical layer model, capable of simulating the behavior of the system under consideration. In the first step, the physical layer is

fully characterized, whereby the necessary features are obtained from the available telemetry to estimate the relevant physical layer parameters. Subsequently, from the tuned physical layer model, the working point of the system is appropriately designed. During the first step, the system is set under specific conditions, and the physical layer model is adjusted to match the optical transmission behavior as reported by the telemetry. Thereafter, on the basis of the network controller targets, the working point of the system is optimized by manipulating the softwarized representation of the optical system.

This thesis is divided into three main chapters, each one of which presents a specific use-case for which one or more cognitive techniques are designed. Each chapter has a general internal structure which can be summarized by the following items:

- *architecture*: defining what is the system under investigation in terms of elementary devices;
- *modeling*: describing the physical layer models that explain the behavior of the investigated system;
- *methodology*: reporting the developed procedures and control strategies in terms of telemetry data collected and their processing;
- *setup*: describing, in the case of experiments, the instrumental devices used, both software and hardware, how they are structured and their settings, or, in the case of simulations, the considered scenario and the physical parameters involved;
- *results*: showing the experimental or simulation results for each analyzed scenario and commenting on the salient aspects in great detail.

The whole work ends with a concluding chapter, which summarizes the thesis work carried out and outlines the possible future developments that this work suggests.

Before proceeding to the specific technical aspects of each chapter, it is necessary to make a general premise.

This work assumes that the considered optical system operates by filling the spectrum of the system under test with ASE noise-shaped and modulated channels under a full spectral load condition, and this decision is motivated by two primary

factors. The first reason is that it allows the optical network to operate in the worst-case scenario for NLI impairment, while maintaining a static GSNR metric over time and thus preventing further degradation of the channels' QoT, which allows a considerable simplification from the point of view of network control and the determination of the maximum bit rate of LPs to be assigned. The second motivation is to prevent transient effects from spreading across the network due to the gradual loading of channels, variations in the launch power, or even LPs' drop due to fiber cuts. As a result, this approach reduces the frequency with which network components must be reconfigured to operate in the optical control plane and allows a more accurate QoT-E, which is necessary to attempt a zero-margin working mode, at least in the first instance.

As already stated, this work presents both experimental and simulation results. In the first case, the main objective is to validate and test the effectiveness of the software tools and methodologies designed on commercial equipment, in order to highlight the criticalities and degrees of freedom where it is still possible to work both to intensify the cognitive process of the control system and to simplify it. In the second case, the simulation sets-ups are built so that they can be reproduced later using experimental apparatus, or to extend a realistic scenario more easily, being able to observe a wider range of scenarios.

Although it will be specified case by case, in most of the investigations performed, the adopted physical model is the one described in the open source software library called Gaussian Noise Model in Python (GNPy) [96, 88, 97], carrying out tests to establish its effectiveness and reliability.

Clearly, the application of cognitive techniques can also be extended to the case of variable spectral load, whose implementation requires a less complex apparatus and control, but presents a greater difficulty in estimating QoT. This work addresses the full spectral load case, opening a discussion of the variable one in the concluding chapter.

Chapter 2

The Counter-Propagating Distributed Raman Amplifier Case

In the last decades, in addition to the strengthening of the actual infrastructures and the creation of new solutions, the focus of research – and also of the market – has pointed towards systems that deeply exploit features of the already installed resources, taking full advantage from them. Going into detail, focusing on the field of optical fiber networks, the design of amplification sites and their management within the context of SDN turn out to be fundamental factors in the achievement of high performance systems with larger capabilities. When defining a high-performance optical amplifier, it is distinguished by its ability to impart significant gain and output power, maintain low noise, exhibit a uniform gain spectrum, accommodate wavelength versatility, and ensure stability. Furthermore, additional equipment for remote control, monitoring, and management, allows network operators to adjust amplifier parameters and verify its status. Collectively, this fusion helps to achieve superior signal fidelity, allows transmission distances to be extended, and contributes to the overall high performance of the network.

For this purpose, a consolidated amplification technology in backbone networks renowned for its feature of producing a lower equivalent noise figure with respect to standard systems based on EDFA is Raman amplification [98, 99]. Due to its characteristic of keeping the ASE noise generation low [100, 101], the use of Distributed Raman Amplifiers (DRAs) is sensibly favored in the realization of long-haul optical communication systems [102, 103]. The distributed amplification produced

on the WDM spectrum originates from the optical power provided by high-frequency high-power lasers, known as pumps, which are used to recover part of the channel loss experienced during propagation. Furthermore, given the broad-band impact, this kind of amplification allows to manage very DWDM spectra, contributing to enable multi-band transmissions [104, 105]. In terms of maximum reach and noise degradation, a notable trade-off is obtained by adopting a hybrid amplification technique based on EDFAs and DRAs, which combine high performance and relatively low noise generation [106].

Considering the field of long-haul multi-band transmissions, the increase in computational power available on board recent controller devices has allowed softwarization and disaggregation of the optical network and improved service management through the implementation of more sophisticated models and optimization algorithms [107]. At the same time, physical layer characterization has become a fundamental step in the probing procedure to adequately feed and effectively exploit such calculation tools. As a consequence, these factors have kicked off the birth of cognitive optical networks, in which the network infrastructure becomes an entity aware of the context where it is immersed and able to take decisions, to learn, and to optimize features. Referring specifically to the physical layer, in addition to the difficulty of acquiring a sufficient amount of information from the optical domain, in-field operations of a generic network are affected by various scenario modifications, such as fiber cuts, component aging, and temperature. These variables deeply notch system performance, especially in case of multi-band DWDM, where Raman cross-talk becomes a dominant nonlinear effect [74].

In order to achieve effective designs of cognitive optical networks, this infrastructure must be composed of software modules that confer dynamism and flexibility to the installed equipment, acting on the basis of a robust probing procedure and exploiting the telemetry feedback. Artificial intelligence and Machine-Learning (ML) techniques seem to offer an effective solution, even if the achievement of a suitable field dataset is not provided for free in terms of time and resources. Also in this case, scenario modifications can easily alter the conditions captured during dataset measurements, even creating significant mismatches between the physical model absorbed by the single controller and the real one.

From a historical point of view, to enable the use of Raman amplification in optical communications, the first approach was to mathematically address the op-

timization problem related to the achievement of amplification targets, ranging between extremely different methodologies [108–112]. Thanks to the multiple benefits provided, DRAs was considered right away in innovative optical network designs that massively exploit the fiber link capacity [113, 114, 107]. In parallel, various research activities have investigated network solutions that include the feature of cognition at any abstraction level of the system, pushing toward the concept of autonomous and aware optical networks [79, 115, 116]. Raman amplification has been recently addressed even through the implementation of ML techniques, reaching high levels of efficiency and precision in terms of performance [117–120] if a large dataset can be collected.

A DRA can follow two configurations, co-propagating and counter-propagating, where the term refers to the propagation direction of the Raman pump optical power with respect to that of the WDM spectrum channels. Each of the two configurations has different benefits, and the choice depends on the specific use case. In the following, the case of counter-propagating DRA will be treated as it generally allows one to reach higher gains by introducing lower relative noise. Furthermore, with regard to performance metrics, only the gain profile obtained from the power variation of the WDM spectrum channels will be considered. Noise metrics such as ASE and NLI degradation will not be mentioned.

This chapter provides different descriptions of a software controller capable of autonomously handling Raman amplification on a single fiber span in the context of SD optical networks according to the available deployed telemetry, achieving the working point requested by the optical control plane in terms of gain and tilt targets. For contextualizing the results reported in the following chapter within the state of the art for DRAs, it is necessary to mention that it is complex to make a comparison with other works proposing different methodologies. The main reasons are the heterogeneity of the experimental equipment, both with regard to the Raman card and the fiber span, the metrics of interest (i.e., target achieved, accuracy of the model with respect to the measurement), and the information available from the monitoring devices. It should be noted that this research aims to make the use of commercial equipment more efficient, regardless of the characteristics of the fiber span, in the most flexible and practical way possible. Taking into account the leading works that exploit artificial intelligence techniques [118, 121, 122], the results obtained are comparable in terms of the accuracy achieved by comparing

scenarios with similar characteristics. In the discussion, the content is taken from the following publications: [123–128].

2.1 System Architecture

The architecture conceived for an autonomous DRA is illustrated in Fig. 2.1, starting from an optical network context and zooming towards a single amplification site. The graphical representation provides a general description of the control process with the related information exchanged between the monitoring devices and the control modules. The system is made up of two main software modules: Raman Design Unit (RDU) and Raman Control Unit (RCU). Firstly, RDU defines the optimal working point in designing the power level configuration of the Raman card pumps according to the requested amplification mask without considering any channel spectral load. Then, thanks to the feedback from the monitoring device, RCU performs a tracking operation on the measured gain toward the target, linearizing the problem around the optimal working point.

Focusing on the behavioral aspect of the proposed DRA controller architecture, after the installation of an optical ROADM-to-ROADM link, each DRA placed within specific fiber spans is calibrated using a probing procedure, conceived to acquire the knowledge of the physical layer needed by the RDU for optimization. At

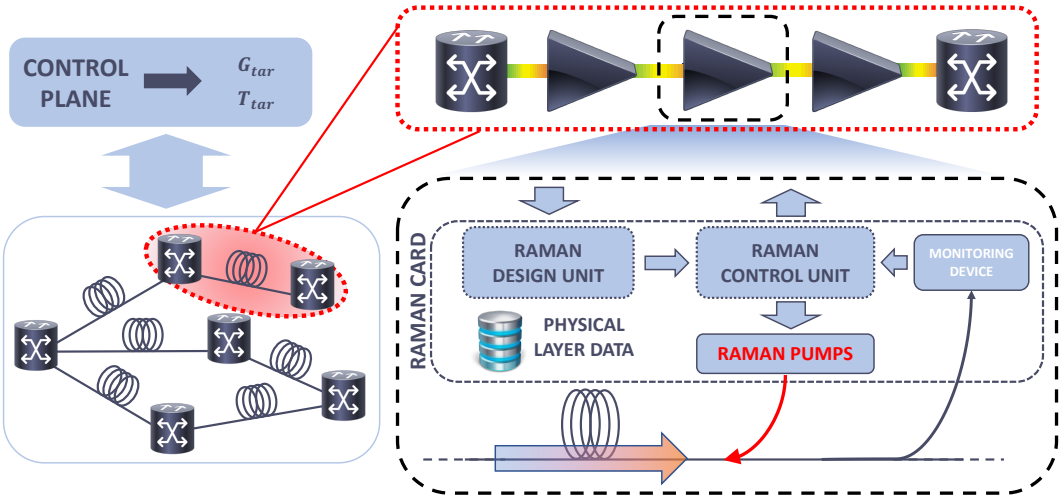

Fig. 2.1 Designed general controller architecture for an autonomous DRA working in a single fiber span contextualized within an SD optical network.

this point, DRAs are ready to be configured in terms of target parameters, and the workflow starts with the definition of the amplification targets as mean gain and tilt for each amplification site by the control plane. Locally, DRA controllers receive the description of the respective target gain mask and each RDU proceeds with the definition of the Raman pump power configuration that matches the amplification targets. This optimization phase is performed regardless of the channel spectral load, considering only inter-pump interaction. In addition to the optimal Raman pump power configuration, RDU also calculates in advance the power gradients for each pump with respect to the gain variation, which are parameters that RCU will use to adjust the mean gain profile. This step is done internally by the optimization framework before the start of real in-line operations. Subsequently, RCU is in charge of setting the Raman pump power levels according to the computed configuration. Thanks to a linearization algorithm based on the gradient evaluation performed by RDU and telemetry data provided by field monitoring devices, RCU controls the Raman pumps by varying their power levels to achieve the mean gain compensating for the depletion effect generated by the propagating comb WDM. The exploited monitoring devices are located at the end of the considered fiber span in order to monitor the status of propagating spectrum resolute in frequency after the amplification.

The proposed controller architecture implies several advantages regarding the adaptability to the physical layer features of the scenario in which the system is inserted and the flexibility with respect to spectral load variations. In particular, the anatomy of the controller combined with the currently only mentioned probing procedure allows one to easily manage cases of fiber cuts or components' aging, which are probable issues related to the scenario modifications. The conceived framework is able to support both multi-band and single-band transmission following the necessities of the network. The focus of the optimization process is to define a Raman pump power level configuration that matches the target given a set of Raman pump lasers at specific frequencies. The implementation could be extended including the design of the optimal frequencies of the Raman pumps to define the characteristics of Raman cards for specific applications, but this study is not addressed in this work.

Regarding the execution of single fiber span operations, recording the optimization time for different combinations of target values RDU requires a computational time that is in the order of some minutes. From an application point of view, this

operation is the most time-consuming part of the control process, but it has to be performed only once during the initialization of the system before the actual traffic deployment and can be done simultaneously for every amplifying site, as it is a local procedure. When the optimal Raman configuration is set, RCU performs analytical computations to adjust the mean gain toward the gain target with real-time response. Thus, RCU may exploit the edge computing available in network elements, which guarantees a quick response and consequent adaptation to possible variations in the physical layer.

In the next sections, a more detailed view of the probing procedure and of the content of the software module is provided, even reporting information and clarifications about the choice of the adopted strategies and protocols.

2.2 Stimulated Raman Scattering Modeling

Raman scattering consists of two main processes: Stimulated Raman Scattering (SRS) and spontaneous Raman scattering. SRS refers to the inelastic scattering of an optical signal traveling in silica, leading to energy transfer from higher frequency channels to lower frequency channels, along with phonon emission. Consequently, spontaneous Raman scattering occurs when a material naturally emits photons with different energies as a result of its vibrational modes being excited by incident light.

The SRS phenomenon is modeled in Single Mode Fibers (SMFs) through a system of Ordinary Differential Equations (ODEs) describing the signal power evolution of channels and pumps [129, 99]:

$$\pm\frac{dP(f_i,z)}{dz} = P(f_i,z)\,l(z)\cdot\Bigg[-\alpha(f_i)+ \sum_{j=i+1}^{N} C_R(f_i,f_j)P(f_j,z) - \sum_{j=1}^{i-1}\frac{f_j}{f_i}C_R(f_i,f_j)P(f_i,z)\Bigg], \tag{2.1}$$

where z represents the spatial coordinate along the fiber span, α is the loss coefficient, l represents the function of lumped losses spread along the fiber span, C_R is the Raman gain coefficient between the i-th and j-th frequencies, where f is the frequency array ordered from f_1 to f_N which are the lowest and the highest frequencies, respectively. The sign "$\pm$" distinguishes co-propagating channels (+) and counter-

propagating ones (-). Since in this work only the counter-propagating DRA case is treated, the boundary conditions are $P(f, z = 0)$ for channels and $P(f, z = L_S)$ for pumps, where L_S is the length of the fiber span considered.

2.2.1 Optical Fiber Physical Layer Parameters

In the following, the parameters of the physical layer involved in SRS in SMFs are presented, underlining their dependence on frequency. The latter aspect is functional to accurately model the optical propagation phenomenon in a generic wideband transmission scenario. A complete description of each physical layer parameter is provided in [130] and a summary focused on a wideband transmission scenario is given in [131].

Loss Coefficient Function

The power loss that affects the propagation of the optical signal through a fiber is taken into account by the fiber loss coefficient, α. The wavelength of the propagating signal determines the attenuation of the fiber [132], and depends on the composition of the fiber and the manufacturing process. From a phenomenological perspective,

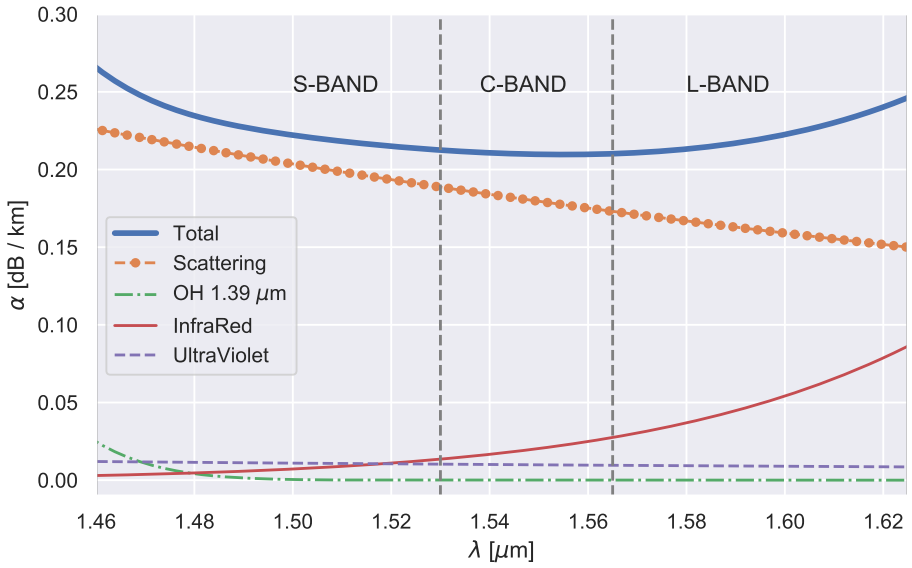

Fig. 2.2 A generic loss coefficient profile and the related model contributions.

the contributions in the wavelength range between 1.2 and 1.7 μm are the Rayleigh scattering, the violet and infrared absorption, the maximum absorption of OH ions at around 1.25 and 1.39 μm, and the absorption caused by phosphorus in the fiber core. [133] proposed a parametric model of the loss coefficient function with respect to each phenomenological component (see Fig. 2.2). The loss coefficient profile may be written as follows with regard to the optical signal wavelength and all terms written in logarithmic units (dB/km):

$$\alpha(\lambda) \simeq \alpha_{\mathrm{S}}(\lambda) + \alpha_{\mathrm{UV}}(\lambda) + \alpha_{\mathrm{IR}}(\lambda) + \alpha_{13}(\lambda) + \alpha_{12}(\lambda) + \alpha_{\mathrm{POH}}(\lambda)\,,$$

where:

$$\begin{aligned}
\alpha_{\mathrm{S}}(\lambda) &= \mathrm{A}\lambda^{-4} + \mathrm{B}\,, \\
\alpha_{\mathrm{UV}}(\lambda) &= K_{\mathrm{UV}} e^{C_{\mathrm{UV}}/\lambda}\,, \\
\alpha_{\mathrm{IR}}(\lambda) &= K_{\mathrm{IR}} e^{-C_{\mathrm{IR}}/\lambda}\,, \\
\alpha_{13}(\lambda) &= \mathrm{A}_1 \left(\frac{A_{\mathrm{a}}}{\mathrm{A}_1} e^{\frac{-(\lambda-\lambda_{\mathrm{a}})^2}{2\sigma_{\mathrm{a}}^2}} + \frac{1}{\mathrm{A}_1} \sum_{i=1}^{3} A_i \, e^{\frac{-(\lambda-\lambda_i)^2}{2\sigma_i^2}} \right), \\
\alpha_{12}(\lambda) &= \mathrm{A}_1 \left(\frac{1}{\mathrm{A}_1} \sum_{i=4}^{5} A_i \, e^{\frac{-(\lambda-\lambda_i)^2}{2\sigma_i^2}} \right), \\
\alpha_{\mathrm{POH}}(\lambda) &= A_{\mathrm{POH}} e^{\frac{-(\lambda-\lambda_{\mathrm{POH}})^2}{2\sigma_{\mathrm{POH}}^2}}\,,
\end{aligned}$$

in turn, stand for the contributions from the Rayleigh scattering, ultraviolet, infrared, OH− peak absorption, and (P)OH. By taking into account the important elements in the C, L, and S bands, the overall model may be made simpler while ignoring the contributions from the OH-ion absorption peak at 1.25 μm and phosphorus. Additionally, within the interest band, the UV absorption exhibits consistent broad-band behavior. With these presumptions, it is possible to define 5 parameters: A, B, K_{IR}, A_1 and K_{UV}, which take into account the effects of each phenomenological contribution.

Effective Area

The effective area , A_{eff}, may be calculated as the circle area having as radius the optical mode radius, w, which depends on the central pulse wavelength and the fiber

geometry, when the mode profile of the pulse is well approximated by a Gaussian function. In more detail, the radius of the mode is denoted by $w = a/\sqrt{\ln V}$, where a represents the radius of the fiber core and V is the normalized frequency. In the event of a minor relative index step at the core-cladding interface, $\Delta \approx (n_1 - n_c)/n_1$, this may be stated as:

$$V(\lambda) = \frac{2\pi}{\lambda} a n_1 \sqrt{2\Delta}\,, \tag{2.2}$$

where n_1 is the refractive index of the core and n_c is the refractive index of the cladding. The manufacturing fiber values of Standard Single-Mode Fiber (SSMF) parameters are $a = 4.2\ \mu$m. Then, the refractive index of the cladding, n_c, and the relative refractive index difference with respect to the core, Δ, are 1.45 and 0.3%, respectively.

Raman Gain Coefficient

The SRS is the prominent broadband non-linear phenomenon that occurs during the propagation of a WDM channel comb [99], where the propagating electromagnetic field and the fiber's dielectric medium interact to give rise to the SRS phenomenon. If the interaction is exclusively caused by the various channels within the propagating spectrum, the SRS caused by the transmission of a WDM comb is commonly referred to as Raman crosstalk in optical fiber communications. The Raman gain coefficient, C_R, which quantifies the coupling between a specific pair of channels with a frequency shift, Δf, expressed as $f_p - f_s$, where p and s are the channel indices at higher (pump) and lower (Stokes wave) frequencies, respectively. This parameter describes the regulation of power transfer between channels during fiber propagation. The kind and concentration of dopants in the fiber core, the reciprocal polarization state, the mode overlap between the pump and the Stokes wave, the absolute frequency of the pump, and other characteristics of the fiber and propagating channel modes affect this coefficient. Using a reference pump at frequency f_{ref}, it is feasible to determine the Raman gain coefficient profile for a specific fiber type [134]. In terms of optical power, the following curve may be described:

$$C_R(\Delta f, f_{ref}) = \frac{\gamma_R(\Delta f, f_{ref})}{A_{eff}^{ov}(\Delta f, f_{ref})}\,, \tag{2.3}$$

where γ_R is the Raman gain coefficient in terms of mode intensity (expressed in m/W) and A_{eff}^{ov} is the effective area considering the effective area overlap between the pump and the Stokes wave. The effective area can be calculated by averaging the effective areas at the pump and Stokes wave frequencies considered and assuming a Gaussian mode intensity distribution [135].

The whole Raman gain coefficient may be modeled using the following equation in order to completely mimic optical fiber propagation and take SRS effects into account:

$$C_R(\Delta f, f_p) = k_{pol}^{ps} C_R(\Delta f, f_{ref}) \frac{f_p}{f_{ref}} \frac{A_{eff}^{ov}(\Delta f, f_{ref})}{A_{eff}^{ov}(\Delta f, f_p)} , \tag{2.4}$$

where the ratios between the frequencies and effective areas take into consideration the scaling of the pump and the effective area, whereas k_{pol} accounts for the reciprocal polarization vector alignment between the pump and the Stokes wave [99]. It is a symmetric matrix with null main diagonal where each element can be between 0 and 2, where the value 2 means that the couple of channels has aligned polarization vectors, 1 if they are completely depolarized, and a low value close to 0 if the two polarization vectors are orthogonal. In the following, for a matter of simplicity, the notation of the Raman gain coefficient can also be:

$$C_R(\Delta f, f_{ref}) = C_R(f_s, f_p) \tag{2.5}$$

where f_s and f_p are the absolute frequencies of the channels representing the Stoke wave and the pump.

2.3 Methodology

This section generally describes the methodology followed by the controller designed to make DRA work effectively from the installation of the system. It is divided into three basic steps:

- *Probing & Characterization*: physical layer data are collected by configuring the system in a known state and exploiting the available telemetry; subsequently, these data are functional to characterize the system in order to improve the accuracy and precision of the physical model;

- *Configuration Design*: given the target parameters from the control plane, an optimization framework allows to design the power configuration of the Raman pumps based on the physical model and the parameters extracted from the physical layer;
- *Control & Compensation*: starting from the optimal working point determined in the previous phase, an iterative compensation procedure that takes advantage of telemetry devices allows the amplifier to reach the target working point.

While the second and third points are common to all the use cases analyzed, the first aspect varies according to the telemetry available and the transmission scenario considered. It will be described in more detail each time in the discussion.

2.3.1 Probing & Characterization

All pumps contained within a Raman card require a preliminary calibration step in which each of them has to be tuned to inject through the fiber the desired amount of optical power, benefiting from probing the physical layer in the management of the DRA. In fact, DRA turns out to be an extremely sensitive system to the environment in which it will operate. Its sensitivity is related to the fact that the high-power light emitted by each pump interacts intensely with the others due to SRS, generating different "Raman scattering orders". The latter refer to the different energy or frequency shifts that photons experience as a result of their interaction within the fiber. Since the gain profile generated by the DRA in the WDM spectrum is a joint effect of the entire set of pumps, the variation in power of each single pump can result in a different, even significant, variation in the signal spectrum due to the physical characteristics of the fiber and frequency of each pump. For this reason, it is essential to refine the parameters with which to feed the used physical model by probing the response of the real physical system, adequately characterizing optical devices with non-flat frequency response.

The whole controller framework is based on the knowledge of the following physical parameters:

- the fiber span length, L_S ;
- the lumped losses along the fiber span, l ;

- the Raman gain coefficient of the fiber, C_R ;
- the loss coefficient function, α .

2.3.2 Configuration Design

The RDU represents an optimizer capable of determining the power configuration in order to match the amplification targets, given a set of defined Raman pumps and a physical description of the fiber-span link. The core of RDU is a numerical solver which allows one to emulate the SRS phenomenon for different pump power levels through a system of ODEs that describes the power evolution [99].

The optimization problem can be formulated as follows:

$$\min_{x} \mathrm{F}(x) \tag{2.6}$$

where F represents the objective function (which will be introduced immediately below) and x are the variables to optimize, i.e. the power levels of the Raman pumps. For each of them, the power level ranges from zero to the maximum amount that can be delivered. In addition, the maximum total power injected by the Raman card into the fiber span is considered as an input constraint of the problem.

In the optimization procedure, only the depletion mechanism among Raman pumps is considered, while pump-channel and inter-channel interactions are neglected, with the aim of having an initial regulation of the working point of the amplifier which is independent of the spectral load propagating inside the fiber section. The depletion effects due to the WDM comb are compensated in the next phase, refining the configuration built during this design phase. The on-off gain profile, G_{OO}, obtained by a single pump-channel pair is computed as:

$$G_{OO}(f_{ch}) = \exp\left(\int_0^{L_S} C_R(f_{ch}, f_p) P(f_p, \zeta)\, d\zeta\right) \tag{2.7}$$

where f_{ch} is the specific channel frequency. The contribution of each pump is considered analytically identical, and therefore, the overall effect on a single channel is equal to the product of each contribution of the Raman pump.

Considered a combination of Raman pump power values, after the evaluation of the on-off gain profile by means of the physical layer model, the mean, $\overline{G_{OO}}$, the

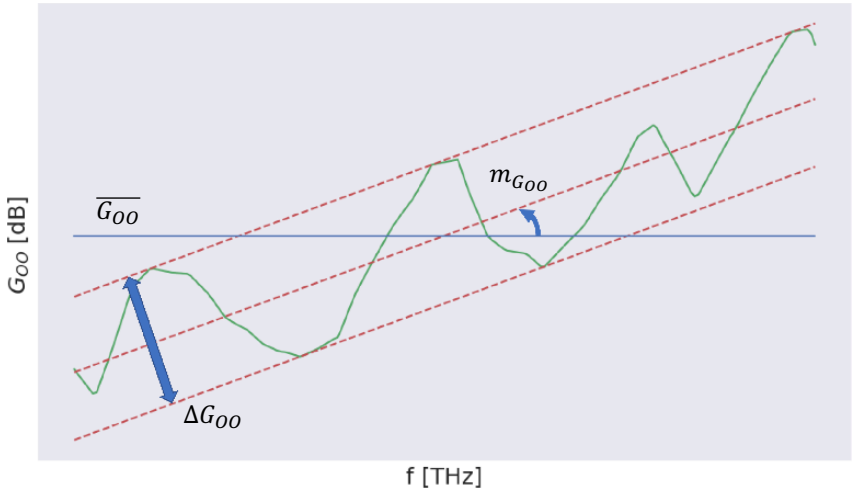

Fig. 2.3 Metrics of interest derived from the on-off gain profile.

angular coefficient of the linear regression, $m_{G_{OO}}$, and the maximum deviation from the linear regression, ΔG_{OO}, are derived (see Fig. 2.3). Thereby, the general form of the objective function considered is:

$$\mathrm{F}(x) = \frac{|\,\overline{G_{OO}} - \mathrm{G_{tar}}\,|}{\mathrm{G_{tar}}} + |\,m_{G_{OO}} - \mathrm{T_{tar}}\,| + \Delta G_{OO} \tag{2.8}$$

where $\mathrm{G_{tar}}$ and $\mathrm{T_{tar}}$ represent the gain and tilt targets required by the DRA. The cost function is designed to evaluate the combination of power levels of the Raman pumps that produces a gain mask centered on the required target values, annulling the first two terms, with the smallest gain ripple, minimizing the dispersion of the profile with respect to its linear regression.

Since the optimization procedure is performed regardless of the spectral load of the channels traversing the fiber span, the optimal Raman pump configuration found by RDU presents deviations from the expected result after which RCU sets the Raman card. In particular, considering the metrics of interest, the on-off gain profile produced in the field can have two possible mismatches: the mean and tilt values. What is experimentally shown also in this work is that the unique significant and appreciable drawback is related to a limited variation of the average gain on-off, while the slope of the linear regression is not affected in fairly long fiber-length conditions. In fact, the presence of the WDM spectrum leads to a pump depletion effect, which is not taken into account during the configuration design but contributes to rigidly shifting the gain mask. This issue is compensated online during the

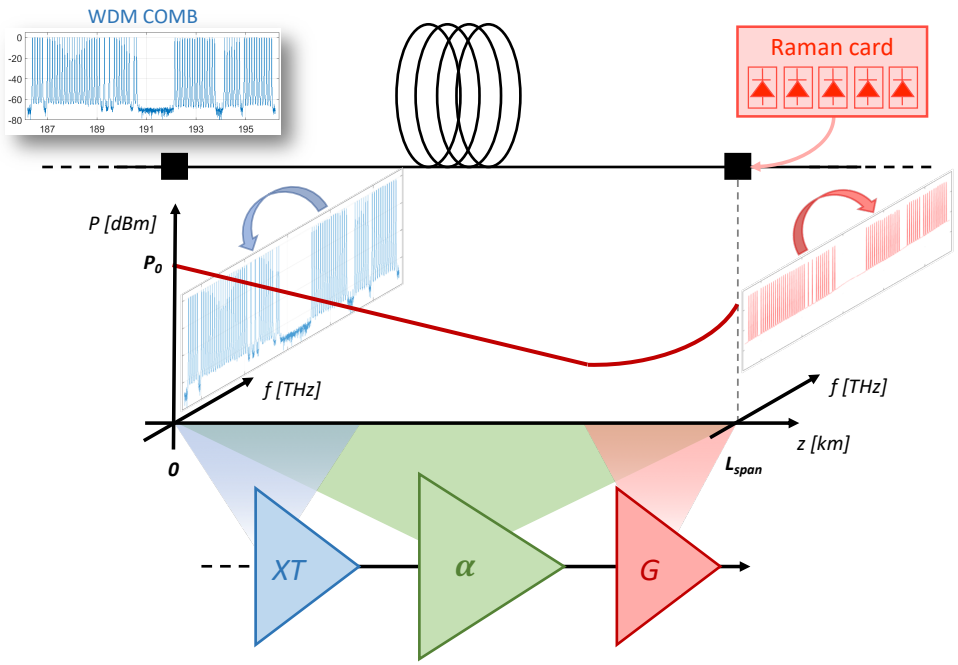

Fig. 2.4 Phenomena involved during the optical propagation along a single fiber span in presence of a DRA: fiber attenuation (α), Raman cross-talk (XT), Raman amplification (G).

operation through a conceived linearization algorithm carried out by the RCU, which restores the desired average gain without distorting the shape of the gain profile.

The observation that the input spectral load represents a minor impairment for the shape of the on-off gain profile is explicable focusing on the dynamics of the phenomena that take place along the fiber span during the propagation (see Fig. 2.4). The WDM spectrum experiences three main effects during its propagation, which are the fiber attenuation, the Raman crosstalk, and the Raman amplification. Although the attenuation effect is constant along the entire link, the impact of Raman cross-talk and Raman amplification can be circumscribed in specific areas of the link, which are the effective lengths of the corresponding phenomenon. In particular, the WDM spectrum tilting takes place only when the power levels of the channels or pumps are effective: Raman crosstalk originates in the first kilometers of the fiber span due to the high power density of the WDM spectrum, and Raman amplification occurs close to the span termination due to the high Raman pump powers. So, from an optimization point of view, it is possible to achieve the tilt requested by the control plane in the case of long fiber spans in which the two Raman tilting effects can be separated.

At the end of the optimization process, before leaving the floor to RCU, RDU computes some parameters that are fundamental to understand how to manage Raman pump power levels to proceed with the linearization algorithm. For this purpose, a couple of perturbations around the optimum solution, one positive and one negative, is applied at each Raman pump in order to observe the variations of the mean gain with respect to the selected Raman pump power level. Starting from the optimal Raman pump power levels, P_{opt}, the behavior of each perturbed configuration is emulated and the corresponding on-off gain averaging is numerically evaluated. The perturbation applied to the selected Raman pump is a small percentage of its power level, $p\%$. Considering each variation of the optimum scenario, the gradient with respect to a single input variable is computed as an incremental ratio.

$$\partial_{P^{\pm}_{opt,i}} \overline{G_{OO}} = \frac{\delta \overline{G_{OO}}}{\delta P^{\pm}(f_i, L_S)} = \frac{\overline{G_{OO,opt}} - \overline{G_{OO,opt\pm var}}}{10 \log_{10}(1 \pm p\%)} \quad \left[\frac{\text{dB}}{\text{dB}}\right] \tag{2.9}$$

where $\overline{G_{OO,opt}}$ is the on-off gain average generated by the optimal Raman pump power configuration and $\overline{G_{OO,opt\pm var}}$ is the on-off gain average derived from the configuration with the selected Raman pump power perturbed of a percentage $\pm\, p\%$. The final result is a set of parameters – formed by two gradients for each Raman pump – used by RCU to adjust the mean gain, moving the pump power levels according to the information given by the gradients.

As will then be shown during each use case, the decision of the target gain required by the control plan always follows the evaluation of the maximum gain achievable by the system as the last step during the probing process. In summary, this is done in two ways: by assuming the maximum flat gain that may be required of the system and by designing the pump configuration to obtain it, and by setting all the pumps to the maximum power that can be delivered. In this way, the control plan request is formulated considering an achievable target for the amplifier.

2.3.3 Control & Compensation

At this point, RDU provides to RCU the optimal Raman pump power configuration P_{opt} and the list of calculated gradients, $\partial_{P^{\pm}_{opt}} \overline{G_{OO}}$. Thanks to the telemetry feedback, RCU performs a tracking operation of the on-off gain average towards the target and linearizes the problem space around the optimal working point. This procedure is

Algorithm 1 Control algorithm

procedure RCU($P_{opt}, \partial_{P^{\pm}_{opt}} \overline{G_{OO}}$)
  $P = P_{opt}$
  Set Raman card pumps at P
  Extract $\overline{G_{OO}}$ from telemetry data
  while $|\overline{G_{OO}} - \mathrm{G_{tar}}| \geq \varepsilon$ **do**
    $P =$LINEARIZATION($P, \partial_{P^{\pm}_{opt}} \overline{G_{OO}}, \Delta\overline{G_{OO}}$)
    Set Raman card pumps at P
    Extract $\overline{G_{OO}}$ from telemetry data
  end while
end procedure

performed until the gap between the actual on-off gain average and the target one is below a fixed tolerance, ε (see Alg. 1).

Algorithm 2 Linearization function

function LINEARIZATION($P, \partial_{P^{\pm}_{opt}} \overline{G_{OO}}, \Delta\overline{G_{OO}}$)
  if $\overline{G_{OO}} - \mathrm{G_{tar}} < 0$ **then**
    $S_P^{\overline{G_{OO}}} = \partial_{P^{+}_{opt}} \overline{G_{OO}}$
  else
    $S_P^{\overline{G_{OO}}} = \partial_{P^{-}_{opt}} \overline{G_{OO}}$
  end if
  $S_{tot} = \sum S_P^{\overline{G_{OO}}}$
  $\Delta P = |\overline{G_{OO}} - \mathrm{G_{tar}}| / S_{tot}$
  $P_{lin} = P + \Delta P$
return P_{lin}
end function

At each iteration, the linearization procedure is applied to the problem space starting from the current Raman pump configuration (see Alg. 2). The key idea is to proportionally divide the average gain on-off gap with respect to the target according to the gradient entity of each Raman pump around the optimal working point, $\partial_{P^{\pm}_{opt}} \overline{G_{OO}}$. $S_P^{\overline{G_{OO}}}$ represents the list of sensitivities used to linearize the problem space around the current working point, which is selected between $\partial_{P^{+}_{opt}} \overline{G_{OO}}$ and $\partial_{P^{-}_{opt}} \overline{G_{OO}}$, according to the sign of the evaluated on-off gain average gap. All the values within $S_P^{\overline{G_{OO}}}$ have the same sign by construction. This process has been designed to rapidly operate adjustments of the mean gain without distorting the

on-off gain profile shape. Being a linearization procedure, it is effective around the computed optimum for small gain ranges, up to 1 dB, preserving the shape of the on-off gain profile. During the experimental campaigns conducted, deviations above this threshold have not been recorded.

2.4 C-Band DRA using Integrated Photodiodes

The first investigated use-case in which the conceived controller autonomously operates is a single fiber span having available only integrated EDFA photodiodes measuring the total optical power in the C-band frequency range. In particular, the DRA operation is optimized to achieve the required performance in terms of gain and tilt targets on the basis of the information from the physical layer extracted by means of a specific probing and characterization procedure using the mentioned telemetry. The proposal has been established in the laboratory and validated through an experimental session, testing first the probing procedure on a single fiber span and then the operation of DRA using the extracted information.

In order to maintain the reproducibility of the designed configurations by providing a specific set of physical layer parameters, a deterministic minimization method called Sequential Least Squares Programming (SLSQP) is used [136]. The choice of the optimization algorithm is due to the nature of the problem, as it belongs to the class of constrained nonlinear multi-variable optimization problems.

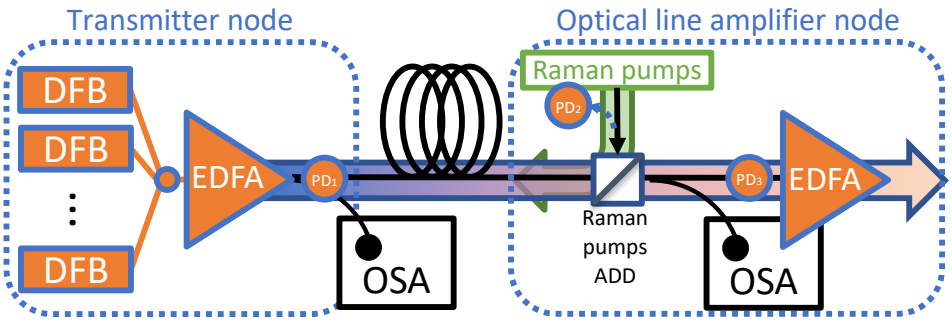

Fig. 2.5 C-band DRA using integrated photodiodes: experimental setup sketch.

2.4.1 Experimental Setup

The general scheme of the equipment used to perform the proposed measurements is shown in Fig. 2.5. It is composed of a SSMF span with 85 km nominal length (created joining 2 spools of 60 km and 25 km nominal lengths) and 2 optical nodes, called by reference the transmitter node and the optical line amplifier node. The former is composed of a system of 35 polarized, Continuous Wave (CW) Distributed Feed-Back (DFB) lasers, 100 GHz spaced, used to generate the C-band WDM spectrum. Since SRS is not sensitive to signal modulation, but only to the average power level, there is no loss of generality when using the described CW comb. The power level of each DFB laser is tuned to obtain an almost flat spectrum around 0 dBm per channel, after EDFA amplification at the transmitter node. The other span termination presents a set of 4 counter-propagating Raman pumps with frequencies roughly at 204, 206, 209 and 211 THz followed by an EDFA stage for WDM comb propagation towards the hypothetical next fiber span. An OSA is used at both fiber span terminals to verify the operation of DRA.

2.4.2 Probing & Characterization Procedure

The following procedure supports C-band transmission operations aiming to extract the loss coefficient function for pump and channel frequencies, α, the Raman gain coefficient, C_R, and a gain correction parameter, $\overline{G_{OO,cor}}$, which is a further DRA tuning parameter.

As a premise, the Raman gain coefficient is expressed as:

$$C_R(\Delta f) = K_R \, c_R(\Delta f)\,, \tag{2.10}$$

where c_R is the normalized Raman gain coefficient profile dependent on the frequency shift, Δf, between the specific couple of frequencies, and K_R is the scaling factor of the profile representing the coupling intensity. Taking advantage of the fact that different fiber varieties present significant similarities [99], only the Raman gain coefficient scaling factor is extracted, assuming the normalized profile as known [137].

In the following, the sequence of steps aimed at characterizing the physical layer will be illustrated in terms of measurements and the corresponding processing of the collected data.

Firstly, without the presence of any spectral load injected from the transmitter node, each Raman pump is switched on individually and the loss coefficient is derived by exploiting the integrated back-reflection photodiode (PD_2) through [138]:

$$\alpha(f_p) \approx \frac{\kappa P(f_p, L_S)}{2 P_R(f_p, L_S)} \tag{2.11}$$

where κ is the Rayleigh back-scattering coefficient, fixed at 0.5×10^{-7} m^{-1}, L_S is fiber span length, P is the launch power level at the Raman pump frequency, f_P, and P_R is the corresponding measured reflected power. The back-reflection photodiode, PD_2, is present within the Raman amplification system for safety reasons in order to detect fiber cut events and to avoid power wasting. Even if the proposed approach requires the assumption of the value of the Rayleigh back-scattering coefficient, κ, it allows one to estimate the loss coefficient at the Raman pump frequencies without the need of additional photodiodes at the transmission node measuring the Raman pump residual power.

As a second step, the input spectrum is introduced by loading the ASE noise at a low power level from the EDFA favoring the undepleted pump condition, and the corresponding on-off gain average, $\overline{G_{OO}}$, is evaluated in the C-band frequency range switching on one pump at a time and measuring the total power received (PD_3). Knowing that the peak of the Raman gain coefficient curve is roughly at $\Delta f^{\text{peak}} \approx 13.2$ THz, the frequency around the C-band range that maximizes the coupling for the selected Raman pump is:

$$f_{CH} = f_p - \Delta f^{\text{peak}}. \tag{2.12}$$

Being the system in undepleted pump condition, one value of Raman coupling is sampled for each measured on-off gain [134] and the related Raman scaling factor is computed as follows:

$$K_R(f_p) = \frac{\ln\left(\overline{G_{OO}(f_{CH})}\right)}{\mathscr{C}_R(f_p, f_{ch}^+, f_{ch}^-) P(f_p, L_S) L_{eff}(f_p)}, \tag{2.13}$$

where the effective length , L_{eff}, and $\mathscr{C}_R$ are defined as:

$$L_{eff}(f_p) = \frac{1 - e^{-\alpha(f_p)L_S}}{\alpha(f_p)}\,, \tag{2.14}$$

$$\mathscr{C}_R(f_p, f_{ch}^+, f_{ch}^-) = \frac{\int_{f_p - f_{ch}^+}^{f_p - f_{ch}^-} c_R(\phi)\, d\phi}{f_{ch}^+ - f_{ch}^-}\,, \tag{2.15}$$

given f_{ch}^+, f_{ch}^- the maximum and the minimum boundary frequency of the input spectrum, respectively. The final Raman gain coefficient scaling factor is obtained as the average of the collected K_R values.

Subsequently, the average fiber attenuation at the C-band frequencies is estimated as the difference of the total powers measured by the photodiodes PD_1 and PD_3 with all Raman pumps switched off. To extract the loss coefficient values at the channel frequencies, the expected on-off gain average values for each pump are computed assuming the scaled profile found in the previous step in order to probe the contribution of the fiber attenuation. Consequently, the differences between the computed values and the measured ones, $\varepsilon_{G_{OO}}$, are done and mapped on the loss coefficient function as:

$$\alpha(f_{CH}) = \overline{\alpha}\left(1 - \frac{\varepsilon_{G_{OO}}(f_{CH})}{\overline{G_{OO}(f_{CH})}}\right)\,, \tag{2.16}$$

where $\overline{\alpha}$ is the average loss coefficient estimated from the measured fiber span total attenuation. A quadratic regression is performed to refine the loss coefficient function.

Finally, in the same undepletion condition using the injected ASE spectrum, a first DRA design configuration is performed at the maximum gain target achievable by the system. After this optimization, the actual on-off gain average is measured and compared with the target value, computing the on-off gain average correction parameter as:

$$\overline{G_{OO,cor}} = \mathrm{G_{tar,MAX}} - \overline{G_{OO}}. \tag{2.17}$$

This final step aims to compensate for uncertainties due to lack of knowledge of the physical layer, improving the definition of RDU operation, and allowing a feasible procedure with a high degree of linearization for RCU. During the operative phase

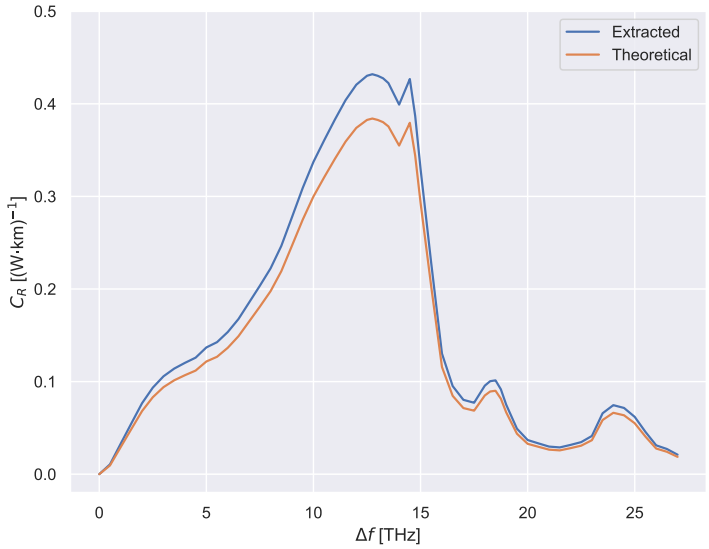

Fig. 2.6 C-band DRA using integrated photodiodes: probing and characterization result for the Raman gain coefficient profile.

Table 2.1 C-band DRA using integrated photodiodes: Raman pump power configuration (sorted by decreasing frequency).

G_{tar} [dB]	#1 [mW]	#2 [mW]	#3 [mW]	#4 [mW]
13.0	261.6	124.8	244.2	93.6

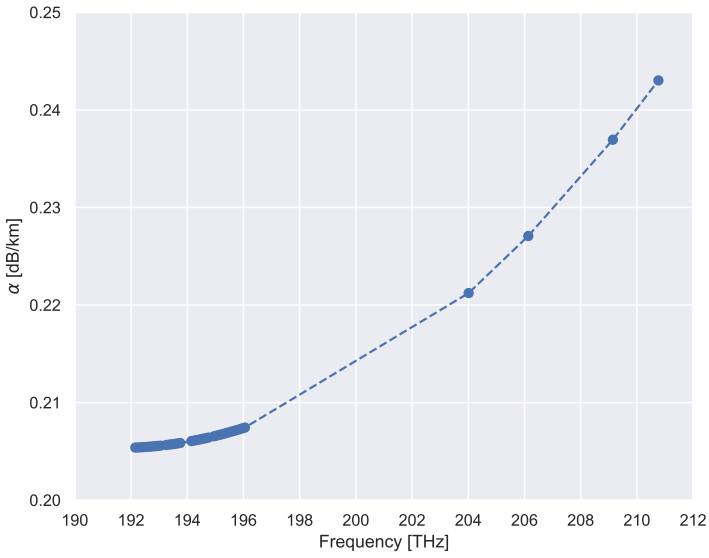

Fig. 2.7 C-band DRA using integrated photodiodes: probing and characterization result for the loss coefficient function.

of the system, all variations in the working point due to modifications of the input spectral load are managed by RCU.

As a last note, not envisaging the use of OTDRs, this procedure assumes *a priori* estimate of the connector losses at the ends of the fiber section, l. Even if the impact introduced by the output connector close to the Raman card is particularly significant for the performance of the amplification system, the last phase of the procedure guarantees the achievement of the maximum target gain required by the control system, or to find operating anomalies with respect to the planning of the installed resource. It is assumed that all reciprocal polarization states between each couple of Raman pumps are equal to 1 (completely depolarized).

2.4.3 Results

Applying the described procedure on the experimental setup, the extracted Raman gain coefficient scaling factor is similar to the theoretical one associated with a SSMF (see Fig. 2.6), and the estimated loss coefficient function is reasonable with respect to literature [133], deducing an average span loss of roughly 18 dB ((see Fig. 2.7)).

Based on the parameters of the physical layer extracted during the probing and characterization procedure, the embedded controller architecture has been tested by imparting as amplification targets a gain of 13 dB, due to the maximum Raman pump power limits, and a flat WDM spectrum at the optical line amplifier node. This goal turns out to be challenging for the apparatus under analysis, due to the required performance and the impossibility to detect any information about the system frequency behavior in standard operations. The measurements of the transmitted and received power spectra are reported in Fig. 2.8. The final configuration of the Raman pump power level deployed by the controller is reported in Tab. 2.1, with Raman pumps sorted by decreasing frequency. The received power spectrum and the on-off gain profile are shown in Fig. 2.9. Taking into account the linear regression of the WDM spectrum, the residual tilt captured by OSA is less than 1 dB over the total C band and the mean gain target has been achieved accurately.

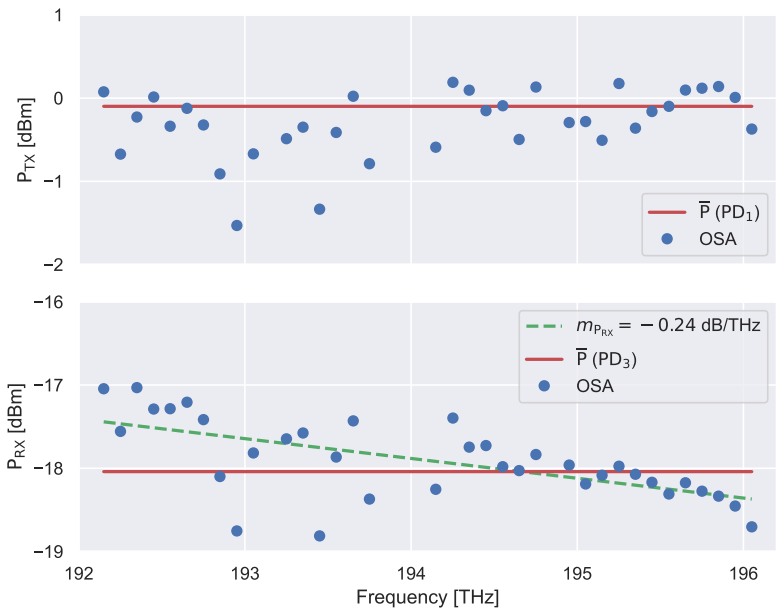

Fig. 2.8 C-band DRA using integrated photodiodes: transmitted and received spectrum power peaks, measured by OSA and photodiodes (Raman pumps turned off).

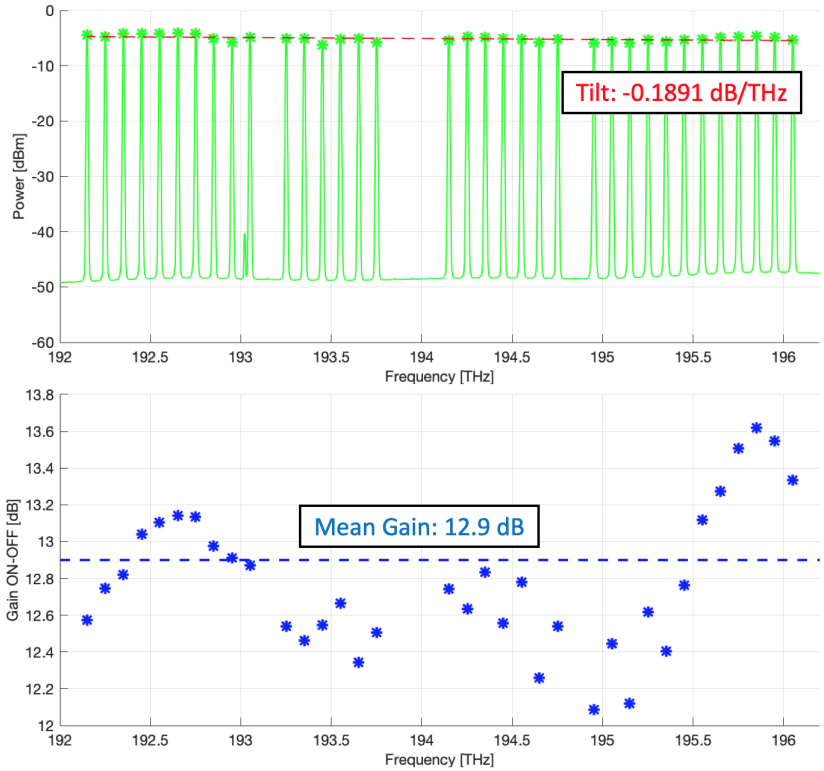

Fig. 2.9 C-band DRA using integrated photodiodes: received power spectrum and on-off gain profile.

2.5 C-Band DRA using Optical Channel Monitors

The second use case investigates the capability of a conceived cognitive DRA controller using an evolutionary optimization strategy for both the calibration of the field device and the design of the optimal pump power configuration. The developed framework is expected to work using OCMs as a telemetry device and has been experimentally validated, obtaining outstanding results in terms of precision in a C-band set-up. The proposed methodology jointly characterizes the physical layer properties of the optical fiber span, such as the fiber attenuation profile, the entities of lumped losses due to mechanical connectors or splices, the polarization coefficients between each Raman pump pair, and the Raman gain-coefficient curve. The characterization process aims to retrieve an equivalent model of the single fiber span modifying the values of the physical layer parameters by exploiting the comparison between the emulated output and the in-field probing measurements obtained in the same working-point condition. Then, the Raman pump configuration design consists in emulating the behavior of the system under different working point conditions changing the power levels of each pump and in evaluating the relevant features of the emulated gain profile with respect to the targets. The conceived approach represents an alternative effective solution to massive data-driven techniques [122] in automatizing DRAs and adapting the system after modifications of the scenario, such as fiber cut events.

For both characterization and configuration design, given the non-linear nature of the physical layer model and the increased complexity of the problems, in this use case, the adopted optimization algorithm is Co-variance Matrix Adaptation Evolutionary Strategy (CMA-ES) [139]. The choice is related to the target precision of the required solution, wanting to optimize a larger set of variables having more information available from the physical layer. By the way, it is worth noting that, even if the choice of the optimization algorithm impacts the effectiveness and execution time of the procedure, it does not compromise the validity of the developed methodology.

2.5.1 Experimental Setup

The control framework is based on the assumption of fiber span equipment reported in Fig. 2.10. It is made up of three elements, which are an In-Line Amplifier (ILA),

a series of fiber spools, and a Raman card. Each ILA consists of an EDFA equipped with OCMs at both terminals, a photodiode to measure the residual power of counter-propagating Raman pumps, and an OTDR, to detect the position of mechanical connectors. The overall fiber span is created connecting the different fiber spools through mechanical connectors. In this study, the fiber span is modeled by a set of physical layer parameters such as the total length, L_S, the entity and the position of the lumped losses along the span, l, the loss coefficient function, α, and the Raman gain coefficient curve, C_R. The Raman card is mounted in counter-propagating configuration by means of a circulator, containing a set of Raman pump lasers, each characterized by a specific frequency, launch power level, and polarization state, k_{pol}.

The experimental laboratory setup used to reproduce the single span scheme depicted in Fig. 2.10 is composed of the following devices:

- a commercial ILA, filling the whole C-band spectrum working in ASE mode;
- a couple of SSMF spools creating a span 100 km long (nominal length);
- a commercial Raman card composed of 5 independent counter-propagating Raman pumps;
- an OSA to measure both the transmitted and received spectra.

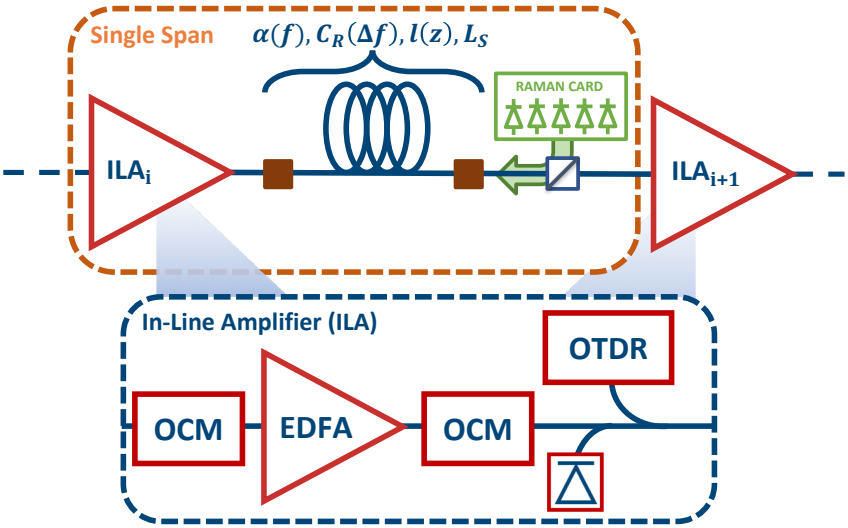

Fig. 2.10 C-band DRA using OCMs: sketch of the experimental setup.

2.5.2 Probing & Characterization Procedure

After hardware installation, the developed methodology plans to execute two consecutive optimization steps to make DRA operative: characterization of the fiber span, based on probing measurements of the physical system, and definition of the configuration of the DRA working point. In this section, only the first optimization phase is described, as the configuration design process is consistent with what is described in Sect. 2.3.2.

Probing Measurements

The aim of this optimization step is to retrieve the physical layer parameters that allow the model to match the experimental behavior of the system under fixed working conditions. The framework requires a specific set of measurements to get a complete overview of the system behavior.

Firstly, the OTDR scans the fiber span, detecting the position of all the lumped losses and the total length.

Then, the total loss at the frequency of the Raman pumps is measured by turning on each pump individually at the maximum power and reading the residual power at the other span terminal due to the photodiode.

Finally, an arbitrary number of on-off gain profiles are measured defining the Raman pump power configuration *a priori*, turning on the EDFA in order to have a propagating ASE full channel load and measuring the received spectrum through the OCM with the Raman pumps turned on and off. The on-off gain is computed through the operative definition in linear units as the ratio between the propagating power spectra on the DRA side with the Raman pumps turned on and off, respectively:

$$G_{OO}(f) = \frac{P^{\mathrm{ON}}(f, L_S)}{P^{\mathrm{OFF}}(f, L_S)}. \tag{2.18}$$

The shape of the produced ASE full-channel load does not impact the result of the methodology thanks to the use of OCMs. It is important to verify through the photodiode that the input ASE full-channel load power is low enough to not affect the Raman pump power evolution, achieving the undepleted pump condition. The number of measured on-off gain profiles has to be defined in order to probe different

working regions of the system, appropriately choosing the pump configurations according to the delivered total power.

Physical Layer Characterization

As mentioned, the set of physical layer parameters to optimize includes:

- loss coefficient function, α;
- Raman gain coefficient, C_R;
- lumped losses, l;
- polarization coefficient matrix, k_{pol};

The loss coefficient function is described through a phenomenological model using four parameters that take into account the Rayleigh scattering, the infra-red absorption and the fiber water peak [140], also reported in Sect. 2.2.1. The Raman gain coefficient curve is parametrized using two parameters which describe the concentration of Germanium in the fiber, determining the shape of the normalized curve, and the absolute scale factor of the profile [135]. The total number of lumped losses depends on the result of the OTDR analysis. Given its definition, the number of parameters to optimize the matrix of polarization coefficients is equal to $\sum_{i=0}^{N_P-1} i$, where N_P is the number of Raman pumps contained in the Raman card.

These parameters are jointly optimized by emulating at each iteration all the on-off gain profiles obtained in the predefined pump power configurations feeding the physical layer model with a single extracted set of physical parameters. The goodness of the solution is tailored on the following objective function:

$$\min \quad \sum_{j=1}^{N_{\mathrm{G}}} \sqrt{\sum_{i=1}^{N_{\mathrm{SAMPLE}}} \left[\mathrm{G}_j^{\mathrm{MEAS}}(f_i) - \mathrm{G}_j^{\mathrm{EMU}}(f_i) \right]^2}, \tag{2.19}$$

where N_{G} is the number of measured on-off gain profiles, N_{SAMPLE} is the number of evaluated points of the spectrum, $\mathrm{G}_j^{\mathrm{MEAS}}$ is the j-th measured profiles obtained using a specific pump power configuration and $\mathrm{G}_j^{\mathrm{EMU}}$ is the corresponding emulated profile. The optimal set of physical parameters must emulate with the lowest possible error the measured gain profiles according to the different pump configurations.

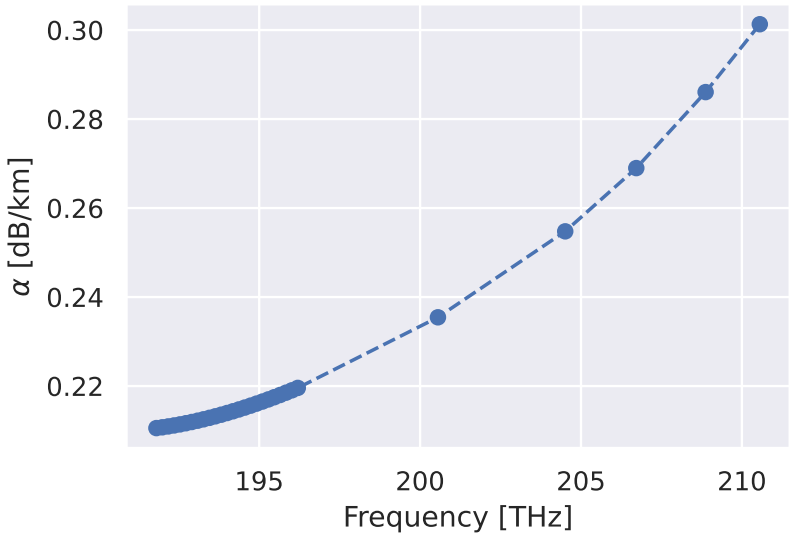

Fig. 2.11 C-band DRA using OCMs: characterization result of the loss coefficient function.

Table 2.2 C-band DRA using OCMs: characterization result of the lumped losses.

$l(z=0)$ [dB]	$l(z=50.3\,\text{km})$ [dB]	$l(z=101.3\,\text{km}=L_S)$ [dB]
0.952	0.958	0.954

Table 2.3 C-band DRA using OCMs: characterization result of the polarization state

	P_1	P_2	P_3	P_4	P_5
P_1	0	1.6481	1.3318	1.4736	0.8465
P_2	1.6481	0	0.0005	0.0058	0.0156
P_3	1.3318	0.0005	0	0.5724	0.01559
P_4	1.4736	0.0058	0.5724	0	1.68794
P_5	0.8465	0.0156	0.01559	1.68794	0

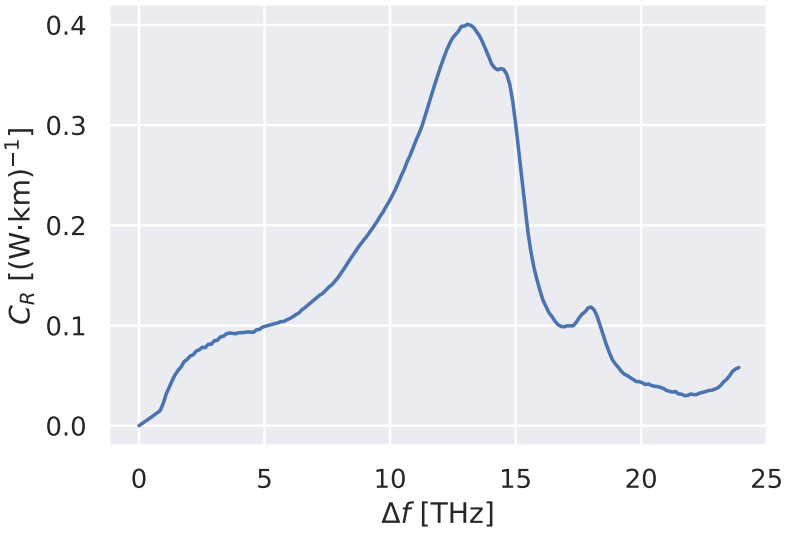

Fig. 2.12 C-band DRA using OCMs: characterization result of the Raman gain coefficient.

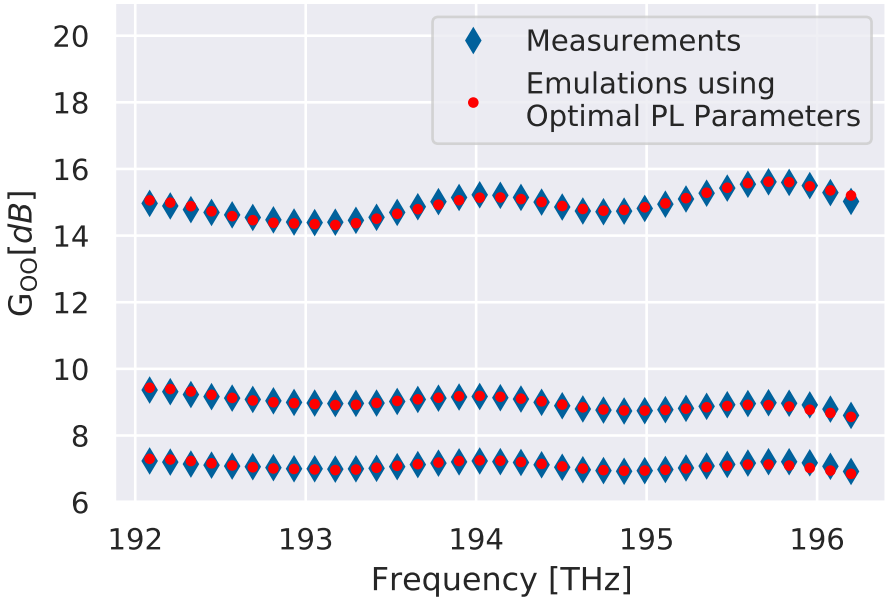

Fig. 2.13 C-band DRA using OCMs: characterization result of the measured on-off gain profiles at three different power regimes. In turn, all the Raman pumps at the relative maximum launch power level, 130 mW and 100 mW (blue diamonds). The emulated on-off gain profiles using the corresponding Raman pump configuration and the optimal set of physical layer (PL) parameters are represented by the circled red markers.

This formulation allows to fully characterize the DRA, probing its behavior within the specific scenario, and addressing the definition of the optimal set of physical layer parameters in the direction of an equivalent representation of the system based on the chosen physical layer model.

2.5.3 Results

First, the results obtained during the physical layer characterization are reported. In particular, the derived loss coefficient function and the Raman gain coefficient curve are depicted in Figs. 2.11 and 2.12, the OTDR analysis and the estimated lumped losses are shown in Tab. 2.2, the extracted polarization matrix is reported in Tab. 2.3. To obtain this set of physical layer parameters, three on-off gain profiles have been measured configuring the pumps at three different power regimes. Fig. 2.13 shows the comparison between the emulations performed with the optimal set of physical layer parameters and the measured on-off gain profiles obtained setting all the pumps, respectively, at the maximum values, 130 mW and 100 mW. This choice of the launch pump power configurations satisfactorily inspects the dynamics of the Raman amplifier and to keep the optimization time limited, which increases with the number of on-off gain profiles to emulate. In the considered case, the physical layer characterization takes a variable time to finish the optimization which is of the order of tens of minutes.

Then, to test the effectiveness of the methodology, the launch pump power configuration design process described in Sect. 2.3.2 is performed for all pairs of targets derived from the combination of 10, 11, 12 dB as gain values and -0.2, 0.0, 0.2 dB/THz as the tilt. The optimization time of the design process using five Raman pumps is less than one minute for all the evaluated configurations. Tab. 2.4 contains all designed pump power configurations for each couple of given targets, reporting the maximum power value and frequency of each pump. The complete set of measured and emulated on-off gain profile is depicted in Fig. 2.14 and the relative summary of some aggregated metrics is reported in Tab. 2.5. Observing the experimental results, the designed Raman pump power configurations correctly produce the required mean gain, presenting a slight positive tilt offset with respect to the targets. Ripple values are limited below 0.7 dB, showing a satisfactory degree of flatness around the linear regression of the profile. When comparing the predicted

Table 2.4 C-band DRA using OCMs: designed pump power configurations.

Pump Number		#1	#2	#3	#4	#5
G_{tar} [dB]	T_{tar} [dB/THz]	Pump Power Levels [mW]				
10	-0.2	161.4	113.7	171.0	130.3	166.0
11	-0.2	179.6	105.3	198.2	145.7	202.3
12	-0.2	180.0	130.0	200.0	171.7	228.8
10	0	176.0	64.3	176.0	150.3	199.2
11	0	151.9	98.3	186.0	161.3	220.9
12	0	152.0	112.4	200.0	180.9	248.5
10	0.2	179.9	20.4	180.6	168.2	230.7
11	0.2	156.6	53.8	191.0	178.1	253.6
12	0.2	138.8	86.5	198.3	192.9	273.5
		Pump Maximum Power Levels [mW]				
		180.0	130.0	200.0	320.0	360.0
		Pump Frequencies [THz]				
		200.6	204.5	206.7	208.9	210.6

Table 2.5 C-band DRA using OCMs: result analysis.

G_{tar} [dB]	T_{tar} [dB/THz]	$\overline{G_{OO}}$ [dB]	$m_{G_{OO}}$ [dB/THz]	ΔG_{OO} [dB]	RMSE [dB]	E_{MAX} [dB]
10	-0.2	10.0	-0.159	0.5	0.09	0.24
11	-0.2	11.0	-0.155	0.6	0.10	0.25
12	-0.2	11.9	-0.166	0.6	0.08	0.20
10	0	10.0	0.045	0.6	0.10	0.27
11	0	10.9	0.0214	0.7	0.10	0.16
12	0	11.9	0.012	0.7	0.11	0.18
10	0.2	10.0	0.258	0.7	0.12	0.28
11	0.2	10.9	0.234	0.7	0.14	0.22
12	0.2	11.9	0.205	0.7	0.16	0.27

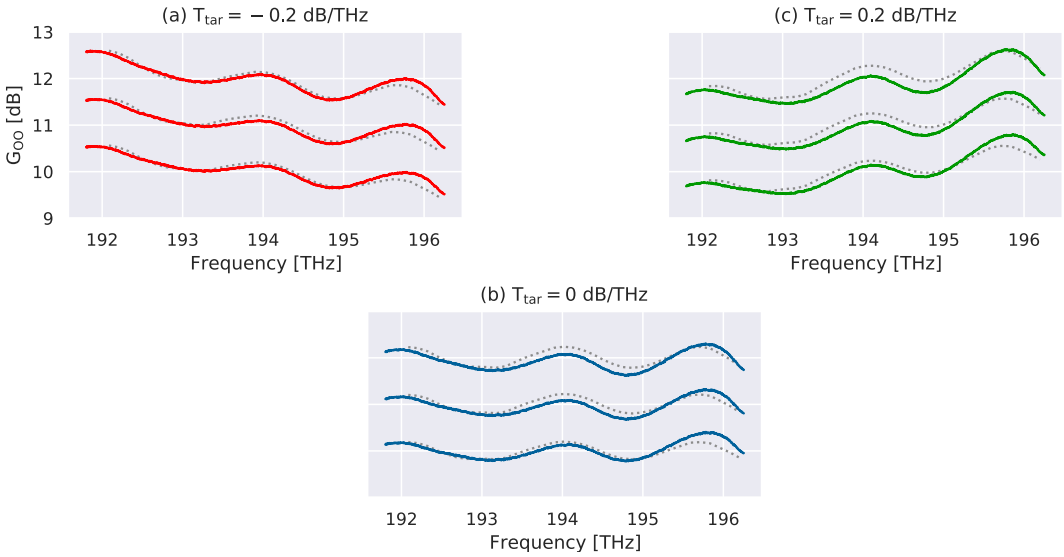

Fig. 2.14 C-band DRA using OCMs: measured (solid line) and emulated (dot line) on-off gain profile for each designed pump power configuration.

and measured profiles, the maximum absolute error, E_{MAX}, is on average 0.23 dB. Regarding Root-Mean-Square Error (RMSE), the discrepancy between profiles increases when a positive tilt is required, since Raman pumps at high frequencies deliver a higher amount of power. In this condition, the interaction between pumps is more intense, and the effective on-off gain profile is more affected by the uncertainty related to the deduced physical layer parameters.

For this use case, it was considered essential to focus on the characterization procedure that led to the power configurations designed for the Raman pump. For this reason, the compensation due to the introduction of a channel WDM comb was not verified. This aspect will be considered again in the next section of the study.

2.6 C+L Band DRA using Optical Channel Monitors

As the last use-case, a controller architecture is presented for managing multiband Raman amplification, in particular a C+L band scenario, on a single fiber span exploiting OCMs. Even in this case, the physical parameters of the fiber needed by the DRA controller for correct operation of the system are extracted through a conceived probing and characterization procedure. The proposal shows a high degree of adaptability of such defined DRA to the particular field scenario in which

it is deployed, also counteracting spectral load modifications. The structure of the proposed procedure for the physical layer characterization enables the extension of the controller usage for both single- and multi-band scenarios, facing up issues related to modifications of the spectral load or of the physical layer and providing a valuable solution for real-time applications. The behavior of the described system is validated by means of an experimental session, confirming the effectiveness of the controller architecture design and the high achieved performance accuracy.

As discussed in Sect. 2.4, the deterministic SLSQP minimization method is adopted for the configuration design [136] in favor of the reproducibility of the optimization process starting from the same input values.

2.6.1 Experimental Setup

The experimental equipment used to investigate the considered multi-band scenario is reported in Fig. 2.15. The input WDM spectrum is generated by means of a CW DFB laser comb, without losing generality, as the SRS is sensitive only to the average power level propagating through the fiber span. In particular, two input WDM spectra are created in the L-band (38 channels) and the C-band (36 channels), and the final WDM spectrum is generated using a C+L coupler. The introduction of Variable Optical Attenuators (VOAs) rigidly changes the input spectrum powers in both the C and L bands. Connecting 2 SSMF spools of 60 km and 25 km nominal lengths, a fiber span of 85 km total nominal length is built.

On the receiver side, 5 counter-propagating Raman pumps controlled in power with frequencies spread in a frequency range between 200 and 211 THz are introduced by means of an optical circulator. To emulate the presence of OCM telemetry devices, an OSA is used at both fiber span terminals.

2.6.2 Probing & Characterization Procedure

As premises, since the context under investigation is a multi-band transmission scenario, it requires the non-flat frequency response of the optical devices involved in the optical propagation along the fiber span together with a careful characterization. The following procedure has been conceived to guarantee flexibility to the system operation without making its application complex or time-consuming, deriving the

parameters by respecting a procedural sequence rather than an optimization phase. To do this, some simplifications regarding the acquisition of the Raman gain coefficient are adopted. In particular, the shape of the Raman gain coefficient profile is assumed to be known, and only the scaling factor of this curve is characterized by probing the physical layer [137]. Given this assumption, as in Sect. 2.4, the Raman gain coefficient is rewritten in the following form:

$$C_R(\Delta f) = K_R \, c_R(\Delta f) \, , \tag{2.20}$$

where K_R is the Raman gain coefficient scaling factor, expressed in $(\mathrm{m} \cdot \mathrm{W})^{-1}$, and c_R is the normalized Raman gain coefficient curve describing the SRS intensity.

The procedure of probing measurements and characterization is described in five different steps that aim to derive the parameters of the physical layer required by the DRA controller to manage the amplification system. In turn, the retrieved parameters are:

- the lumped losses along the fiber span, l;
- the loss coefficient function for the pump frequencies, $\alpha(f_p)$;
- the Raman gain coefficient scaling factor, K_R;
- the loss coefficient function for channel frequencies, $\alpha(f_{ch})$;
- the gain and tilt correction parameters, $\overline{G_{OO,cor}}$ and $m_{G_{OO},cor}$.

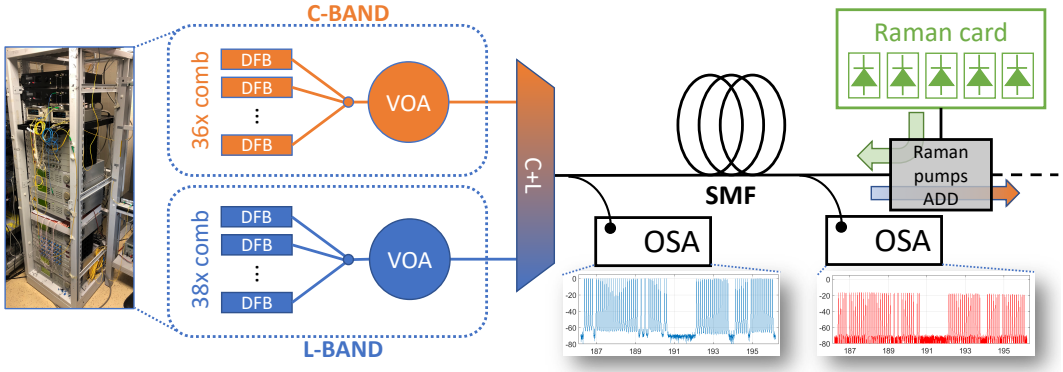

Fig. 2.15 C+L band DRA using OCMs: experimental equipment at the Optical Networks and Photonics Lab of LINKS Foundation, Turin.

OTDR Analysis

Firstly, an analysis of the fiber link is made through an OTDR, detecting the lumped losses, l, such as splices, connectors and non-idealities. If OTDR is not available, the contribution of the lumped losses is taken into account within the fiber loss coefficient function as a distributed effect.

Measurements with Back-Reflection Photodiode

Using the back-reflection photodiode at the input fiber span terminal, the loss coefficient function is evaluated at the Raman pump frequencies. This step is performed by singularly propagating only each Raman pump through the optical fiber span. The loss coefficient function for Raman pump frequencies is calculated in logarithmic units as follows:

$$\alpha(f_p) = \frac{P(f_p, L_S) - P(f_p, 0) + \sum l(z)}{L_S} \,, \tag{2.21}$$

where $P(f_p, L_S)$ is the launch power of the specific Raman pump, $P(f_p, 0)$ is the power measured by the back-reflection photodiode, $\sum l(z)$ is the sum of the concentrated loss.

Pump & Probe Measurements

A set of pump-and-probe measurements is performed in order to determine the Raman gain coefficient scaling factor value, K_R. For each Raman pump, the measurement is done using the channel that maximizes the Raman coupling as a probe, so that $\Delta f \approx 13$ THz, measuring the corresponding on-off gain. As this set of measurements involves one single channel, it is reasonable to assume undepleted pump [108] and so the Raman gain coefficient can be evaluated from the following equation [134]:

$$C_R(f_p - f_{ch}) = \frac{\ln(G_{OO}(f_{ch}))}{L_{eff}(f_p) P(f_p, L_S)} \,, \tag{2.22}$$

where L_{eff} is the fiber effective length at the specific Raman pump frequency (see Eq. 2.14). The final K_R is estimated by averaging the derived values.

Full Spectral Load Propagation

This step estimates the loss coefficient function for channel frequencies, α, with the Raman pumps turned off. In particular, the algorithm consists of:

- propagating the full spectral load along the fiber span;
- acquiring the power spectra at the input, $P^{\mathrm{OFF}}(f,0)$, and output, $P^{\mathrm{OFF}}(f,L_S)$, of the fiber span through OCMs;
- evaluating the tilt of the received spectrum, m_{P_S}, as slope of the profile linear regression;
- estimating the average loss coefficient, $\overline{\alpha}$, by means of the following formula:

$$\overline{\alpha} = \overline{\left(\frac{P^{\mathrm{OFF}}(f,0) - (P^{\mathrm{OFF}}(f,L_S) + \sum l(z))}{L_S} \right)} \; ; \tag{2.23}$$

- emulating the inter-channel Raman cross-talk with the introduction of the average loss coefficient function, $\overline{\alpha}$, and the derived Raman gain coefficient profile;
- computing the power difference between the effective received spectrum, $P^{\mathrm{OFF}}(f,L_S)$, and the emulated one, $P^{\mathrm{OFF,EMU}}(f,L_S)$, (in logarithmic units):

$$\Delta P(f,L_S) = P^{\mathrm{OFF}}(f,L_S) - P^{\mathrm{OFF,EMU}}(f,L_S) \; ; \tag{2.24}$$

- extracting the complete loss coefficient function, α, as:

$$\alpha(f) = \left(\frac{\Delta P(f,L_S)}{P^{\mathrm{OFF}}(f,L_S)} + 1 \right) \overline{\alpha} \; . \tag{2.25}$$

Eq. 2.25 refers to the extraction of the loss coefficient vs. frequency, starting from the difference between experimental results and emulation done with flat loss coefficient (see Eq. 2.24). This process estimates the loss coefficient profile with a single measurement, also using as an alternative to a WDM comb spectrum a spectral load generated by a full channel with ASE noise.

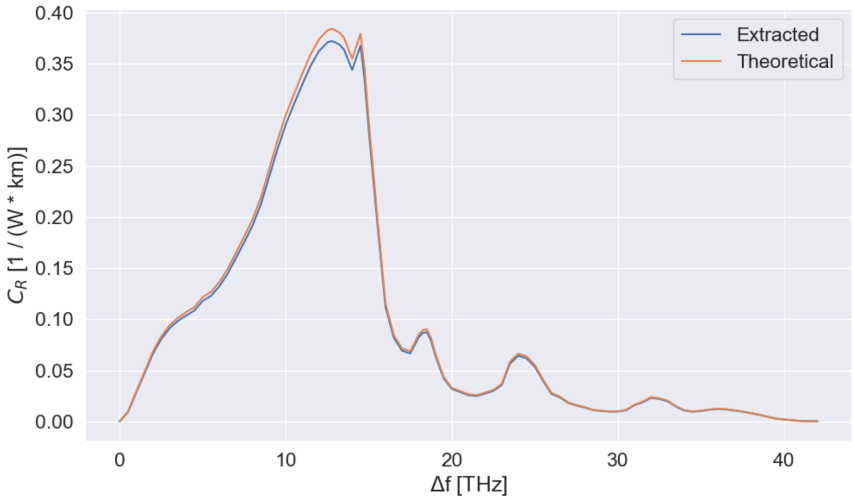

Fig. 2.16 C+L band DRA using OCMs: characterization result of the Raman gain coefficient profile.

Table 2.6 C+L band DRA using OCMs: characterization result of the lumped losses.

Loss Intensity [dB]	Loss Position [km]
0.2	0.0
0.2	61.1
0.3	86.1

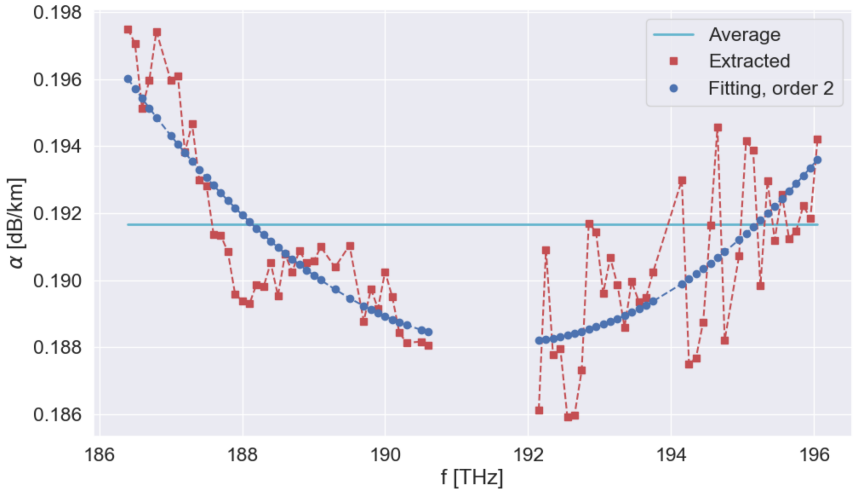

Fig. 2.17 C+L band DRA using OCMs: algorithmic steps for deriving loss coefficient function at channel frequencies.

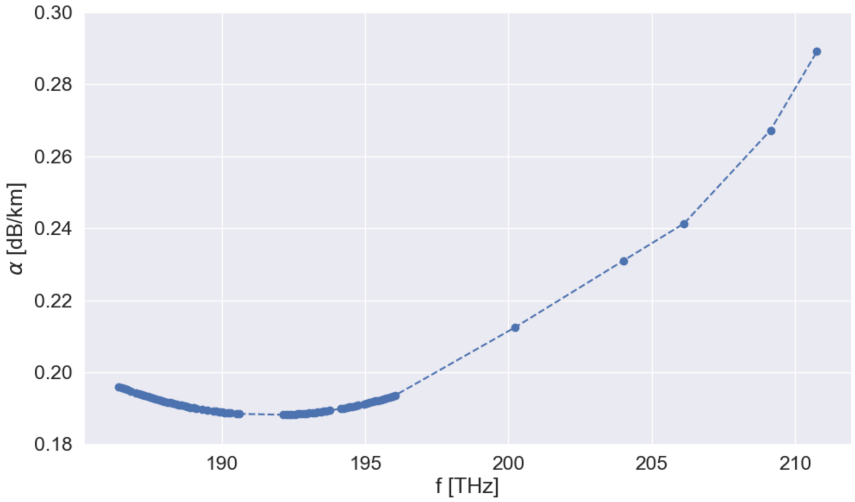

Fig. 2.18 C+L band DRA using OCMs: characterization result of the loss coefficient function.

Table 2.7 C+L band DRA using OCMs: Raman pump power configurations (sorted by decreasing frequency).

G_{tar} [dB]	#1 [mW]	#2 [mW]	#3 [mW]	#4 [mW]	#5 [mW]
8	198.5	150.0	133.5	39.3	91.7
9	224.4	177.0	148.3	42.9	95.1
10	241.2	212.8	164.5	46.2	100.9

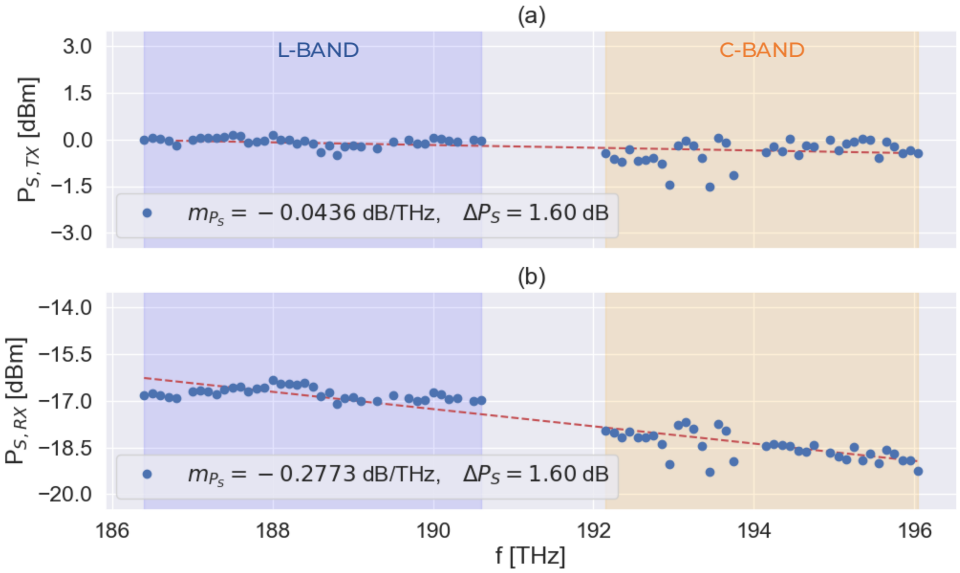

Fig. 2.19 C+L band DRA using OCMs: peaks of the propagated WDM C+L comb with Raman pumps turned off: (a) input spectrum, (b) output spectrum.

Optimization at Maximum Gain

In order to finalize the procedure, a first Raman amplification optimization is performed at the maximum gain target achievable by the system on the full spectral load. After optimization, the average on-off gain, $\overline{G_{OO}}$, and the tilt, $m_{G_{OO}}$, are evaluated using telemetry devices. These data are compared with the target values, and the following correction parameters are computed:

$$\begin{aligned} \overline{G_{OO,cor}} &= \mathrm{G_{tar,MAX}} - \overline{G_{OO}} \ , \\ m_{G_{OO},cor} &= \mathrm{T_{tar}} + m_{G_{OO}} \ . \end{aligned} \tag{2.26}$$

Generally, $\mathrm{T_{tar}}$ is set to 0 dB/THz because the purpose of the optimization is to restore the flatness of the propagating spectral load at the input of the next fiber span. The purpose of this final probing step is to center the virtual gain mask produced by the optimization framework at the proper working point, allowing RCU to perform the linearization algorithm correctly. For this reason, the correction parameters are offset values, with which the controller modifies the control plane target values in order to fill the lack of knowledge of the physical layer and compensate for the uncertainties caused by depletion effects.

2.6.3 Results

Tracing the steps of the proposed procedure, the results achieved from the probing and characterization of the experimental equipment are shown.

The OTDR analysis performed on the fiber span is reported in Tab. 2.6. Reasonably, there are two insertion losses placed at both fiber span terminals due to the input connector and the output splitter, and an intermediate lumped loss due to fiber spools connector.

In the prosecution, the derived scaling factor of the Raman gain coefficient is depicted in Fig. 2.16. Following the loss coefficient function at pump frequencies, the pump-and-probe measurements accurately estimate the strength of the Raman amplification coupling, comparing the extracted value with respect to the theoretical one.

The algorithmic steps for the channel loss coefficient function are reported in Fig. 2.17. The graph clearly expresses the mathematical meaning of Eq. 2.25:

starting from the straight light blue line representing the flat average loss coefficient function, $\overline{\alpha}$, the frequency content, drawn with squared red markers, is extracted by exploiting the power difference $\Delta P(f_{ch}, L_S)$, between the real received spectrum and the received one emulated using the average, $\overline{\alpha}$. In order to smooth the profile trend, the extracted curve undergoes a polynomial second-order fitting, represented by circled blue markers. The result that summarizes the complete extracted loss coefficient function considering both channels and pumps is reported in Fig. 2.18. As the last step, the correction parameters are extracted according to Eq. 2.26 after a system optimization at 10 dB gain and flat power spectrum tilt.

After the calibration phase, an experimental session is dedicated to verify the operation of the conceived DRA controller architecture.

Firstly, the WDM spectrum is acquired turing off all Raman pumps (see Fig. 2.19). Having an almost flat input WDM spectrum roughly at 0 dBm of power per channel, this measurement captures the information regarding the output WDM spectrum tilt, m_{P_S}, useful to emulate the amplification target in gain and tilt. So, by defining the tilt target to 0.2774 dB/THz, three different requests of the control plane are emulated, requiring gain targets of 8, 9 and 10 dB. These values of the gain target are chosen since they represent challenging tasks for DRA, recovering more than half of the total fiber loss.

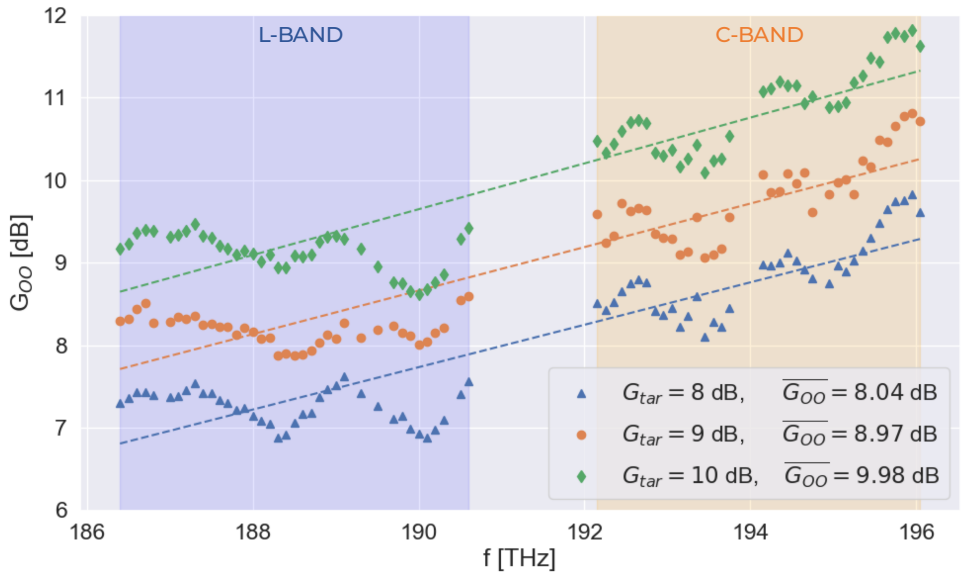

Fig. 2.20 C+L band DRA using OCMs: measured on-off gain profiles with relative metrics.

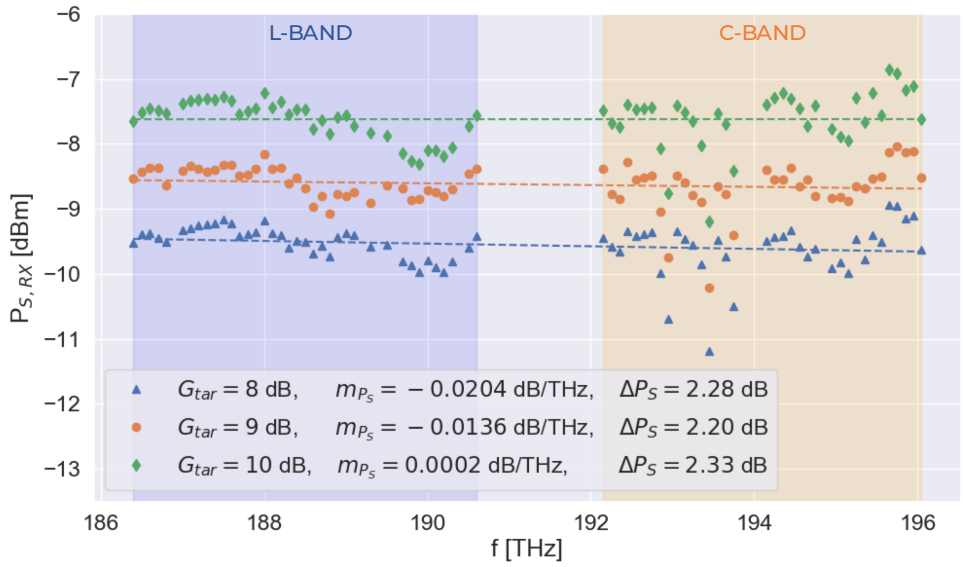

Fig. 2.21 C+L band DRA using OCMs: measured peaks of the output WDM spectra with relative metrics.

Provided amplification targets to the DRA controller, the system starts computing the corresponding optimal Raman pump power configuration. Subsequently, it sets the Raman pumps at the designed working point, and the gain target is aimed within a tolerance of a tenth of dB, linearizing the problem around the optimum working point. The power configurations of the Raman pump achieved are reported in Tab. 2.7. The complete set of experimental results is illustrated in Figs. 2.20 and 2.21. Fig.2.20 displays how the gain target has been successfully obtained within the tolerance range required for each tested scenario. On the other hand, by observing Fig. 2.21, the required tilt is also achieved in all cases. Only a residual 0.2 dB tilt on 10 THz is observed. For all cases, the increase in ripple of the power profile is less than 1 dB.

2.7 Concluding Remarks

In this chapter, the case of the counter-propagating distributed Raman amplifier for cognitive optical networking applications has been investigated. In particular, a software architecture has been proposed which autonomously allows the amplification system to be configured so as to guarantee the achievement of the targets required by the optical control plane. Then, three different transmission scenarios which differ in terms of available telemetry devices (e.g. integrated photodiodes, OCMs)

and input spectrum (single or multi-band) were tackled, proposing for each one a procedure which allows characterizing the physical parameters necessary for the physical model by probing the physical layer by means of the telemetry devices. The efficiency of the procedures has been experimentally tested by measuring the performance achieved by the amplifier in terms of average gain, tilt, and ripple.

As expected, the achieved accuracy depends both on the amount of information that the telemetry devices supply - determining a different processing of the data - and on the portion of the bandwidth that is exploited, involving a consequent impact of the nonlinear effects of the SRS.

The case under investigation appears to be extremely sensitive to the characteristics of the physical layer and therefore to its variations. For this reason, it requires a refinement of the dedicated configuration according to the specific context in which it works. Imagining the use of cognitive networks, this system is proving to be perfectly suitable, expecting to significantly improve its autonomous management within a centralized SDN.

Chapter 3

The Optical Line System Case

This chapter investigates the application of cognitive techniques in optical networks at the physical layer, defining a vendor-agnostic optical line controller architecture capable of autonomously setting the working point of optical amplifiers to maximize the capacity of the optical link. The presented framework is based on an automatic line characterization procedure, span-by-span, to abstract the properties of the physical layer, using the monitoring devices present in each amplification site, such as OCMs and OTDR. Similarly to the case of DRA analyzed in the previous chapter, the presented methodology aims to determine the physical properties of the specific optical fiber section, probing them through the introduction of optical power at different power levels. Based on the characterization performed, an optimization algorithm determines the working point of each amplifier to obtain the highest and flattest Signal-to-Noise Ratio (SNR) for each channel. This strategy derives from the context for which the methodology is developed, that of metro and core transparent meshed optical networks, with a medium- or long-haul, in which for the determination of a LP there are no disparities in the choice of the channel wavelength.

In the current chapter, the optical amplifiers used during the experiments and considered in the various simulation campaigns are commercial dual stage EDFAs controllable by setting gain and tilt, equipped with Gain Flattening Filter (GFF) between the two amplification stages.

The entire system has been experimentally tested in laboratory using different optimization strategies, showing interesting behaviors and excellent matches with respect to emulation results. Furthermore, the investigation on the capabilities of

the software structure has been extended through simulations, expanding the set of optimization strategies and the available telemetry.

The main tools used within the framework are the GNPy open source library, used as a physical model for optical propagation through the fiber, and the CMA-ES, used as an optimization algorithm to identify properties of each fiber span and to maximize the link capacity. In the next chapter, a complete and generic network-level control framework is defined to understand how the control of a single optical line system can be orchestrated within a partially disaggregated network context.

In the discussion, the contents are taken from the following publications: [141–143, 140, 144, 145].

3.1 System Architecture

An Optical Line System (OLS) is considered as a subsystem of a partially disaggregated optical network, shown in Fig. 3.1. In the considered framework, Optical Network Controller (ONC) is assumed to have direct access to Transceivers (TRXs) and ROADMs for route-wavelength assignment and LP deployment purposes. The ROADM and the collection of TRXs placed in a specific location within the geographical footprint of the optical network identify an optical node.

However, the management of OLSs, identified by the ROADM-to-ROADM physical connections including both Booster (BST) and Pre-amplifier (PRE), is delegated to a single Optical Line Controllers (OLCs), which establishes direct communication with all the amplifier controllers – also the ILAs – and the additional telemetry devices placed at each amplification site. Furthermore, each OLC autonomously evaluates and sets the optimized working points of the amplifiers, providing to the

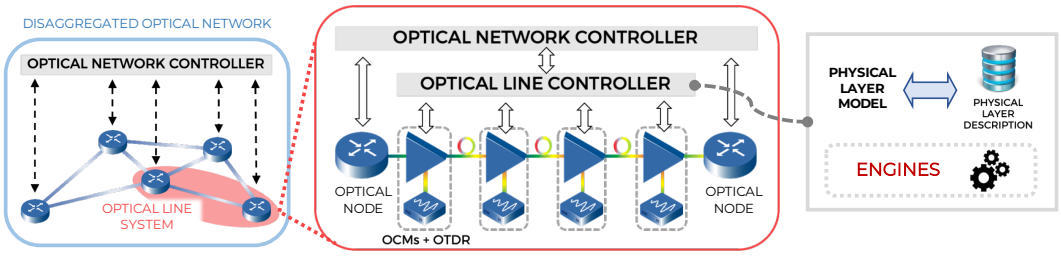

Fig. 3.1 Conceived ROADM-to-ROADM optical line system architecture within a partially disaggregated optical network.

ONC the QoT metrics required for the LP computations. The definition of the working point of the amplifiers takes place by combining the information probed from the physical layer through telemetry and the use of algorithms (which are called engines below) through the adoption of a set of physical models that reproduce the optical behavior propagation of the system.

3.2 Optical Propagation Modeling

In this section, the optical propagative behavior of the devices that make up an OLS is described in terms of modeling and key parameters. This will be considered hereinafter in the methodology developed, and includes the generation of ASE noise of the optical amplifiers and NLI impairment due to the fiber. In addition, it describes how to characterize and measure the performance of an optical TRX.

In this work, PDL [146] and the filtering penalties [147] due to ROADMs are neglected, as the scenarios faced experimentally and in simulation present valid conditions for their assumption. Moreover, CD and PMD are assumed to be fully compensated for by receiver DSP [148]. It is known that such degradations do not introduce penalties below a certain threshold of accumulated metrics, after which it is necessary to take into account their effect as an additional penalty.

3.2.1 Amplified Spontaneous Emission & EDFA Behavior

The ASE noise generation turns out to be a prominent impairment in optical transmission systems, associated with optical amplification, serving the purpose of restoring signal power while introducing ASE noise as an undesired byproduct in terms of optical propagation performance [149]. The ASE noise can be represented as AWGN with a bilateral Power Spectral Density (PSD), $\mathrm{G_{ASE}}$, which incorporates both polarization states [149, 150]. It can be quantified using the following formula in linear units:

$$\mathrm{G_{ASE}}(f) = hf\ \mathrm{NF}(f)\ [G(f) - 1]\ . \tag{3.1}$$

In the equation, h is the Planck constant, NF indicates the amplifier noise figure, and G represents the amplifier gain.

It should be noted that this equation is primarily applicable to EDFAs [151], but similar principles apply to other amplification techniques such as pure Raman amplification or Hybrid Raman-EDFA Amplifiers (HFAs) [98, 101]. EDFAs employ erbium-doped fiber as the active medium, allowing population inversion through the use of 980 nm or 1480 nm optical pump lasers [151]. This population inversion facilitates stimulated emission, resulting in signal amplification. However, population inversion also leads to spontaneous emission, which contributes to the generation of ASE noise. EDFAs can be designed as needed based on the desired gain dynamics and the noise figure produced. There are various configurations ranging from single-stage to multi-stage schemes [152, 31]. The latter reach higher gain, while still managing to compensate for the distortion between the various wavelengths thanks to the introduction of specific filters called GFFs between the various stages. They are specially designed to achieve a flat gain profile by compensating for defects generated by the absorption/emission curves of erbium-doped fibers. Additionally, the introduction of programmable filters into the architecture allows you to fine-tune the gain profile channel by channel by implementing a technique called Dynamic Gain Equalization (DGE) [153].

The noise figure parameter, NF, plays a vital role in describing the amplifier performance. It is related to the spontaneous emission factor, $n_{sp} > 1$, which is influenced by the atomic populations in the ground and excited states of erbium atoms [149], allowing to determine the noise figure as:

$$\mathrm{NF}(f) = 2\, n_{sp}(f)\ . \tag{3.2}$$

In long-haul optical communications, Raman amplifiers and HFA are often utilized alongside EDFAs to improve noise performance. Raman amplifiers introduce Raman pumps into the fiber to activate it as an active medium, while HFAs combine Raman amplification and EDFAs to minimize the overall noise impact. For each amplification system, the equivalent noise figure can be estimated [154].

By incorporating the appropriate gain and noise figure parameters, each amplifier can be characterized in terms of its amplification and noise characteristics. The frequency behavior of both the gain profile and the noise figure depends on the architecture of the amplifier, the design, and the manufacturing process used to make each amplifier. In fact, given the functions available for the control systems of these devices, it is possible to manage the average gain and the tilt of the generated gain

profile. However, both the latter and the noise figure actually exhibit deviations from the expected behavior, recognizable by the ripple measured against the linear regression of the profiles [155, 156]. In addition to the cascade of different active media and filters, the real gain profile produced by the device is mostly affected by the spectral hole burning phenomenon [157]. The output power of an amplifier for a given signal with a certain input power can be calculated as:

$$P^{\mathrm{OUT}}(f) = P^{\mathrm{IN}}(f)\, G(f)\,. \tag{3.3}$$

Achievement of the required gain is guaranteed up to the maximum output power level, P^{SAT}, after which the amplifier falls back into an operating zone called saturation, in which the device dynamics is limited.

The ASE noise power can be computed using the formula:

$$P_{\mathrm{ASE}}(f) = hf\,\mathrm{NF}(f)\,\left[G(f)-1\right]\,B_n\,, \tag{3.4}$$

where B_n is the noise bandwidth, often equivalent to the channel symbol rate, R_s, which represents the spectral occupation of the modulated signal.

3.2.2 Non-Linear Interference Noise Generation

The NLI noise generation is another significant impairment in optical communication systems, arising from the non-linear properties of optical fibers. It has become a critical challenge in high-speed transmission scenarios, impacting overall system performance. The NLI occurs due to the Kerr effect [158–160], where the refractive index of the fiber core changes in response to the intensity of the transmitted light. This effect leads to a nonlinear phase modulation of the optical signal, which results in distortion of the received symbols.

Focusing on the main parameters influencing the NLI generation [130, 161], the fiber nonlinear coefficient, γ, expressed in units of $(\mathrm{W{\cdot}m})^{-1}$ quantifies the strength of the Kerr effect. In addition, NLI is also influenced by CD, referring to the phenomenon in which different wavelengths of light travel at different speeds in the fiber and cause the optical pulse to spread. The exacerbation of non-linear interference occurs when there is time overlap between pulses. From a practical perspective, optical fiber manufacturers provide information on the dispersion parameter in the

fiber data sheets, D. This parameter is presented as a function of the wavelength of the optical pulse and helps characterize the dispersion properties of the fiber. It is related to the chromatic dispersion coefficient, β_2, which represents the second derivative of the mode propagation constant, β, expanded using the Taylor series with respect to the central frequency of the pulse. The symbol rate, also known as the baud rate, R_s, is related to NLI, representing the number of symbol changes per second. The symbol rate determines the rate at which the transmitted signal is modulated and affects the overall performance of the system, including the effects of NLI. Another parameter of interest is the noise bandwidth, B_n, which characterizes the spectral range over which NLI-induced noise is spread. The choice of the noise bandwidth considered is mostly due to the shape of the pulse, the symbol rate, and the limitations of the system bandwidth.

To accurately model and predict the impact of NLI impairment, various mathematical models have been developed. Two widely used models are the Gaussian Noise (GN) model [162] and one of its variations, which is the Generalized Gaussian Noise (GGN) model [163, 164], both of them implemented in GNPy [96, 88]. These models provide valuable information on NLI behavior and aid in evaluating the performance of the system. In the GN model, NLI is treated as an additive noise term that follows a Gaussian distribution, where Gaussian distributed signals are assumed and the non-linearity is a perturbation of the propagating electric field. This model assumes that the NLI-induced noise is uncorrelated with the signal and has a constant power spectral density. While the GN model offers a simplified representation of NLI, it fails to capture the statistical dependencies between the signal and SRS. These dependencies become critical as the occupied bandwidth expands, allowing SRS to play a dominant role. On the other hand, the GGN model incorporates the statistical dependencies between the signal and NLI, providing a more accurate representation of the impairment including frequency-dependent attenuation and SRS. It considers the joint probability distribution of the signal and the NLI, which is modeled as a bivariate Gaussian distribution. The GGN model takes into account the correlation between the signal and the NLI, allowing a more realistic assessment of the performance of the system.

3.2.3 Transceiver Characterization and Performance Measuring

Optical TRXs enable the efficient transmission of data over long distances in modern optical communication systems. These devices rely on several key concepts to ensure high-capacity and reliable data transfer.

Typically, data are encoded using modulation schemes such as Quadrature Amplitude Modulation (QAM), using the in-phase and quadrature components to represent the corresponding amplitude and phase of the optical signal [165]. By manipulating these components, multiple bits can be transmitted simultaneously, increasing the data rate. In addition, the management of polarization states is also added to transmit information faster by packing more bits. In fact, Polarization Multiplexed (PM)-QAM allows the transmission of two orthogonal polarization states simultaneously, effectively doubling the data capacity of the optical channel. M-QAM schemes are frequently used in optical TRXs, where M represents the cardinality or number of points in the constellation diagram. Higher cardinality schemes, such as 64-QAM or 256-QAM, offer increased data rates, but are more susceptible to impairments such as noise and fiber nonlinearity.

To shape the transmitted signal in a way that minimizes inter-symbol interference, the Root-Raised Cosine (RRC) shape is commonly utilized, also ensuring a smooth transition between symbols and maximizing spectral efficiency. The main parameter characterizing the RRC shape is the roll-off, ρ. Another possibility to achieve the same goal is to generate a spectrum of channels with a sinc shape.

To further increase the capacity of optical communication systems, WDM techniques are used, which allow the transmission of multiple signals simultaneously by assigning each signal to a unique spectral slot. These spectral slots can be organized using either a *fixed* or *flexible* grid, depending on the specific requirements of the system. The flexible grid provides more efficient utilization of the available spectrum, while the fixed grid simplifies the design of transceivers and network elements.

At the receiver end, demodulation of the received optical signal is performed to extract the transmitted data [166]. This process involves DSP techniques, which employ algorithms to mitigate impairments, including CD, PMD, and non-linear effects [167].

Lastly, the use of Forward Error Correction (FEC) is employed to enhance the robustness of the optical transmission system, introducing redundancy into

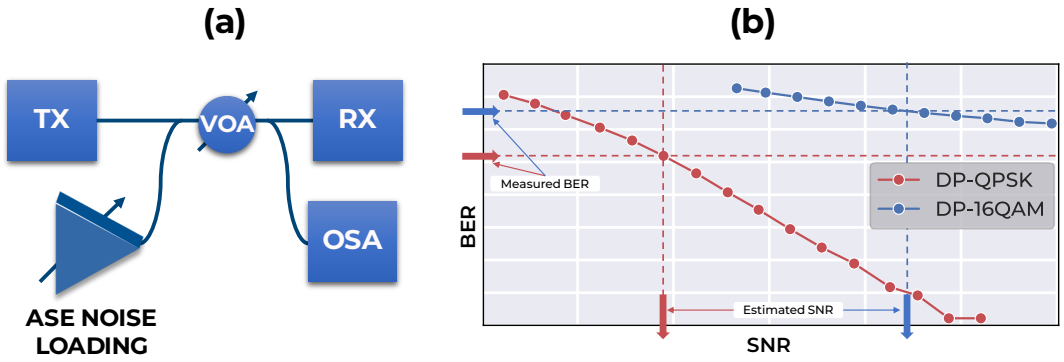

Fig. 3.2 (a) Setup scheme for the B2B characterization of a TRX. (b) SNR estimation procedure using TRX B2B curves given the measured BER.

transmitted data and allowing the receiver to detect and correct errors [168]. System performance can be evaluated both pre-FEC, where the raw bit error rate is measured, and post-FEC, where the error rate after FEC decoding is assessed.

To evaluate the performance of optical TRXs, Back-to-Back (B2B) characterization measurements are commonly conducted, directly connecting the transmitter and receiver without any intermediate transmission fiber to assess the fundamental performance limits of the transceiver [169]. These measurements provide information on achievable data rates, signal quality, and power budget (see Fig. 3.2).

Fig. 3.2-a shows the scheme of the experimental apparatus commonly used for this characterization procedure, where TX and RX represent the terminals of the TRX [170, 171]. For each BER measurement, an amount of optical ASE noise is introduced by means of an EDFA varying its gain. The OSNR is measured by a differential measurement between the signal strength peak and the floor using an OSA. Furthermore, VOA determines the power range necessary for the receiver to avoid further penalties. This scheme can be enriched by inserting channels adjacent to the one under test, in order to quantify the effect of cross-talk between channels.

Subsequently, to estimate the SNR given the BER value for a given modulation format, it is determined by converting the value measured by the receiver using the corresponding B2B curve (see Fig. 3.2-b). Generally, the BER that is considered to estimate the SNR is the pre-FEC one, which expresses the degradation that the signal has undergone. This approach is based on the assumption that the NLI impairment can be modeled as AWGN, being extensively validated in various scenarios with the use of commercial network equipment [96, 97, 172]. This approach decreases its

validity when the types of fiber used have a dispersion, D, lower than 4 ps/nm/km, determining the weakening of the assumption made on the NLI. The FEC is able to completely correct errors up to a certain threshold of pre-FEC BER. Considering a context in which a certain sequence of devices, such as optical fibers, optical amplifiers, and ROADMs pass between the transmitter and the receiver, the noise accumulated determines the overall deterioration of the modulated signal given by optical propagation, which is emulated in B2B characterization with ASE noise progressive loading.

It is also important to consider other factors that affect receiver operation, estimating the penalties introduced and appropriately planning the margins [91]. The coherent receiver can fully compensate for the effect introduced by the CD and PMD up to a certain threshold declared by the vendor. Other impacting phenomena are the PDL, which can generate BER oscillations over time due to the rotation of the polarization caused by the optical fiber spans, and the aging or wear of the components, which causes irreversible alterations of the characteristics of both active and passive devices.

3.3 Cognitive Optical Line Controller

In this section, in the direction of disaggregated and cognitive optical networks, a vendor-agnostic QoT-driven optical line controller architecture capable of autonomously setting the working point of optical amplifiers to maximize the capacity of an OLS of the type described in Sect. 3.1 is presented in terms of methodology and tested on an experimental setup. Optimization problems related to the physical layer characterization and the amplifier gain control are mathematically formalized, describing all the necessary details to adopt the proposed optical line controller within a generic scenario. To define without ambiguity each optimization process, the formalism is divided into three subsections: the physical model, the optimization algorithm, and the formulation of problems. Both optimization problems, namely the characterization of the physical parameters and the definition of the working point of the amplifiers, clearly have a different formulation of the problem but adopt the same physical model and optimization algorithm.

3.3.1 Physical Model

The presented software framework uses GNPy open source Python library [96, 173] as a physical model for QoT. The emulation of the optical propagation through a single fiber span or through the complete considered OLS is performed abstracting three main object classes, where each of them is defined by a set of parameters:

1. **Optical fiber**:
    - total span length, L_S;
    - lumped losses, l, located at a specific spacial coordinate, where at least the losses due to the input, $l(0)$, and the output connector, $l(L_S)$, of the fiber span are assumed by default;
    - loss coefficient function, α, resolute in frequency;
    - Raman gain coefficient, C_R;
    - chromatic dispersion parameter, D;
    - nonlinear coefficient, γ.
2. **Optical amplifier** (EDFA):
    - gain target, $\mathrm{G_{tar}}$;
    - tilt target, $\mathrm{T_{tar}}$;
    - actual gain, G;
    - noise figure, NF;
    - saturation total output power, P^{SAT}.
3. **WDM comb**, in which each channel is described by:
    - frequency, f_i, where i is the channel ordinal number within the specified grid that goes from 1 to the number of channels, N_{ch};
    - symbol rate or baud rate, R_s;
    - roll-off, ρ;
    - signal power, P;
    - ASE noise power, P_{ASE};

- NLI noise power, P_{NLI}.

Defining a certain input WDM comb and a sequence of fibers and amplifiers, these objects allow to propagate the spectral information and to compute the WDM comb status at the corresponding output. From this it follows that the first two classes are static, where all instantiated objects do not change properties for the duration of optical propagation. The WDM comb class is dynamic, and its objects change state every time the transfer function of a certain fiber or amplifier object is applied to them. In the developed optimization framework, considering fixed in advance the properties of each fiber and amplifier in the optical propagation experienced by the defined WDM comb, the signal power, P, and the two contributions of the noise power, P_{ASE} and P_{NLI}, represent the metrics of interest. Consequently, it is possible to perform a QoT-E computing the GSNR for each declared channel in the propagating WDM comb. The main nonlinear effects considered within the calculation for the optical fiber propagation are the inter-channel SRS [99] and the NLI impairment. Regarding the optical amplifier, the amplifier object applies to the input WDM comb a resolute frequency gain profile, G, and introduces a quantity of ASE noise proportional to a flat noise figure, NF, providing a specific couple of gain target, G_{tar}, and tilt target, T_{tar}.

3.3.2 Optimization Algorithm

In the next study, each optimization problem has a remarkably high degree of computational complexity in terms of the physical model and involves a substantial number of variables. To address these challenges, a stochastic optimization algorithm based on an evolutionary strategy is adopted. Specifically, the CMA-ES [174, 139] technique is used as an optimization algorithm to determine both the characteristics of the individual fiber spans and maximize the capacity of the OLS. This selection is rooted in the fact that the physical model encapsulates nonlinear relationships that need to be solved using numerical computational techniques. Furthermore, the problem involves a substantial volume of variables and manifests itself as an irregular problem space. Consequently, opting for an algorithm that does not rely on the explicit calculation of gradients eliminates this requirement in the evaluation of the cost function. Instead, the search is based on statistical information derived from the distribution of candidate solutions. Moreover, in scenarios with more than two

variables under optimization, gauging the effectiveness of the determined solution by analyzing the problem space around the optimum becomes non-trivial and resource intensive, regardless of the chosen optimization algorithm.

3.3.3 Problem Formulation

In the following, the details regarding the mathematical formulation of two different optimization problems that address the physical layer characterization of each fiber span and the amplifier working point design are provided. First, the measurement operative steps of the monitoring devices are described in order to retrieve the required information from the in-field apparatus. Then, the optimization procedure is explained using the telemetry data.

In the preliminary, the generic OLS scheme on which the optimization methodology is applied is represented in Fig. 3.3, focusing on the integrated telemetry and monitoring equipment considered available on board each optical amplifier. As mentioned in Sect. 3.1, the OLS between two adjacent nodes of the optical network is considered a sequence of spans, N_S, ended by a single PRE, where each span is composed of a coupled amplifier–fiber. In particular, a single amplification site is equipped with an OCM and a photodiode at both terminals of the EDFA and with an OTDR. The latter performs an analysis on the fiber following the amplifier, evaluating the length, the position of lumped losses, and the loss coefficient at the frequency of the OTDR optical pulse. Regarding the measurement of the propagating spectrum, each OCM retrieves the spectral information resolute in frequency, while integrated photodiodes allow to measure the total power, minimizing the uncertainty due to eventual lumped losses.

Physical Layer Characterization

This optimization problem is conceived as an initial automatic step after the installation and the configuration of the hardware equipment and before actual transmission operations, enlarging the physical layer information and allowing to determine with higher accuracy the amplifier working point definition. From a practical point of view, this procedure can be applied in parallel to each single fiber span, speeding up the characterization process.

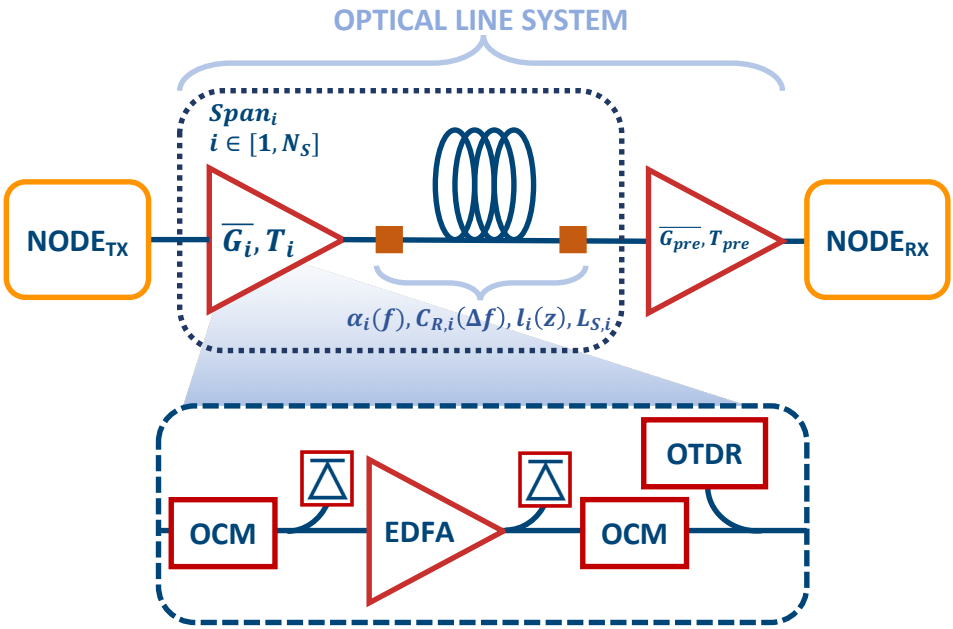

Fig. 3.3 General OLS structure under assessment focusing on the assumed available telemetry devices within a single amplification site.

Firstly, an OTDR analysis is performed for each fiber span, measuring the length of the fiber span, L_S, the positions of the eventual lumped losses in line, l, and estimating the loss coefficients at pulse frequency, $\alpha(f_{\text{OTDR}})$. Then, excluding PRE, each amplifier is set in ASE mode providing at the corresponding output a C-band ASE full spectrum. The latter is measured by OCMs at both terminals in each fiber span for two different ASE power levels, obtaining four different power profiles: $P^{\text{LOW}}(f,0)$, $P^{\text{LOW}}_{\text{tar}}(f,L_S)$, $P^{\text{HIGH}}(f,0)$, $P^{\text{HIGH}}_{\text{tar}}(f,L_S)$. The first measurement at low ASE power is performed to minimize the Raman crosstalk contribution, and the second one is done at a higher ASE power level enhancing the inter-channel SRS. The definition of the two ASE power levels is related to the installed equipment and to the telemetry sensitivity.

Once the OTDR and OCM measurements are available, the fiber span characterization is carried out for each fiber span, in order to estimate the parameters of the physical layer able to accurately emulate the experimental behavior using the physical model described above. A set of parameters for a single fiber span includes the Raman gain coefficient scaling factor (the normalized profile is assumed), K_R, the loss coefficient function, α, the input, $l(z=0)$, and the output connector, $l(z=L_S)$, and the eventual lumped losses detected by OTDR along the fiber span, $l(0<z<L_S)$.

Regarding the loss coefficient function, the phenomenological model described in Sect. 2.2.1 is used, considering all the attenuation effects involved in the propagation of optical fibers within the frequency range of interest. Because the ultraviolet absorption has constant trend within a frequency range that is far larger than the only C-band, this term is taken into account, but it is not optimized. As a consequence, Eq. 2.2 easily derives even broadband loss coefficient functions defining only four parameters: A, B, K_{IR}, A_1.

The final set of variables to optimize, x, in the defined physical layer characterization problem for a single fiber span is:

- Raman gain coefficient scaling factor, K_R;
- loss coefficient function, α, defined by four parameters: A, B, K_{IR}, A_1;
- input connector loss, $l(z=0)$;
- output connector loss, $l(z=L_S)$;
- eventual intermediate lumped losses along the fiber span, $l(0<z<L_S)$.

The objective function to minimize, F, is expressed by the following formula:

$$\begin{aligned} \mathrm{F}(x) &= \sqrt{\sum_{i=1}^{N_{\mathrm{SAMPLE}}} \left(P_{\mathrm{tar}}^{\mathrm{LOW}}(f_i,L_S) - P^{\mathrm{LOW}}(f_i,L_S)\right)^2} + \\ &+ \sqrt{\sum_{i=1}^{N_{\mathrm{SAMPLE}}} \left(P_{\mathrm{tar}}^{\mathrm{HIGH}}(f_i,L_S) - P^{\mathrm{HIGH}}(f_i,L_S)\right)^2}, \end{aligned} \tag{3.5}$$

where N_{SAMPLE} is number of frequencies sampled by the OCM, $P^{\mathrm{LOW}}(f,L_S)$ and $P^{\mathrm{HIGH}}(f,L_S)$ are the emulated power spectra at the output of the fiber span introducing for a specific set of variables, x, and $P^{\mathrm{LOW}}(f,0)$, $P^{\mathrm{HIGH}}(f,0)$, the measured power spectra, respectively. Fig. 3.4 qualitatively represents the metrics adopted for this optimization framework. The result of this methodology is more accurate in uniform fiber condition; when there are spools composing each fiber span of the same type. If this condition is not guaranteed, the optimization result provides equivalent parameters as if the specific fiber span were uniform.

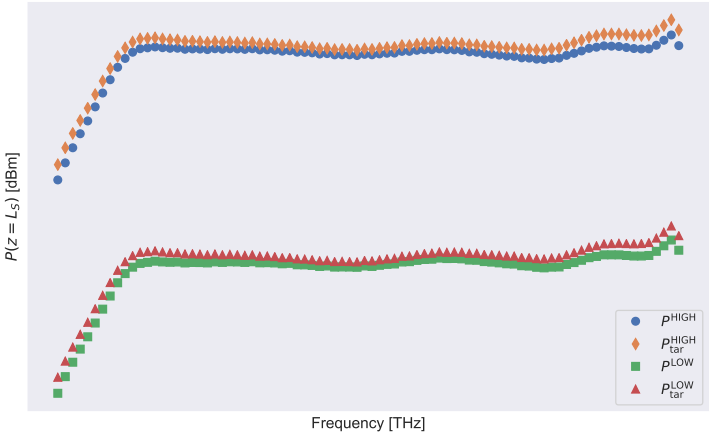

Fig. 3.4 Adopted metrics for the physical layer characterization procedure, span-by-span.

The strong point of the proposed probing and characterization procedure relies on the identification of the fiber span physical properties operating a joint optimization of the main parameters that are involved within the optical fiber propagation. In addition, this approach produces a first classification of the in-field optical fibers without having any physical layer knowledge available.

Optical Line Control

The purpose of the following framework is to define the optimal amplifier working point on the basis of QoT provided the physical layer description of the OLS previously extracted. The optical line control is addressed according to two different strategies, in which both determine the working point of each amplifier providing a gain, G_{tar}, and a tilt, T_{tar}, targets. In any case, these approaches depend on the introduced WDM comb spectrum, which has to be measured by the OCM at the OLS input to properly optimize the working point of the BST amplifier. The first optimization formulation evaluates the GSNR at the output of the OLS, having a global view of the behavior of the transmission system. The second performs a set of forward optimizations starting from the BST span, one for each span and one for the PRE alone, using at the considered span input the status of the WDM comb propagated with the optimal amplifier configurations retrieved during the previous steps. Referring to the Local-Optimization Global-Optimization (LOGO) strategy [175, 176], this second optimization is based on a similar approach, dividing a complex problem into smaller ones and evaluating the proportion between the

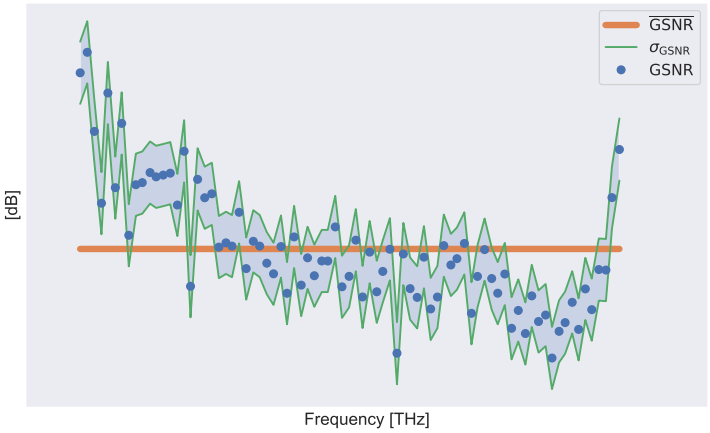

Fig. 3.5 Adopted metrics for the *global* GSNR optimization for the optical line control strategy.

two ASE and NLI noise contributions. Regarding the problem dimension, in the first case there is a single optimization which has a number of variables to optimize, which is twice the number of the OLS amplifiers. In the second case, the number of optimizations is equal to the number of OLS spans plus one related to the PRE working point, but the number of variables is fixed at two, since a single amplifier is optimized at each step.

Starting from the first optimization formulation based on the evaluation of the global GSNR, the fitness of each generated amplifier parameter configuration is evaluated in logarithmic units as follows:

$$\max_{\{\mathrm{G_{tar}},\mathrm{T_{tar}}\}} \left\{ \overline{\mathrm{GSNR}^{\mathrm{dB}}} - \sigma_{\mathrm{GSNR}^{\mathrm{dB}}} \right\}, \tag{3.6}$$

where $\overline{\mathrm{GSNR}}$ and σ_{GSNR} are the GSNR average and relative standard deviation in logarithmic units (see Fig. 3.5).

The second local optimization formulation follows for each step the metrics summarized in Fig. 3.6 and expressed in logarithmic units as:

$$\min_{\{\mathrm{G_{tar}},\mathrm{T_{tar}}\}} \left\{ |m_{P_{ch}^{\mathrm{dBm}}}| + \frac{1}{N_{ch}} \sum_{i=1}^{N_{ch}} \left| P_{\mathrm{ASE}}^{\mathrm{dBm}}(f_i) - \left[P_{\mathrm{NLI}}^{\mathrm{dBm}}(f_i) + 3 \right] \right| \right\}, \tag{3.7}$$

where $\mathrm{G_{tar}}$ and $\mathrm{T_{tar}}$ are the target parameters of the specific amplifier to optimize, P_{ASE} and P_{NLI} are the two noise contribution profiles at the output of the considered

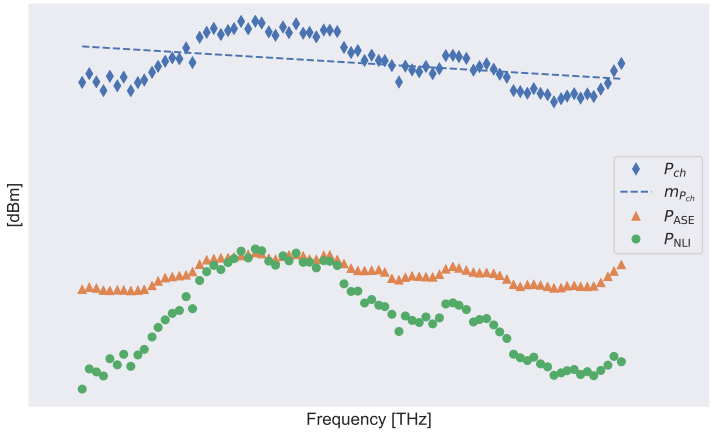

Fig. 3.6 Adopted metrics for the *local* GSNR optimization for the optical line control strategy.

span also depending on the amplifier parameters, and $m_{P_{\mathrm{SIG}}^{\mathrm{dBm}}}$ is the linear regression angular coefficient of the signal power profile expressed in dB/THz.

It is important to specify that in the evaluation of the cost function for a specific set of extracted variables the fact that an amplifier is brought to work in the saturation condition leads to the introduction of an additional cost penalty. This mechanism aims to obtain a realistic solution in which the behavior of the amplifiers within their dynamics is accurately predicted by the model.

The agnostic optimization approach confers to this control strategy the ability to uniquely determine the OLS operation without adopting power sweep procedures to establish the amplifier working point. Furthermore, the proposed methodologies are effective in the case of the full spectral load transmission condition, having minimal variations of the introduced WDM comb and avoiding the presence of transients.

3.3.4 Experimental Setup

A WDM comb composed by 80 channels centered at 193.35 THz with a WDM grid spacing of 50 GHz within the C-band is generated by manipulating an output from a ASE noise source with a commercial programmable WaveShaper© (1000S from Finisar), obtaining a final flat spectrum with an average power level of -23 dBm. 9 independent Channels Under Test (CUTs) over the 80 channels have been chosen in order to have an equally distributed sampling of the spectrum; for these CUTs, the signal transmission is managed by a commercial AS7716-24SC Cassini device, along

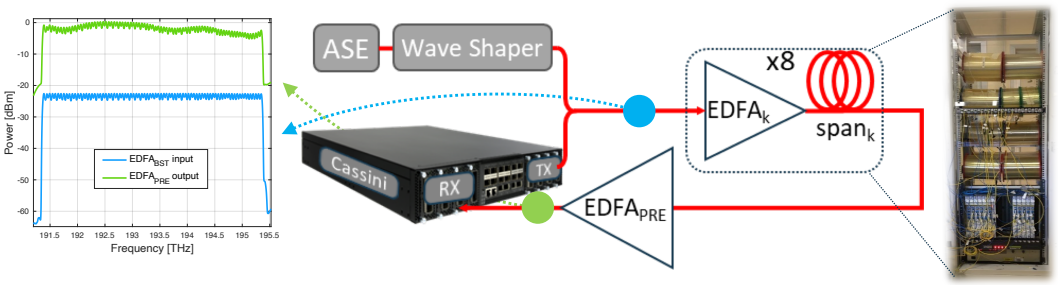

Fig. 3.7 Experimental setup and OCM measurements of the transmitted and received spectra.

with a CFP2-Digital Coherent Optics (DCO) module from Lumentum, configured in order to generate a 32 GBd, PM-Quadrature Phase Shift Keying (QPSK) modulated signal. The same module is equipped with a coherent receiver section, followed by the digital equalization and time, carrier, and phase estimation sections necessary for the signal recovery and for the pre-FEC BER evaluation. The OLS consists of 8 fibers spans, each approximately 80 km long, with a mixture of SMF types, characterized by different physical parameters and preceded by a commercial EDFA operating with different constant gain and tilt values. The complete experimental setup is depicted in Fig. 3.7.

At the OLS output, a PRE is used to fix the optical power of the channels at the receiver input and to evaluate the CUT OSNR and the power levels of all 80 channels by means of the integrated OCM; an example of the power measurement performed using the OCM is shown in Fig. 3.7. The pre-FEC BER in transmission for each CUT is then measured by means of the CFP2-DCO module. In this experimental proof of concept, the proper operation of the conceived architecture is investigated without automatizing with standard protocols the exchange of information between telemetry devices and the software controller. The acquisition and transmission of data is made using embedded laboratory protocols.

EDFA Characterization

A precise procedure has been applied to each EDFA to characterize the gain profile along the frequency produced by the specific device, given different values of the tilt and gain targets. On the contrary, a fixed value for NF has been considered for all EDFAs.

In this procedure, a fixed input spectrum, including 40 channels along the C-band, is amplified setting 15 different gain targets. For each gain target, 15 different tilt targets have been tested, in turn. All output spectra are measured with an OSA and the extracted gain profiles are evaluated. These profiles can be characterized by three features: gain average, tilt, and residual ripple profile. In particular, the tilt has been defined as the angular coefficient of the linear regression of the output spectrum profile, and, in general, it is proportional to the tilt target, as the gain average is roughly equal to the gain target.

These three characterizing quantities, along with the total saturation output power, have been measured for all EDFAs and have been used to create the software implementation that accurately reproduces these amplification procedures.

3.3.5 Results

Firstly, the physical layer characterization process is applied to the described experimental setup. The complete set of results is synthesized for each span in Tab. 3.1 and in Figs. 3.8 and 3.9. Starting from the extracted Raman gain coefficient profiles, which are strictly related to the fiber effective area, it is possible to operate a classification of the analyzed fibers even without the knowledge of the in-field type variety, deducing the corresponding value of dispersion.

Based on the OLS physical layer description reported, the optical line controller produces the configuration of the amplifier target parameters. The gain target ranges from 14.5 dB to 20.5 dB and each tilt goes from -1.5 dB to 1.5 dB, referring to the C-band in frequency ($\simeq$ 4 THz).

The dimension of the problem has a considerable impact on the optimization time. In this particular case, the single optimization with 18 variables of the *global* control strategy takes a variable time interval of some tenths of minutes. On the other hand, the total optimization time of the 9 *local* optimizations with 2 variables is less than 2 minutes. This time performance have been achieved using a processor 2.2 GHz quad-core Intel Core i7 with a 16 GB 1600 MHz DDR3 RAM.

For both global and local control strategies, the results of the optimization process of the final amplifier configurations are reported in Tabs. 3.2 and 3.3, respectively. As a preliminary experimental step, receiver site penalties have been properly characterized, making the residual impairment comparable with measurement error. Using

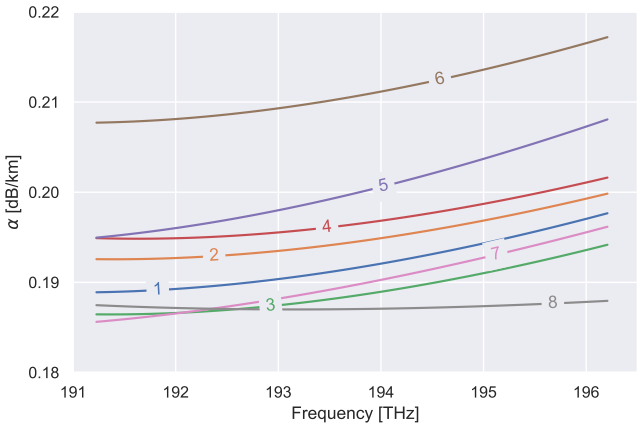

Fig. 3.8 Cognitive optical line controller: loss coefficient functions extracted during the physical layer characterization for each fiber span.

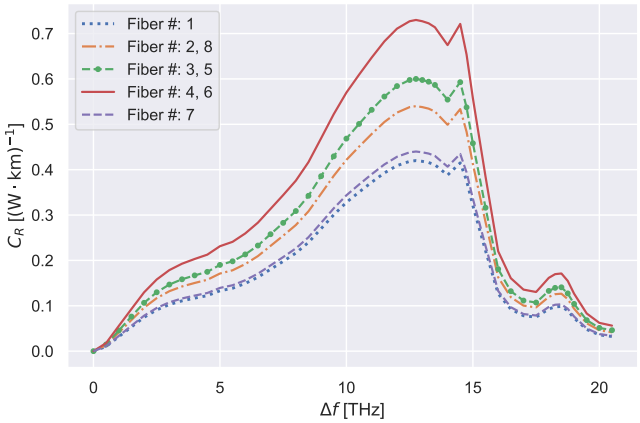

Fig. 3.9 Cognitive optical line controller: Raman gain coefficient profiles extracted during the physical layer characterization for each fiber span.

Table 3.1 Cognitive optical line controller: results of the physical layer characterization procedure performed for each fiber span.

Span	L_S [km]	K_R [(W·km)$^{-1}$]	D [ps/(nm·km)]	$\alpha(f_{\text{OTDR}})$ [dB/km]	$l(z=0)$ [dB]	$l(z=L_S)$ [dB]
#1	80.4	0.42	16.7	0.191	0.9	0.1
#2	80.4	0.54	3.8	0.194	2.0	1.0
#3	80.6	0.60	8.0	0.188	0.6	0.3
#4	79.9	0.73	4.4	0.196	0.1	3.6
#5	79.8	0.60	8.0	0.199	0.1	2.3
#6	75.8	0.73	4.4	0.210	1.7	0.4
#7	64.7	0.44	16.7	0.189	0.2	3.0
#8	78.6	0.54	3.8	0.187	0.3	0.1

Table 3.2 Cognitive optical line controller: amplifier parameter configuration optimized using the *global* control strategy.

[dB]	BST	ILA_1	ILA_2	ILA_3	ILA_4	ILA_5	ILA_6	ILA_7	PRE
G_{tar}	19.9	17.6	19.5	17.0	19.7	19.7	17.1	19.5	16.7
T_{tar}	1.5	1.5	1.4	1.4	0.3	0.4	-1.5	0.1	1.4

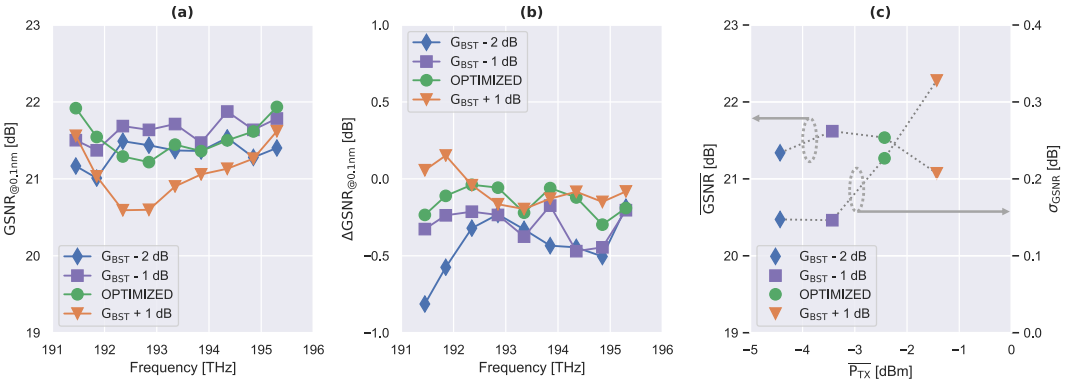

Fig. 3.10 Cognitive optical line controller: experimental results of the *global* control strategy using a noise bandwidth of 0.1 nm: (a) GSNR profiles, (b) error profiles between GNPy emulation and experimental measurement, (c) GSNR aggregated metrics versus the BST output power average level: mean and standard deviation.

Table 3.3 Cognitive optical line controller: amplifier parameter configuration optimized using the *local* control strategy.

[dB]	BST	ILA_1	ILA_2	ILA_3	ILA_4	ILA_5	ILA_6	ILA_7	PRE
G_{tar}	20.3	19.6	18.0	15.6	20.3	20.3	15.7	18.4	18.4
T_{tar}	1.1	1.5	1.5	1.5	1.5	1.5	1.5	1.5	0.8

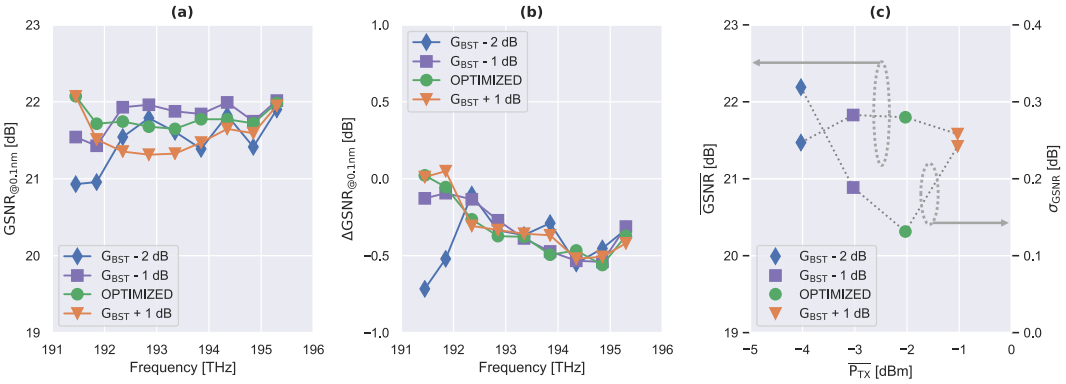

Fig. 3.11 Cognitive optical line controller: experimental results of the *local* control strategy using a noise bandwidth of 0.1 nm: (a) GSNR profiles, (b) error profiles between GNPy emulation and experimental measurement, (c) GSNR aggregated metrics versus the BST output power average level: mean and standard deviation.

optimized amplifier parameter configurations, four different experiments are carried out for each control strategy modifying the BST gain from -2 dB to +1 dB with steps of 1 dB. This experimental campaign aims to demonstrate that the optimal working points evaluated are actually close to the optimum, comparing the GSNR profiles collected during this power sweep.

The two sets of experiments for both control strategies are summarized in Figs. 3.10 and 3.11. Observing the GSNR error profiles in Figs. 3.10(b) and 3.11(b), it is remarkable that, in view of the characterization of the operated physical layer, GNPy accurately estimates the GSNR profile for all amplifier configurations of both power sweeps. In fact, the emulations are conservative in almost all cases with a maximum error that is strictly below 0.9 dB. Considering the aggregated metrics, the optimized amplifier configuration derived from the global approach shows suboptimal characteristics due to a smaller average GSNR, 21.6 dB, and a more dispersed profile, 0.22 dB of standard deviation, with respect to the same configuration with a BST gain set at 18.9 dB. On the other hand, the local control configuration has the lowest standard deviation, 0.13 dB, and a average GSNR that is almost equal to the maximum achieved in the power sweep and higher than that of the global control strategy, 21.9 dB. In both cases, the performance of the experimental results achieved is excellent in terms of GSNR profile flatness, bringing the system close to the actual global optimum. When comparing the two control strategies, the local approach is more effective in tackling the final goal, achieving a GSNR profile with a higher mean and a more distributed shape. It takes noticeably a small amount of time to complete the optimization process, due to the formulation of modular problems with a higher number of optimizations but with a small number of variables to optimize. In addition, this framework allows for the accurate determination of the dependency between the GSNR profile with respect to the amplifier configuration owing to the forward local approach, span-by-span.

3.4 Iterative Supervised-Learning Optimization

As a variation and enhancement of the previous section, in the following, a methodology is presented that optimizes QoT of an OLS by setting the working points of EDFAs, by analyzing simulations that use synthetic data derived from experimental characterization of commercial devices. It is a procedure divided into three phases:

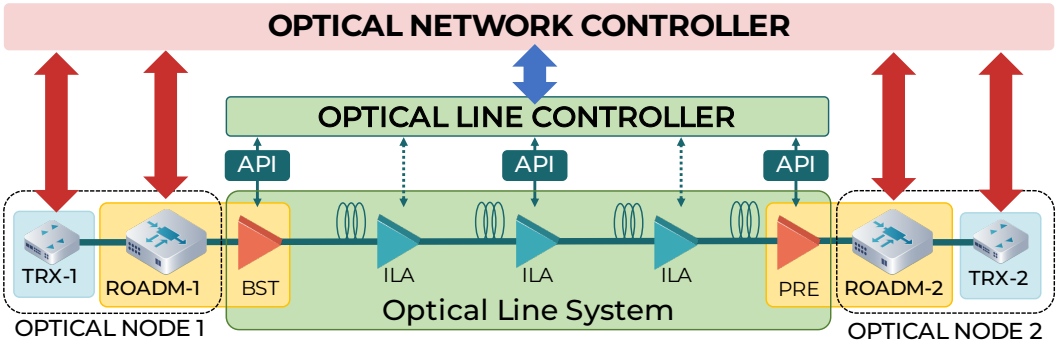

Fig. 3.12 ROADM-to-ROADM optical line system architecture with auxiliary TRXs as telemetry devices.

- amplifier physical layer characterization;
- configuration design;
- iterative supervised learning approach.

Within the first phase, a novel characterization of the physical layer of the amplifier is proposed, using a simple EDFA model that allows an efficient estimation of OLS behavior, knowing only the operating ranges of the devices. The results show that the satisfactory outcome already produced during the design phase is further improved by the iterative supervised learning approach.

The latter is implemented for single OLSs between couples of adjacent ROADMs, each equipped with a certain set of auxiliary TRXs, allowing QoT estimation of the specific OLS in different portions of the propagating WDM spectrum by means of the BER measurement for a given amplifier configuration (see Fig. 3.12). This assumption reflects the reality in the case of linear topology optical networks or in which there is the need to route connections between adjacent nodes. Regarding the telemetry required for the proposed implementation, each amplification site is equipped with an OTDR and a couple of OCMs at the input and the output of the device. The proposed iterative supervised learning approach is shown to achieve considerable improvements with a significantly limited number of training data samples (i.e., only a few cases of actual performance of QoT using 4 selected frequencies of the spectrum WDM for the auxiliary TRXs) compared to the solution found applying only the configuration design procedure.

The simulation results obtained through the iterative supervised learning approach in the highly controlled environment developed are referred to a mitigation of QoT limited to the effect of the EDFAs' gain ripple and ASE noise. It is expected that the application of this methodology to a real case will have a much greater impact on performance improvement due to deviations from the model of other components that directly affect QoT, such as fiber spans, ROADMs and TRXs. In addition, the proposed methodology allows efficient dealing with optimization of an OLS even after a fiber cut or component aging. The latter results from a combination of environmental factors and operational usage during the life cycle of the optical infrastructure. The aging phenomenon includes mechanisms such as reduced output power from light sources, reduced sensitivity of photodiodes, attenuation of optical fibers, thermal and mechanical stresses, and cumulative effects resulting from exposure to high power. An optical control of the proposed type could efficiently handle QoT and also mitigate the impact of aging.

For completeness of the description, due to the complexity of the problem, the optimization algorithm adopted within all the steps of the procedure is CMA-ES [139], a stochastic optimization algorithm based on an evolutionary strategy. Regarding the adopted physical layer model, in the built software framework, the GNPy open source Python library [96] is used to emulate optical propagation using the physical layer models of two main class of objects: the optical fiber and the propagating WDM comb.

3.4.1 Methodology

The proposed methodology aims to optimize the working points of an OLS maximizing and leveling the QoT for all modulated channels that make up the WDM comb. Within an optical network, this approach provides the same performance for any traffic connection allocated between a couple of source/destination nodes of the optical infrastructure passing through the specific OLS. This procedure involves the use of a set of TRXs, transmitting as many channels equally spaced in frequency, properly characterized in the B2B configuration to retrieve the SNR estimation based on the measured BER (see Sect. 3.2.3). In the following, the GSNR derived from the measured field BER is referred to this conversion using the B2B TRX characterization of all these CUTs. The remaining part of the WDM comb is considered to

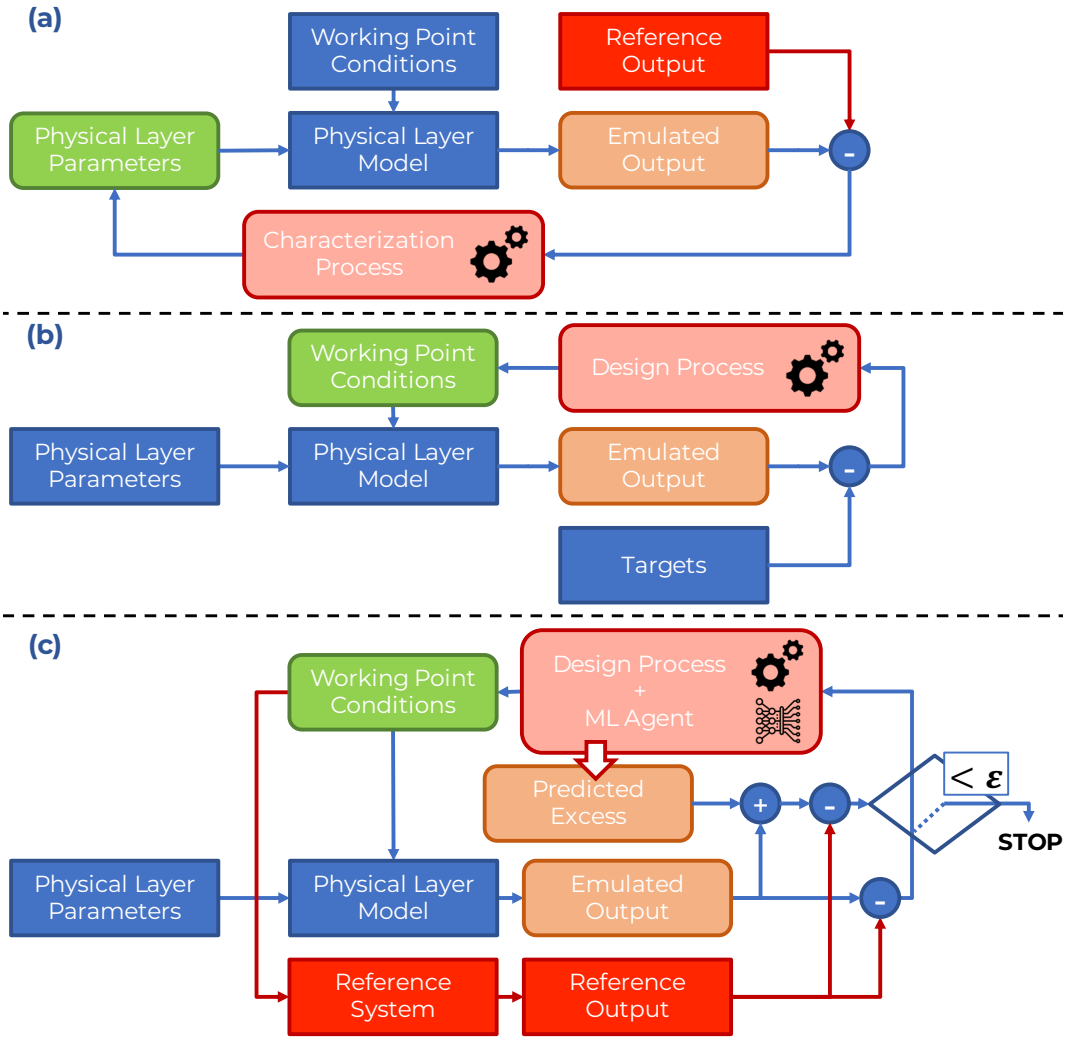

Fig. 3.13 Methodology conceptual block schemes: (a) physical layer characterization (related to fiber spans and optical amplifiers), (b) configuration design optimization relying on the retrieved physical layer model, (c) working point refinement using an iterative supervised learning approach.

be filled with ASE-shaped channels to reproduce the full spectral load transmission condition.

In addition, the adopted terminology is based on the use of three key words. The word *model* refers to the physical layer model built while performing the proposed methodology, which emulates the behavior of a given system. Then, the word *reference* means the system against which the model is compared. It can be a real system when referring to an experiment or a virtual object in a simulation. Finally, the word *prediction* concerns the result obtained by the ML agent's formulation in the third step of the methodology.

The algorithmic process that brings the OLS to be operative is divided into three phases, which will be described in detail in the following. The block diagrams of each of them are depicted in Fig. 3.13. In the first step, generally called *physical layer characterization*, the field telemetry apparatus is used to probe the status of the system in a specific working condition, and the measurements are processed to retrieve the equivalent physical layer model parameters of the device under test. In the following, only the novel EDFA physical layer characterization is presented, assuming that the fiber characterization, which is independent from the installed EDFA characteristics, is performed as a preliminary step [143]. This procedure brings to the full virtualization of each fiber span of an OLS, providing the estimation of the fiber length, L_S, the loss coefficient function, α, the Raman gain coefficient curve, C_R, and the lumped losses, l.

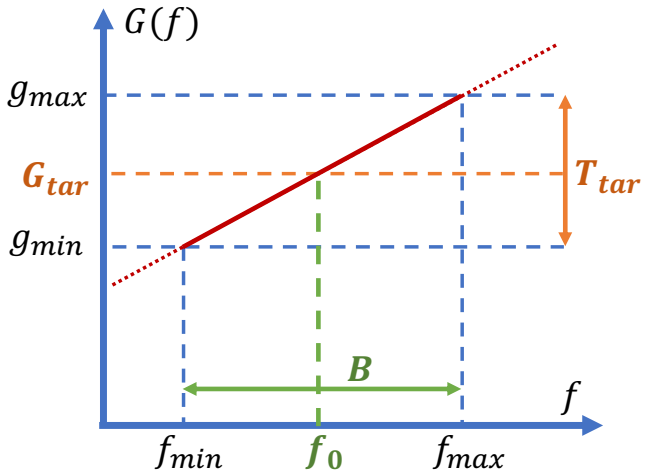

Fig. 3.14 Qualitative representation of the EDFA simple model gain profile.

EDFA Physical Layer Characterization

A simple physical layer EDFA model is considered, describing the gain profile, G, in logarithmic units as:

$$G(f) = \mathrm{G_{tar}} + \frac{\mathrm{T_{tar}}}{B}(f - f_0) \ , \tag{3.8}$$

where all the parameters are graphically represented in Fig. 3.14, and the introduced ASE noise profile, P_{ASE}, in linear units as:

$$P_{\mathrm{ASE}}(f) = hf\,\mathrm{NF}\,[G(f) - 1]\,B_n \ , \tag{3.9}$$

where h is the Planck constant, B_n is the noise bandwidth and NF is the noise figure, constant and fixed for all the gain values. The amplifier settings coincide with the target parameters, $\mathrm{G_{tar}}$ and $\mathrm{T_{tar}}$, while B, f_0 and NF represent the physical layer parameters of the EDFA to be probed. In particular, B and f_0 parameters define the slope of the tilt and where it is applied within the amplification band. The NF parameter is used to extract the average level of ASE noise introduced by EDFAs in a specific working condition.

All EDFAs within the OLS are set in a known working condition. Using the telemetry, it is assumed that the system is set in transparency mode, choosing the gain value to restore the required output power and the tilt values to balance the flatness of the channel power profile. With this configuration, the input spectrum propagates through the reference OLS, collecting at the output GSNR for the complete set of available TRXs, GSNR^r.

The characterization process aims to jointly retrieve the three EDFA model physical layer parameters for all the EDFAs within the OLS model observing the emulated, GSNR^e, and the reference, GSNR^r, GSNR profiles under the defined working conditions, as stated by the following objective function:

$$\min_{\{B,\,f_0,\,\mathrm{NF}\}} \left\{\mathrm{RMSE}\left(\mathrm{GSNR}^e(f), \mathrm{GSNR}^r(f)\right)\right\} \ , \tag{3.10}$$

where f are referred to the frequencies of the CUTs. The optimization problem presents a dimension of $3 \times \mathrm{N_{EDFA}}$, where $\mathrm{N_{EDFA}}$ is the number of EDFAs present in the OLS.

The main advantage of this novel EDFA characterization process is that it fully abstracts the OLS only knowing the operating ranges of the setting, without performing any experimental characterization in-laboratory for these lumped components.

Configuration Design

At this point, the OLS full abstraction has been achieved, obtaining an equivalent representation of all fibers and EDFAs. On the basis of the previous characterization, the abstracted OLS can be exploited in order to optimize the EDFAs' working point by fixing the retrieved physical layer parameters and modifying the amplifiers' settings within the optimization process (Fig. 3.13-b).

Using the precision of the characterization performed, the design process manipulates the OLS model to determine which amplifier configuration produces the highest and most homogeneous QoT at the output [140]. Assuming two target parameters for a single EDFA (e.g. G_{tar}, T_{tar}), the dimension of the problem amounts to $2 \times N_{EDFA}$. The objective function adopted to achieve this purpose is Eq. 3.6. This problem formulation addresses the choice of the amplifier working point observing the overall QoT estimated at the line output, with the aim of achieving the maximum average value for all channels that make up the spectrum with the minimum dispersion of the profile.

Iterative Supervised Learning Refinement

The result achieved following the procedure until this point could be sufficient to make the OLS ready to start standard transmission operations. Ignoring the uncertainties related to the knowledge of the physical model of the fibers, the TRXs and the ROADMs penalties, the relevant aspect of the adopted EDFA model is that it does not consider any ripple in the gain and ASE noise profile and any dependency of the noise figure with respect to the set gain. In order to properly mitigate the EDFA gain and noise ripple inaccuracies, the methodology ends with a refinement phase of the EDFAs' working point using an iterative supervised learning approach (Fig. 3.13-c, Alg. 3). The Maximum Absolute Error (MAE) evaluation is performed using the following definition:

$$\mathrm{MAE}(X^p, X) = \max\left(|X_i^p - X_i^m|\right) \quad \forall\, 1 \leq i \leq N\,. \tag{3.11}$$

where X^p and X are the arbitrary profiles of the predicted profile and the measured or reference profiles, respectively, and N is the total number of samples per profile.

Algorithm 3 Amplifier working point refinement using the iterative supervised learning approach (pseudo-code)

```
procedure
    Retrieving GSNR^r(f)
    Evaluating MAE(GSNR^p(f), GSNR^r(f))
    if MAE(GSNR^p(f), GSNR^r(f)) > ε then
        Dataset initialization
        while MAE(GSNR^p(f), GSNR^r(f)) > ε do
            ML agent training
            Design process including the ML agent
            Retrieving GSNR^r(f)
            Evaluating MAE(GSNR^p(f), GSNR^r(f))
            Evaluating a new sample: GSNR^e(f) − GSNR^r(f)
            Dataset update
        end while
    end if
end procedure
```

A ML agent is created that maps the difference between the emulated and reference output GSNR profiles, ΔGSNR, according to the corresponding complete EDFA configuration by means of a neural network. An initial dataset is collected both by emulating the behavior of the system through the OLS model and by obtaining the reference GSNR profile using configurations similar to the optimal working point defined in the previous step. The design framework is integrated with a single additional Artificial Neural Network (ANN) and inserted within a larger loop in which the problem dimension and the objective function remain unvarried, but the evaluated GSNR profile is expressed as:

$$\mathrm{GSNR}^p(f) = \mathrm{GSNR}^e(f) + \Delta\mathrm{GSNR}(f)\,, \tag{3.12}$$

where GSNR^p is the overall predicted GSNR profile, GSNR^e is the GSNR profile emulated by the model and ΔGSNR is the GSNR excess predicted by the ANN for each CUTs. At each iteration, the ANN of the ML agent is trained using the current dataset, the OLS is set according to the actual optimal configuration and the dataset is updated by adding the residue between the emulated and reference GSNR profiles. The refinement loop ends when the difference between the predicted and reference

GSNR profiles is below a given tolerance, ε:

$$\mathrm{MAE}(\mathrm{GSNR}^p(f), \mathrm{GSNR}^r(f)) < \varepsilon \,. \tag{3.13}$$

3.4.2 EDFA Machine-Learning Model

An EDFA realistic model both in terms of gain profile and ASE noise generation has been made by means of a ML technique to define the reference OLS of the simulation framework. In particular, a dataset has been collected to perform a full spectral load characterization of a commercial EDFA with maximum output power of 20 dBm and maximum gain of 20 dB. Much valuable research has been done on EDFA modeling using ML techniques [177, 155, 178]. The ML model is adapted to be complementary with respect to the EDFA simple model proposed in the physical layer characterization.

The experimental setup is depicted in Fig. 3.15. A commercial wave shaper filter (1000S from Finisar) is programmed to shape the output of an ASE noise source that generates a C-band WDM comb centered at 193.5 THz and composed by 38 channels, 100-GHz spaced, with 32 GHz of bandwidth each. The WDM comb is introduced

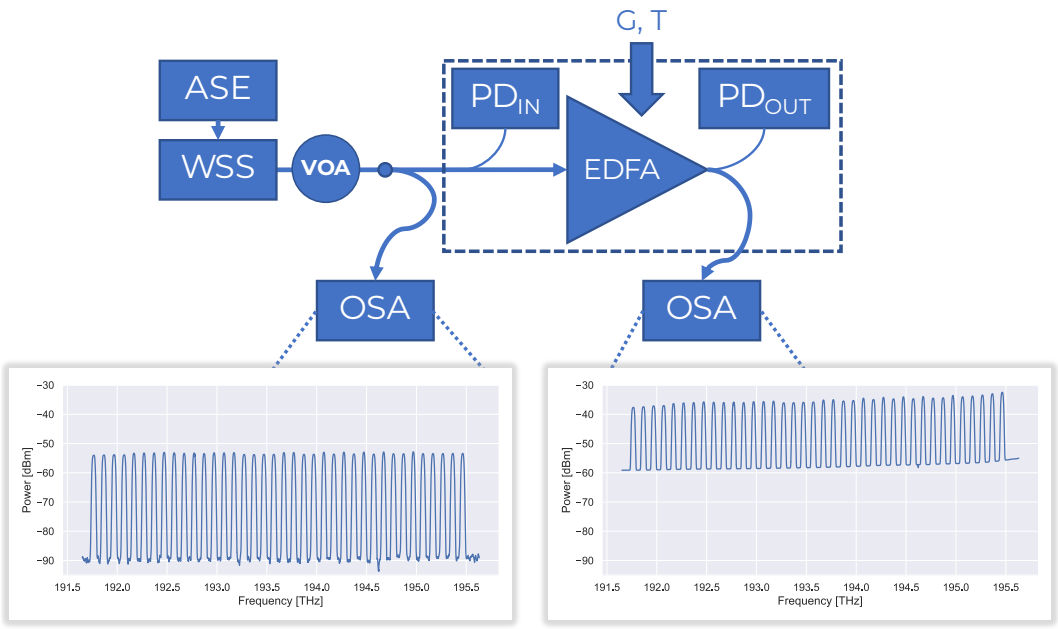

Fig. 3.15 Experimental setup sketch for the characterization a commercial EDFA and measurement examples.

at the EDFA under test input with 9 different overall power values, ranging from -10 up to 6 dBm. Working in fixed gain mode, the EDFA under test is set under different conditions; the gain target parameter, G_{tar}, ranges from 14 to 20 dB (1 dB step), whereas the tilt target parameter, T_{tar}, (gain difference between the extreme channels) ranges from -5 to $+5$ dB (1 dB step). For each combination of input power, EDFA gain and tilt target values, the WDM comb spectrum is captured both at the input and output of EDFAs by means of an OSA and integrated photodiodes. The OSA resolution bandwidth was set to 10 GHz in order to appreciate both the signal peaks and the noise level. All measurements performed with the EDFA in saturation condition are removed from the dataset as they introduce an ambiguity in the relation between target parameters and actual EDFA output. Moreover, knowing the specifications of the in-field amplifiers, the saturation condition is generally avoided in real-case scenarios with the design phase.

Gain profiles, G, are evaluated from the difference between the input and output power peak profiles. Thanks to the internal feedback mechanism of the amplifier, the gain target parameter corresponds exactly to the difference between the total input and output power values measured by the integrated photodiodes. The gain ripple profile, ΔG, predicted by the ML model is defined in logarithmic units as:

$$\Delta G(f) = G(f) - \left[G_{tar} + \frac{T_{tar}}{B}(f - f_0) \right] , \tag{3.14}$$

where B and f_0 are the band on which the tilt is applied and the pivot frequency of the gain profile, respectively, expressed in Hz. These two parameters are fitted in advance, minimizing the RMSE between all the measured gain profiles and the profiles obtained using this linear expression properly considering the corresponding combination of target parameters:

$$\mathrm{RMSE}\,(X^p, X) = \sqrt{\frac{\sum_{i=0}^{N} \left(X_i^p - X_i\right)^2}{N}} . \tag{3.15}$$

For each amplifier configuration, the evaluated ASE PSD profile is reported at the amplifier input subtracting the corresponding evaluated gain profile in logarithmic units. Then the residual noise of the input source is removed from the profile by taking the difference between the two quantities in linear units [154]. The ASE PSD

ripple is evaluated in logarithmic units as:

$$\Delta \mathrm{PSD}_{\mathrm{ASE}}(f) = \mathrm{PSD}_{\mathrm{ASE}}(f) - \overline{\mathrm{PSD}_{\mathrm{ASE}}}\,, \tag{3.16}$$

where $\overline{\mathrm{PSD}_{\mathrm{ASE}}}$ is the profile average, which is stored in a table according to the corresponding amplifier configuration and used in order to perform the overall prediction within amplifier EDFA model.

Based on the described dataset, the ML technique exploits two different ANNs, to predict the ripples of both the gain and the ASE PSD profiles, respectively. To determine the appropriate configurations of the ANN model in order to minimize the complexity, extensive simulations have been performed by changing the ANN parameters, such as number of layers, neurons, epochs, batch size, and types of activation function. Each ANN is implemented using the open source TensorFlow© library [179], which consists of an input layer, a hidden layer with 256 neurons, and one output layer. Furthermore: a Rectified Linear activation Unit (Adam)-based activation function is used for all neurons to avoid the vanishing gradient problem and the Adaptive Moment Estimation (Adam) optimizer and the RMSE metric are used to optimize and evaluate the model, which is trained on 5000 epochs with

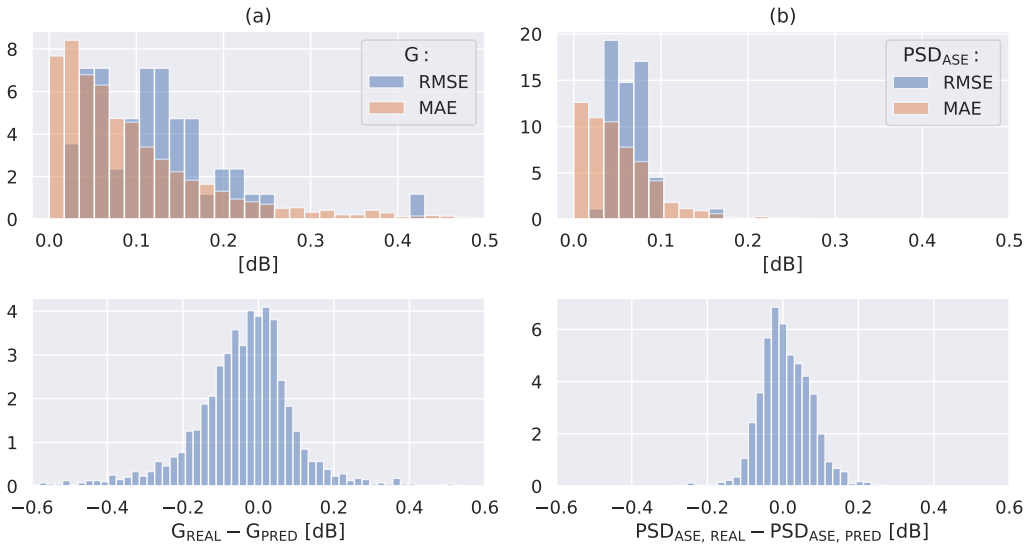

Fig. 3.16 EDFA ML model testing results: RMSE and MAE distributions, and error distribution between the measured profile and the predicted profile for the gain (a-column) and the ASE PSD (b-column).

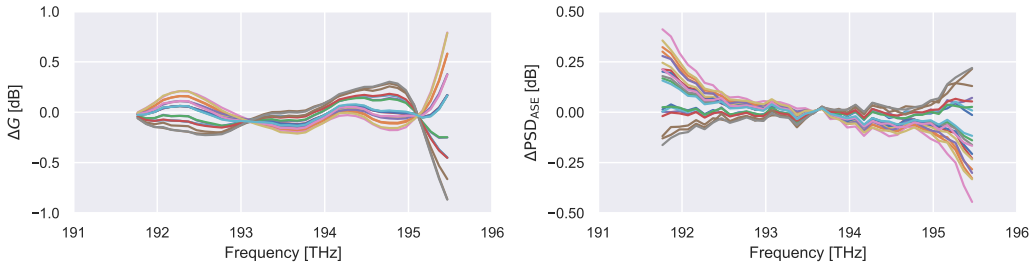

Fig. 3.17 Examples of $\Delta G(f)$ and $\Delta\text{PSD}_{\text{ASE}}(f)$ profiles produced by the ML EDFA model, fixing the total input power at -4.0 dBm and randomizing the values of gain and tilt with the corresponding operative ranges.

a batch size of 64. The input feature space for both the gain and the ASE PSD ripple estimation includes the amplifier target parameters and the total input and output powers. For a given pattern of features, the predicted label values of the two ripple profiles are related to 38 C-band frequencies fixed in the experimental setup. Then, the two predicted ripple profiles are linearly interpolated over the propagated spectrum frequencies. Moreover, the ASE PSD average is linearly interpolated according to the amplifier settings.

For both the ripples, the dataset consists in 510 samples and the model is validated by splitting it into a proportion 90-10% for training and testing, respectively. The goodness of the prediction is estimated in terms of RMSE, MAE and error considering the test dataset over the entire spectrum of each sample (Fig. 3.16). Observing the statistics related to the prediction of the gain ripple, the average value for both the RMSE and the MAE is below 0.2 dB. The maximum error values are 1.4 dB and -0.9 dB, both recorded in rarely used amplifier configurations in which the tilt orientation increases the interchannel SRS. Similarly, considering ASE PSD ripple predictions, the average value for both the RMSE and the MAE is below 0.1 dB. For both the gain and the ASE PSD ripple profiles, the error distributions are concentrated into a dense zone of values around the zero mean. Some examples of the ripples produced by the ML EDFA model are shown in Fig. 3.17.

3.4.3 Simulation Framework

To test the proposed methodology, a reference OLS is created using the EDFA ML model produced from the experimental characterization described previously

in a commercial EDFA (Sect. 3.4.2) and a set of 6 SSMFs characterized after the characterization of the physical layer described in [143], which comprises a span of 6 EDFA-fiber with a nominal length of 65 km and an additional EDFA at the end as PRE. Each fiber span presents a loss coefficient function that varies the frequency around 0.19 dB/km, a Raman gain coefficient scaling factor that ranges from 0.38 to 0.44 1/W/km, input and output connector losses ranging from 0.1 to 2.5 dB and the total span loss is varied from 14 to 22 dB. The dispersion parameter, D, is assumed to be 16.7 ps/nm/km for all the fibers. The reference OLS represents in simulation what the behavior of a real system would be, and it shares with the OLS model built following the proposed methodology the same fiber physical layer abstractions, but differs for the adopted EDFA model. In fact, as described in Sect. 3.4.1, the OLS model is based on the use of the EDFA simple model. In this simulation analysis, the mitigation of QoT produced by the iterative supervised learning approach is limited to the effects of the EDFAs' gain ripple and ASE noise.

Regarding the EDFA physical layer characterization, the bounds for the band, the central frequency, and the noise figure are 3.5–5.5 THz, 192–194 THz and 4.2–6 dB, respectively. The OLS is set in transparency mode at a total power level of 19 dBm. The result of the characterization process is reported in Tab 3.4. Based on the models produced, the working point of EDFAs has been optimized in the design phase, placing as bounds for the gain and tilt parameters the ranges 12–20 dB and -5–+5 dB, respectively.

The transmission scenario has been set as a fully loaded spectrum composed of 70 channels at 32 GBd and 50 GHz fixed spacing centered on the C band, with an equalized uniform power at the input of the BST (0.1 dBm total power). The optimization target has been defined as the maximum average GSNR over all channels, achievable with a limited GSNR variation of each channel in order to obtain a minimal QoT complexity (see Eq. 3.6).

The refinement process starts with the initial dataset creation consisting of 5 samples. The latter are obtained through the evaluation of amplifier configurations similar to the optimal one, randomizing each parameter in the range ± 0.5 dB. The initial size of the dataset has been voluntarily fixed at a small value to stress the convergence of the process. The proposed iterative supervised learning approach is based on the use of a dedicated ANN that has the amplifier gain and tilt target parameters as features and the residual GSNR between the reference and the em-

Table 3.4 Iterative supervised-learning optimization: results of the EDFA physical layer characterization, and the design and refinement optimizations.

	Characterization			Design		Refinement	
	B [THz]	f_0 [THz]	NF [dB]	G_{tar} [dB]	T_{tar} [dB]	G_{tar} [dB]	T_{tar} [dB]
BST	5.49	193.52	4.2	16.2	-0.1	17.4	-3.7
ILA 1	3.50	193.45	4.2	14.6	-0.4	13.3	-2.6
ILA 2	3.50	193.82	4.2	14.2	-2.9	16.0	-0.6
ILA 3	3.68	193.30	4.2	16.2	-1.8	15.0	-0.2
ILA 4	5.49	193.86	4.2	15.5	1.8	16.3	-0.2
ILA 5	5.49	192.08	4.2	17.4	2.8	16.0	0.8
PRE	4.72	192.17	4.3	12.1	-2.3	17.6	0.9

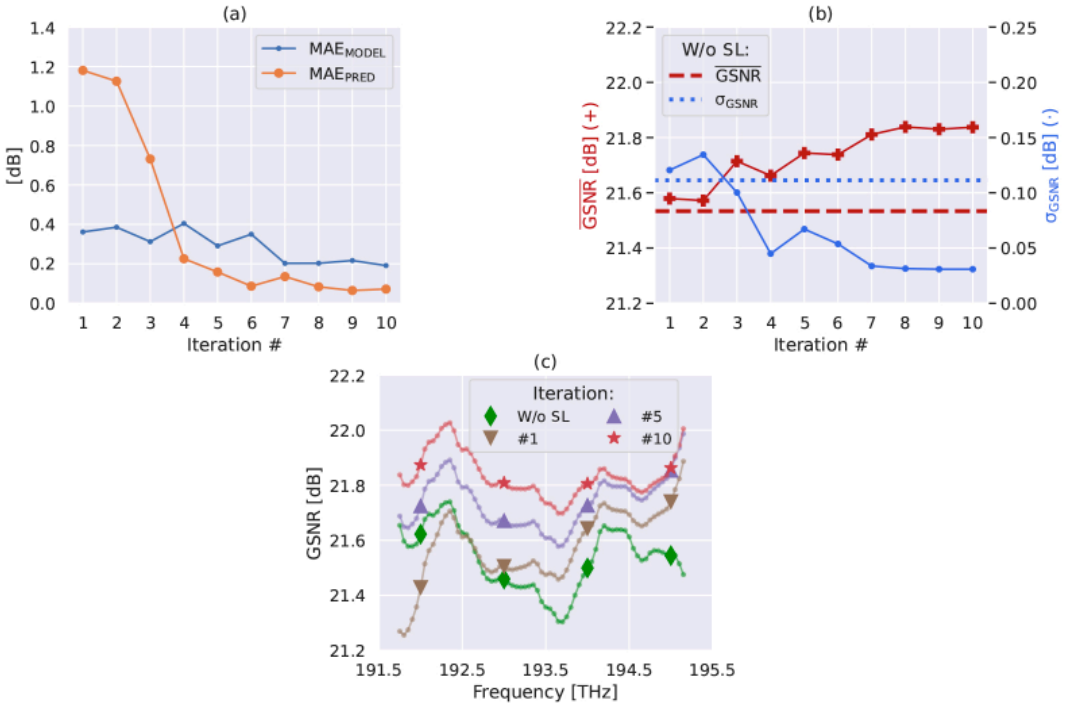

Fig. 3.18 Iterative supervised-learning optimization: simulation results using the refinement with the iterative supervised-learning (SL) approach: (a) MAE evolution comparison between the GSNR profiles obtained with the physical layer model only and the combination of the model with the ANN prediction, (b) GSNR aggregated metrics evolution, mean and standard deviation, (c) GSNR profiles at a specified iteration produced with the reference OLS.

ulated GSNR, ΔGSNR, as labels. The ANN comprises a single hidden layer with 256 number of neurons (ReLU activation function). An optimization strategy based on Adam is used to update the weights with a batch size of 64.

3.4.4 Results

Fixing the tolerance $\varepsilon = 0.1$ dB, the refinement process ends after 10 iterations, having the consecutive last 3 iterations below the tolerance. The results, including the comparison with the design outcome, are graphically reported in Fig. 3.18. The final amplifier working point configuration of both processes is reported in Tab. 3.4. After the fourth iteration, the ML agent enables the outperformance of the accuracy prediction obtained with the only OLS model (Fig. 3.18-a). It is remarkable how the latter provides an estimation accuracy below 0.5 dB, proving the goodness of the EDFA characterization. The aggregated metrics of the GSNR average and standard deviation reported in Fig. 3.18-b show the clear improvement trend, refining the mean of 0.3 dB and bringing the standard deviation from 0.11 dB to 0.03 dB. The performance difference between the configurations obtained through the design process and the refinement is represented in Fig. 3.18-c in terms of GSNR profile, showing how the reference OLS improves the QoT of all CUTs.

3.5 Assessment on Local vs. Global Optimization Strategies

In this section, different optimization strategies based on Eqs. 3.6 and 3.7 are investigated in an accurate and controlled simulation environment using a ML EDFA model (see Sect. 3.4.2) derived from an experimental dataset on commercial devices and a characterized set of fiber spans, enlarging the collection of proposed methodologies in Sect. 3.3 and providing directions on their utilization. In particular, the two mentioned objective functions are combined with different observations of the metrics of interest both at the end of the line and, progressively and in turn, at the end of a single span, comparing the obtained results and analyzing the overall behavior.

3.5.1 Problem Formulation

The analysis performed in this work focuses on the formulation of four different optimization problems, defining the operative points of the EDFA collection, $\{G_{tar}, T_{tar}\}$, according to two objective functions. The first one, labeled as *GSNR* objective function, evaluates the GSNR profile with the aim of maximize its average, $\overline{\text{GSNR}}$, and minimize the standard deviation, σ_{GSNR} (see Eq. 3.6). The second expression, named *NOISE* objective function, which is based on a methodology similar to the LOGO technique, assesses the relative impact of the ASE and NLI power profiles, P_{ASE}, P_{NLI} (see Eq. 3.7)

The two mentioned objective functions are combined with two different observation strategies. The first one consists in the evaluation of the specific objective function at the end of the line (*global* approach) formulating an optimization problem with a total number of variables to optimize equal to twice the number of optical amplifiers within the OLS, where 2 represents the number of parameters that define each amplifier's operating point, gain and tilt targets. On the contrary, the second one starts with the BST span and executes a series of forward optimizations, one for each span and one for the PRE alone, using as the input for the span that being evaluated the state of the WDM comb propagated with the optimized amplifier configurations collected in the earlier phases (*local* approach). This formulation provides for the division of the problem into many optimizations equal to the number of amplifiers present within the OLS, each with a fixed number of variables to be optimized equal to 2.

In summary, the four optimization strategies outlined by combining the two objective functions and the two evaluation approaches are:

- GLOBAL GSNR;
- GLOBAL NOISE;
- LOCAL GSNR;
- LOCAL NOISE.

Table 3.5 Assessment on local vs. global optimization strategies: fiber physical layer parameters.

#	L_S [dB/km]	K_R $[(\mathrm{W}\cdot\mathrm{km})^{-1}]$	$l(z=0)$ [km]	$l(z=L_S)$ [km]
1	106.179	0.34	3.60	0.24
2	107.501	0.44	1.25	0.71
3	106.179	0.44	1.54	0.12
4	108.825	0.42	0.60	0.11
5	108.278	0.42	0.18	0.12
6	106.195	0.42	1.11	0.22
7	106.791	0.34	0.10	0.12
8	106.424	0.34	0.16	0.71
9	107.273	0.42	0.21	0.13
10	108.319	0.42	0.52	2.31

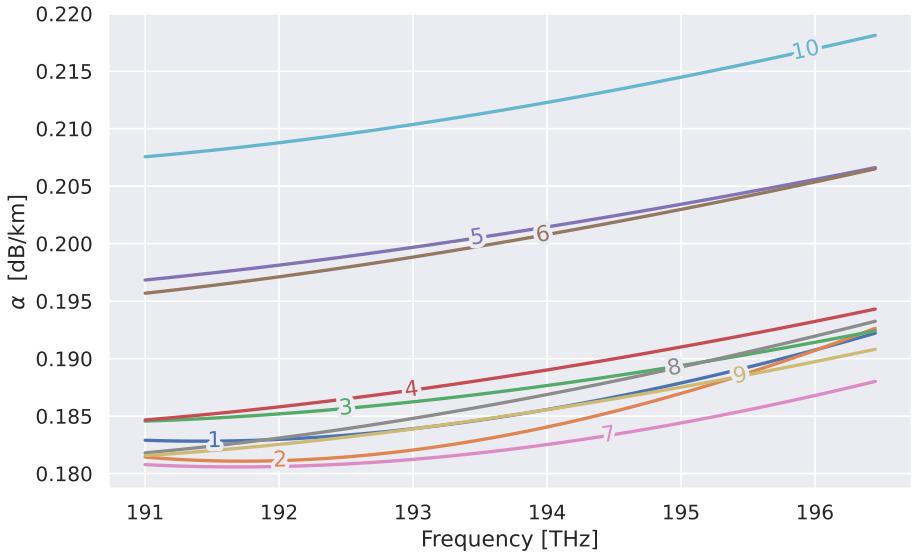

Fig. 3.19 Assessment on local vs. global optimization strategies: loss coefficient functions of each fiber span.

3.5.2 Simulation Framework

Recalling the optical network architecture defined in the previous section, the four formulated optimization problems are tackled using a simulation framework consisting of an OLS of 10 fiber spans (11 amplifiers and 10 fiber spools). The considered full C-band WDM spectrum starts from a channel with a central frequency of 191.31 THz and it is composed of 64 channels with 64 GBd of symbol rate, 75 GHz of spacing and 0.15% of roll-off, presenting a flat signal profile with a total power of 0 dBm at the input of the BST.

The physical model of the fiber is taken from the open source Python library GNPy [96], while the EDFA model is based on the ML technique presented in Sect. 3.4.2. Fiber objects are described through a set of physical layer parameters characterized from an experimental laboratory setup composed of 10 SSMF spans and reported in Fig. 3.19 and Tab. 3.5, where L_S is the fiber span length, C_R is the Raman gain coefficient scaling factor, $l(z=0)$ is the loss of the input connector and $l(z=L_S)$ is the loss of the output connector. The values of the dispersion parameter and the non-linear coefficient are fixed for all the fibers at 17.7 $\text{ps}^2\cdot\text{km}^{-1}$ and 1.27 $\text{W}^{-1}\cdot\text{km}^{-1}$, respectively. The NLI impairment is computed considering 7 CUTs equally distributed along the C-band and linearly interpolating between them and using the GGN model approximation described in [161]. The ML EDFA model is obtained characterizing in full spectral load conditions the gain and the introduced ASE noise profiles of a commercial device with a maximum output power of 23 dBm, gain operative range from 12 to 27 dB and tilt operative range from -5 to 5 dB, and it is used for all the OLS amplifiers. On the basis of the created dataset, two neural networks are generated, one for the gain and one for the introduced ASE noise, respectively, which predict a profile having as input parameters the total input power, the gain, and the tilt target. Starting from the channels defined in the measurements, the profiles are adapted to the channels used in the simulation by linearly interpolating in logarithmic units of measure.

A stochastic optimization method based on an evolutionary approach called CMA-ES [139] is used, since each optimization problem provides a high computational cost from the perspective of the physical model and a large number of variables. In each optimization, the steps leading to the evaluation of a single function are first the propagation of the defined WDM spectrum through the OLS using the current

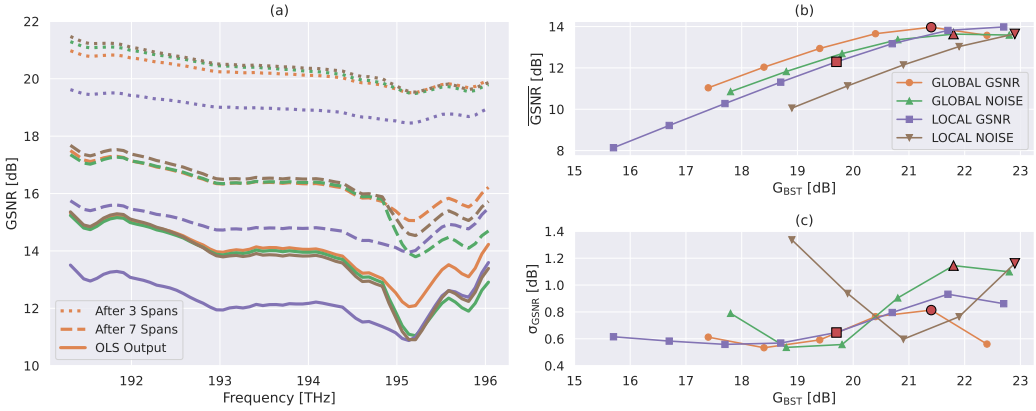

Fig. 3.20 Assessment on local vs. global optimization strategies: simulation results for the different optimization strategies: (a) GSNR profiles accumulated at different points of the OLS for the optimal configurations; GSNR aggregated metrics – (b) average, and (c) standard deviation – with respect to the BST gain varied in 1 dB steps (power sweep) at the end of the OLS.

Table 3.6 Assessment on local vs. global optimization strategies: optimized EDFA configurations.

	GLOBAL GSNR		GLOBAL NOISE		LOCAL GSNR		LOCAL NOISE	
[dB]	G_{tar}	T_{tar}	G_{tar}	T_{tar}	G_{tar}	T_{tar}	G_{tar}	T_{tar}
BST	21.4	-1.6	21.9	0.8	19.7	-1.8	22.9	-2.4
ILA 1	26.4	-4.8	26.5	-4.4	24.8	-2.5	26.3	-3.9
ILA 2	21.4	-0.8	21.0	-4.0	22.6	-2.1	20.6	-2.6
ILA 3	22.3	-0.7	22.1	-2.8	21.3	-2.2	21.9	-3.0
ILA 4	22.1	-4.8	22.2	0.1	21.9	-2.2	22.0	-2.9
ILA 5	24.7	-0.9	25.4	-4.9	24.8	-2.4	25.2	-3.3
ILA 6	21.6	-4.4	20.2	-1.6	21.9	-1.9	21.0	-2.4
ILA 7	23.0	0.3	22.8	-5.0	22.3	-2.3	22.1	-2.8
ILA 8	23.5	-4.4	25.8	-4.7	24.0	-2.3	25.0	-3.2
ILA 9	21.8	-2.4	19.9	-3.8	20.8	-2.2	19.5	-2.6
PRE	23.0	-5.0	23.6	-0.2	25.0	-0.7	25.0	-0.7

extracted configuration of gain and tilt parameters for the optical amplifiers, and then the estimation of the output metrics with the described physical layer model.

3.5.3 Results

The optimized EDFA configurations found applying the four strategies are reported in Tab. 3.6, while the corresponding results in terms of GSNR are depicted in Fig. 3.20. Repeating the optimization process, the execution time of the global strategies is more than one order of magnitude with respect to the corresponding local ones for the considered scenario, given the significant reduction of the number of variables and the complexity of the optimization space in the latter approach. Observing the obtained GSNR profiles (Fig. 3.20-a), it is evident how the high-frequency spectral zone undergoes the characteristic rippled behavior of the EDFAs [180], resulting in a more wrinkled trend of the performance accumulated as the WDM spectrum propagates through the OLS. Moreover, the curves of the GSNR average and standard deviation versus the BST gain, G_{BST}, give a perception of how the behavior of the space of the optimization problem is around the heuristic solution found. The metrics for the optimal configurations in Tab. 3.6 are represented by the larger red markers with an outline. The BST maximum gain cannot be higher than 23 dB as the amplifier will saturate given the total input power value.

Comparing the results obtained, the *global GNSR* strategy achieves the best performance in terms of average and flatness over the whole C band. The *local* and *global NOISE* strategies achieve similar outcomes, highlighting the choice of the first as more advantageous given the lower complexity of the optimization problem and the savings in terms of execution time. The *local GNSR* strategy does not bring about an optimal operative point of the effective OLS. A further refinement of the BST gain allows the system to achieve a performance comparable to the result of the *global GSNR* strategy.

3.6 Concluding Remarks

In this chapter, considering the SD cognitive optical networks, the case of the EDFA-amplified OLS has been investigated, proposing methodologies that allow optimizing the working point of the amplifiers to maximize the infrastructure capacity.

In particular, assuming a telemetry available inside the amplification sites such as EDFAs and OTDRs, this task revolves around a physical layer probing and characterization procedure that allows determining the parameters necessary for the model to reproduce the propagation behavior of the OLS with high accuracy.

After that, first two different amplifier configuration optimization approaches were formulated and the complete methodology was experimentally tested, reaching an accuracy on the predicted GSNR lower than 0.5 dB. Second, through simulation, this framework has been extended first by including the use of additional transceivers among the available telemetry and by simplifying the modeling required for the physical model thanks to an iterative supervised learning technique, then by expanding the range of optimization approaches by combining two cost functions and two observation strategies of the metrics of interest.

As future investigations, the goal is to scale the telemetry available for a given OLS and to propose cognitive methodologies for each scenario that can support the central network control system in transmission operation, trying to estimate both the achievable accuracy as the different operating zones of the OLS vary (e.g. linear, optimal or nonlinear regime), and the necessary or minimal computational resources.

Chapter 4

The Optical Network Case

In the following chapter, the object of investigation will increase in extension and complexity, moving from a single OLS to a complete optical network composed of TRXs, ROADMs and multiple OLSs. Remaining on the trend of SD open optical networks, a generic network architecture will be proposed to manage all NEs at the optical control plane level. Furthermore, the cognitive methodology described for a single OLS will be integrated into the overall functioning of the network, describing the interaction process between modules due to the different open interfaces necessary for the automation of the apparatus.

Since the network context is wider than that of a single line, the number of actors participating in the action of transmission operations also includes a Network Operating System (NOS) that implements the allocation of the optical connections derived from the requests of a hypothetical IP/application layer and part of the data plane.

Considering the context of long-haul core networks, the goal is to guarantee to the operations carried out by the network controller the evaluation of the maximum modulation format supported by a specific LP, first by optimizing the working point of the single lines and then executing the Light-Path Computation Engine (L-PCE) for the required physical paths. The software unit that performs these latter operations is an intelligent environment composed of physical models, data probed by telemetry, and algorithms, which interrogate the physical models fed with the appropriate data taken from the field and perform specific tasks. In a context in which the exchange of telemetry data and the control of the various NEs is made possible by compatible

interfaces, this software module can evolve into the form of a DT of the physical optical network.

After formalizing the composition and operation of the generic open network architecture including a cognitive optical control plane, it will be implemented in two different experiments. The first is on a triangular network, and the second on a linear network topology, with the aim of validating the behavior of the DT defined by measuring the GSNR thanks to the TRXs. In this way, the network orchestration operated by the central network controller is enabled by fully exploiting the available resources.

Recall that the optical amplifiers used during the experiments are commercial dual stage EDFAs that can be controlled by setting the gain and tilt, equipped with GFF between the two amplification stages.

In the discussion, the contents are taken from the following list of publications: [181–183].

4.1 Architecture

The proposed optical network architecture is designed to work in an open and disaggregated context, aiming to achieve interoperability among multi-vendor equipment and decouple the optical data and control planes. Specifically, the target approach is a partially disaggregated management [184] in which each node-to-node optical link is typically provided by a single vendor. Thus, the NEs of a line are meant to be handled by a single controller, collapsing the management to a single element from a network point of view. The representation in Fig. 4.1 schematizes an abstract open optical network structure.

Starting from the Physical Layer (PHY), the optical hardware infrastructure is composed of TRXs, ROADM white-boxes, optical fiber spools, and optical amplifiers. It is assumed that a couple of BST and PRE are integrated in a single ROADM for each switching direction. In this network architecture, a single OLS is defined as a ROADM-to-ROADM optical line, thus including the BST and the PRE of the ROADMs at both line terminals. Each amplification site along an OLS can host amplifiers of different technologies, e.g. EDFAs or Raman amplifiers, and telemetry devices, such as an OTDR, photodiodes, and OCMs. An optical node consists of

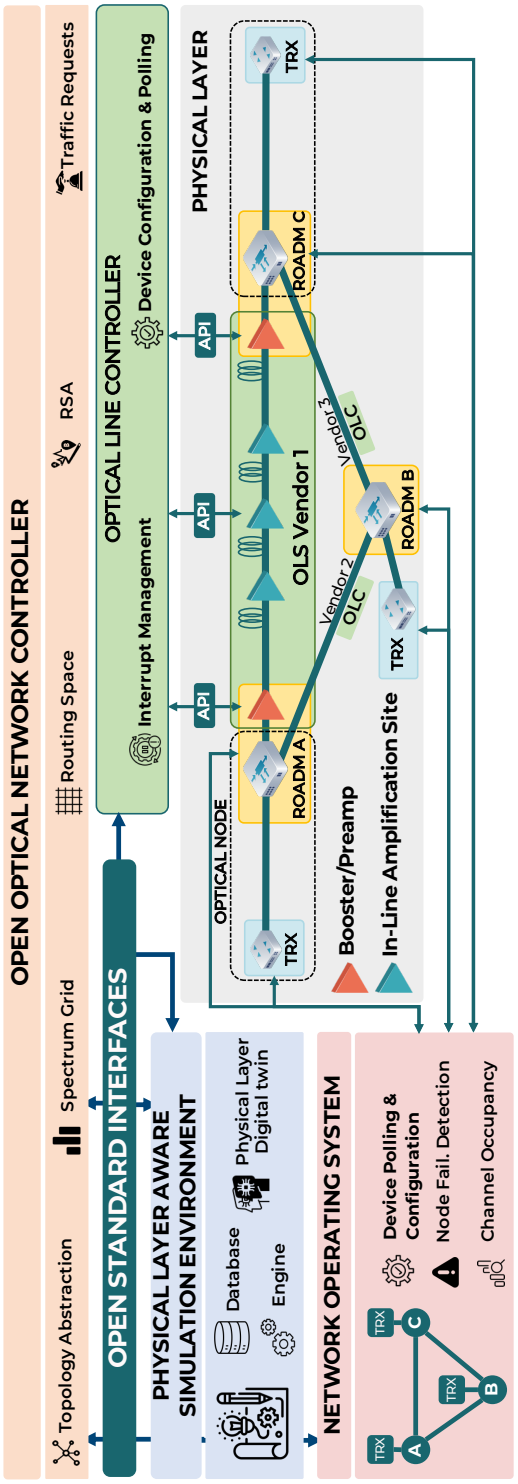

Fig. 4.1 Abstract scheme of the open and disaggregated optical network architecture, designed to independently implement the optical control and data planes through the interaction of the various outlined actors.

the set of TRXs and ROADMs placed in a specific location within the geographical footprint of the optical network.

The optical equipment is managed by the cooperation of four different software modules: (i) the NOS; (ii) an OLC for each OLS that makes up the optical network; (iii) the Physical Layer Aware Simulation Environment (PLASE); and (iv) the Open Optical Network Controller (OONC). Communication among the modules TRXs and ROADMs is carried out by exploiting open standard interfaces and protocols (REST, NETCONF, etc.).

The NOS is aware of the status of the optical nodes and their connections, building an abstraction of the network topology, and directly controls each TRX and ROADM within the network. Furthermore, the NOS must properly manage different types of failure detected in the PHY, both from nodes and lines. Each OLC is responsible for the management of the corresponding OLS, which is generally provided by a specific vendor. The OLC communicates through defined APIs with all the amplification sites of the OLS and the BST and the PRE, collecting telemetry information by means of device polling, configuring the amplifiers' working point, and notifying status information derived from interrupt management. The PLASE represents the building block of the network architecture within which all the intelligence regarding the PHY is collected. In particular, the PLASE stores data related to the PHY, such as datasets or amplifier/ROADM/TRX/fiber characterizations. The PHY-DT represents the central element of the PLASE, including the model of the physical layer and simulating the behavior of the system. On top of this, several computational algorithms (e.g. analytical and/or numerical procedures, artificial intelligence techniques) are run to fulfill different tasks related to the implementation of optical control, which relies on the PHY information knowledge and the interrogation of the PHY-DT. The PLASE directly communicates with both the OLCs and the OONC. With respect to the OLCs, the PLASE collects telemetry data from the NEs, performing fundamental operations such as the optimization of the working points of a specific OLS and the L-PCE [185].

The OONC implements the north-bound system interface exposed towards the network users. This module orchestrates the deployment process, for example, it transparently realizes the allocation and recovery of LP in the optical network, interacting with the other software modules (i.e., the NOS and the PLASE). Specifically, the OONC constructs the description of the spectrum grid by supplying a single con-

figuration for the active channel frequencies through a static external configuration recording the center frequencies for all optical WDM signals. As a result of the topology abstraction offered by the NOS, the routing space is then created and contains details on all possible pathways within the network, as well as the availability of the channel wavelength along each path. Using such structures, the OONC performs the RSA, helped by the PLASE transmission performance indicators, in response to incoming traffic requests from outside pairs of source-destination nodes. In the following, the behavior of the proposed network architecture is illustrated, focusing mainly on the optical control plane operations, showing its decoupled management with respect to the data plane from a procedural point of view.

4.1.1 Cognitive Optical Control Plane

The optical control plane is responsible for managing the optical equipment in order to maximize the exploitation of the installed resources in terms of transmission performance. This task requires the possibility of choosing the most advantageous strategy for the amplifiers' working point configuration, while minimizing the allocated margins [91]. The latter condition is directly related to the degree of knowledge of the PHY's devices, both lumped (optical switches, connectors, EDFAs) and components inducing distributed effects such as fibers or Raman amplifiers. In particular, the effect of lumped losses and fibers can be appreciated only in field by means of the indirect estimation of their properties. In this perspective, network provisioning can be performed after a probing procedure using available monitors and telemetry to completely characterize the PHY, in order to reduce the margin allocation. Cognitive property is the main feature of a class of optical networks bearing the same name [79, 80]. In the network context described above, the optical control plane is represented by the collection of all OLCs supervised by the PLASE. In the following, the procedural steps that lead to network provisioning are described, focusing on the case of a single OLS (Fig. 4.2). The procedure can be repeated over all the OLS, without loss of generality, given the partial disaggregation context. However, the process that leads the OLS to be ready to perform network operations is entirely dependent on the choices dictated by the OLS vendor, especially on the type of data that the OLC exposes.

After installation and before starting transmission operations, a OLS undergoes a tuning procedure targeting the definition of the working point of each amplifier

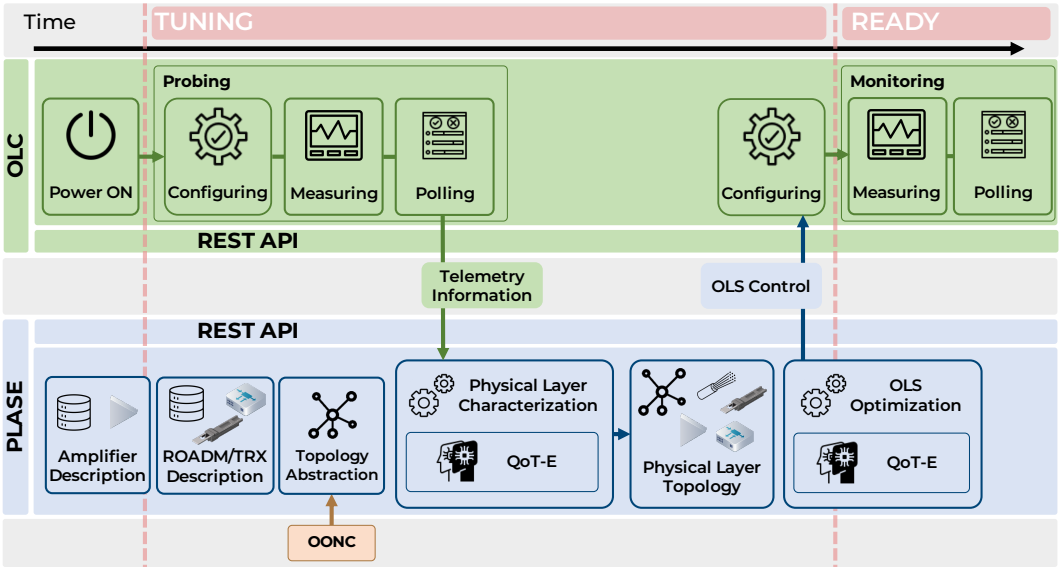

Fig. 4.2 Qualitative time line of the proposed cognitive optical control plane operation that leads an OLS to be ready for use.

along the line. This procedure is meant as an automated probing of OLS, with the aim of achieving a more accurate knowledge of PHY, capturing the behavior of the system directly from the field, and consequently adjusting the model adopted by the PHY-DT within the PLASE. Such a procedure is made up of three steps:

- Configuration of the equipment using predefined settings;
- Telemetry measurements of the quantities of interest;
- Device polling in order to collect the information.

A dedicated REST API is used to transfer data from OLC to PLASE and vice versa. The PLASE estimates the lumped losses and the properties of the fibers that match the measurements collected with the configuration of the equipment during the probing procedure, completing the characterization of the PHY. At the end of the probing procedure led by OLC, the related PHY descriptions of the amplifiers, TRXs and ROADMs are stored in a static database shared with PLASE. On top of such a detailed PHY model, OONC provides topology abstraction, describing the physical connections available between TRXs and ROADMs, allowing PLASE to identify the available OLS within the network. Therefore, PLASE is able to build the complete network PHY topology retrieving for each OLS the corresponding

virtualization that combines the virtual topology, the data measured by telemetry during the probing procedure, and the PHY descriptions. The PLASE defines the configuration of each amplifier within the specific OLS on the basis of the physical layer topology to optimally match the transmission strategy. The devised architecture assumes full spectral load operation on the basis of optical control. This is equivalent to defining the working point with respect to the worst-case scenario in terms of transmission performance. This assumption contributes to decoupling the operation of the data and control planes at an operational level, ensuring that the evaluation of the maximum modulation format cardinality for a specific path and wavelength is conservative even after LPs' further deployment. Once the configuration is received, the OLS is ready to operate as soon as the OLC sets the amplifiers at the design working point. During operations, OLC periodically monitors the OLS status by polling the telemetry devices.

4.2 Triangular Topology Optical Network

In this section, an implementation of the proposed network architecture is described building a proof-of-concept based on experimental multi-vendor equipment. The operation of the created triangular topology network is validated in terms of QoT performance based on the proposed cognitive optical control plane.

4.2.1 Experimental Setup

An experimental setup has been built in the LINKS Foundation's photonics laboratory with the aim of demonstrating the feasibility of such modular, open, and disaggregated optical network architecture by means of a proof-of-concept. The experimental setup that emulates an optical network is shown in Fig. 4.3 and is composed of 3 optical nodes (labeled as A, B and C), each equipped with commercial TRXs and ROADMs and connected by 3 multi-span amplified OLSs, obtaining different optical paths for CUTs. The TRXs are CFP2-DCO and Analog Coherent Optics (ACO) modules from Lumentum, programmed to generate 4 independent Dual Polarization (DP) signals (QPSK or 16QAM) and continuously monitor related BER, providing an updated average value every 15 seconds. The transmitters and receivers of the mentioned TRXs are plugged into Cassini AS7716-24SC [186] boxes,

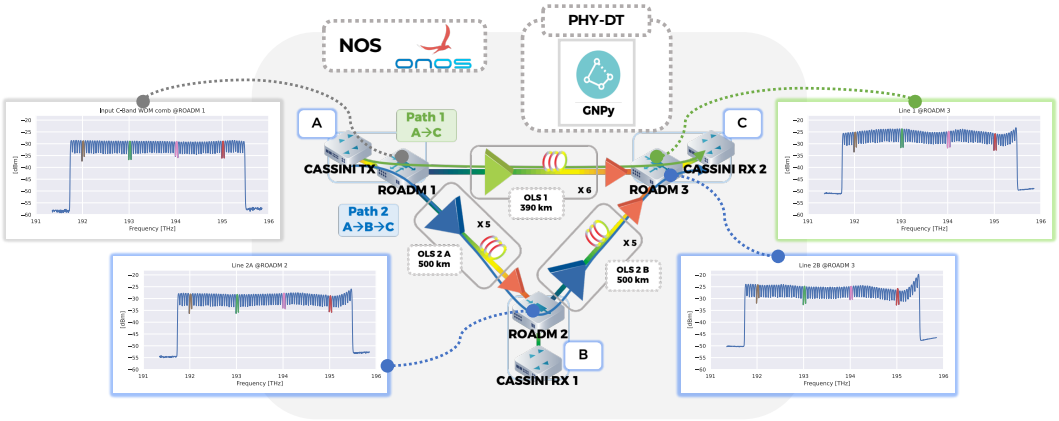

Fig. 4.3 Triangular topology optical network experimental setup, including the spectra of the C-band WDM comb propagated through the various optical nodes. ONOS holds the role of NOS, and GNPy represents the PHY-DT.

an Edgecore-built open network packet optical boxes that can host line card slots to incorporate ACO/DCO optical ports based on coherent digital signal processing and optical TRXs from leading optical technology partners. Each Cassini is operated by Network Operating System for Telecom & Operators (OcNOS), a proprietary operating system supplied by IP Infusion, providing configuration and monitoring facilities via NETCONF interfaces.

A C-band WDM comb centered at 193.5 THz and composed of 75 channels, 50 GHz spaced, modulated at 32 GBd each, is generated at the *Node A* side: 4 CUTs, centered at 192, 193, 194 and 195 THz, respectively, are generated by the TRXs (*Cassini TX*), while a commercial wave shaper filter (1000S from Finisar) is programmed to shape the output of an ASE noise source, generating 71 channels that, coupled with the 4 CUTs, assemble the 75 channels OLS spectral load with no loss of generality due to the large time constant characterizing the physical effects within EDFAs.

ROADM 1 can be configured to add the 75 channels and to route them towards *Node C*, either through *Path 1* or *Path 2*. The former straight, *OLS 1*, connects *Node A* to *Node C* through 6 spans, each based on commercial EDFA operating in constant gain mode and followed by a SSMF of 65 km nominal length. *OLS 2A* and *OLS 2B*, composing *Path 2*, consist of 5 amplified SSMF spans of about 100 km each. In the middle of *Path 2*, *ROADM 2* can drop the CUTs, so that their BER can be evaluated (*Cassini RX 1*), or forward them towards *Node C*. *ROADM 3* finally

drops the 4 CUTs and *Cassini RX 2* evaluates the related BER values, if they are propagated through *Path 1* or *Path 2*. The EDFAs corresponding to the two paths come from two different vendors, sized according to the average total loss of the fiber span present in the specific path.

The software implementation includes ONOS, version 2.7.0, as NOS with some additional custom features developed for this proof of concept. For the first time, ONOS is capable of providing the frequency slot occupation per link with a granularity of 12.5 GHz using new custom REST endpoints. Moreover, specific drivers have been developed that enable the control of TRXs through the Cassini operating system OcNOS, including the configuration of the desired modulation format. In particular, ONOS has been extended to provide visibility of the availability of optical spectrum resources to the OONC module. In addition, specific software drivers for ONOS have been developed to correctly configure the YANG model exposed by OcNOS to represent the corresponding Cassini box.

For this proof of concept, a QoT-driven approach is adopted, with the aim of favoring vendor-agnostic network management. Within the PLASE, GNPy provides the optical propagation model of the PHY-DT. ONOS and the PLASE are hosted on two different servers in order to emulate the cloud environment. ONOS's server is equipped with an Intel(R) Pentium(R) CPU G860 @3.00 GHz and 16 GB of RAM. The PLASE runs on a server powered by Intel(R) Core(TM) i7-4980HQ CPU @2.80 GHz and 16 GB of RAM. OONC is implemented as a Python framework that orchestrates the other software modules, exposing multiple REST endpoints developed based on the Flask library. Each OLC exploits a Secure Shell (SSH) protocol that allows to open a control flow enabling to set and poll the EDFA's parameters (e.g. gain, tilt target parameters) and performance monitors (e.g. OCM measurement, input and output total optical power).

4.2.2 Results

In the following, all experimental results related to the validation of the network optical transmission and the LP-recovery use case are reported and commented on, illustrating the relevant observations and details in terms of practical implementation. Both the PHY characterization and OLS control optimization methodologies adopted in this work are taken from [140].

The experimental setup presents two different models of ILAs according to the nominal length of the specific fiber span (65 or 100 km) and a BST and a PRE integrated into the Lumentum ROADMs. Preliminarily, both types of ILA have been characterized with full spectral load in constant gain mode, varying the gain and tilt parameters with different values of total input power. Each collected data set is used to create a ML model, one for each amplifier type, training 2 different ANNs, abstracting the behavior of the gain profile and the introduced ASE noise profile, respectively (see Sect. 3.4.2). The ROADM's BST and PRE have been similarly characterized at full spectral load in constant output power mode for different output power values varying the total power of the input C-band spectrum. The abstraction of these components by software is obtained for both the applied gain and introduced ASE noise linearly interpolating in logarithmic units the measured quantities. Both the TRX types (ACO/DCO) have been characterized in B2B to obtain the BER versus SNR curves and consequently retrieve the related SNR threshold assuming 10^{-2} as pre-FEC (forward error correction) BER threshold for each available modulation format. To measure GSNR, as graphically explained in Fig. 3.2, the method used is to translate the measured BER from Cassini by means of the B2B characterization, obtaining the corresponding SNR [141].

Physical Layer Characterization

The measurement process bringing to the definition of the PHY topology begins with an OTDR analysis, performed for each fiber span that measures the length of the fiber span, L_S, and the positions of eventual lumped losses, l, present along the specific span. After that, the BST and each in-line EDFA are set in ASE mode providing at the corresponding output a full C-band ASE spectrum with an arbitrary shape. The latter is measured by OCMs at both terminals of each fiber span. The two ASE power levels are defined according to the characteristics of the installed apparatus, such as EDFAs' maximum total output power and fiber span total losses, and to the telemetry sensitivity.

The PLASE characterizes each fiber span through an optimization strategy that aims to reproduce the experimental measurements using the PHY optical propagation model. The PHY parameters to estimate for a single fiber span are the Raman gain coefficient scaling factor, K_R, the loss coefficient function, α, the input, $l(0)$, and

Table 4.1 Triangular topology optical network: complete set of physical layer parameters retrieved from the characterization procedure.

OLS	SPAN	L_S [km]	K_R [1/W/km]	D [ps/nm/km]	$l(0)$ [dB]	$l(L_S)$ [dB]
1	1	65.5	0.34	16.6	5.5	0.1
	2	65.3	0.34	16.8	1.4	0.3
	3	65.5	0.44	16.7	1.6	0.1
	4	65.6	0.34	16.7	0.2	1.4
	5	65.2	0.42	16.7	0.5	0.4
	6	65.8	0.34	16.5	0.1	1.3
2A	1	106.2	0.34	17.5	3.6	0.2
	2	107.5	0.44	17.9	1.2	0.7
	3	106.2	0.44	17.7	1.5	0.1
	4	108.8	0.42	17.7	0.6	0.1
	5	108.3	0.42	17.8	0.2	0.1
2B	1	106.2	0.42	17.9	1.1	0.2
	2	106.8	0.34	17.7	0.1	0.1
	3	106.4	0.34	17.7	0.2	0.7
	4	107.3	0.42	17.8	0.2	0.1
	5	108.3	0.42	17.8	0.5	2.3

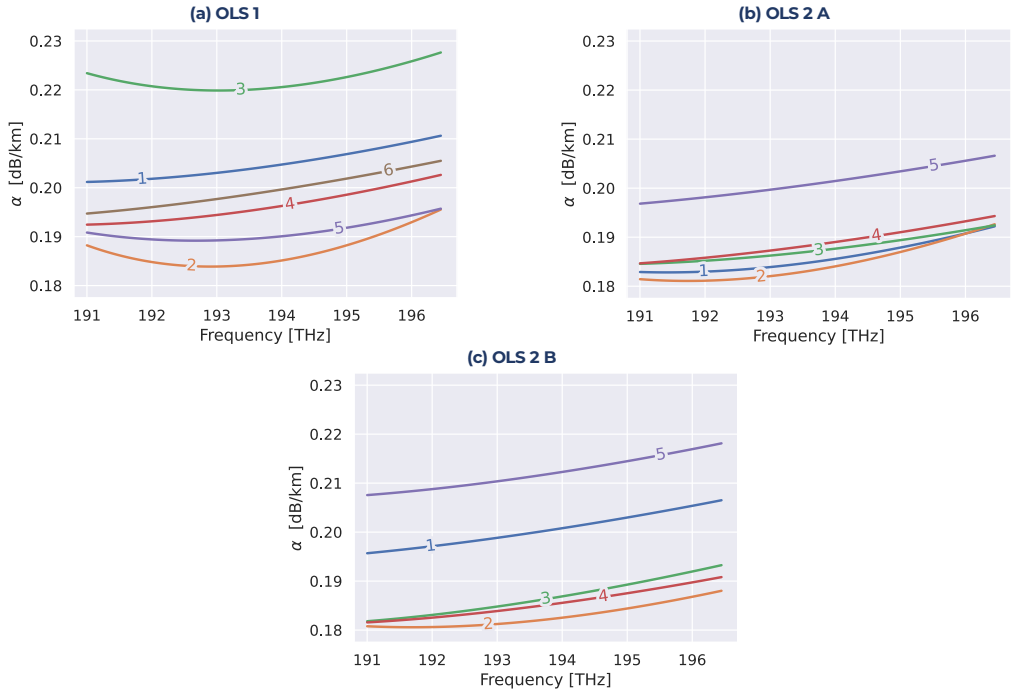

Fig. 4.4 Triangular topology optical network: retrieved loss coefficient functions for each optical fiber span by means of the physical layer characterization procedure.

the output connector losses, $l(L_S)$, and the eventual lumped losses detected by the OTDR, $l(0 < z < L_S)$.

The results of the PHY characterization are shown in Tab. 4.1 and Fig. 4.4. Given a specific OLS within the optical network, each fiber span is characterized in terms of the PHY parameters described above. Additionally, the dispersion coefficient, D, was measured for each span before complete equipment installation. According to the data sheet, the equivalent representations retrieved by the characterization process correspond to the properties of the SSMF type.

OLS Control & Transmission Performance

Based on the PHY topology, the PLASE optimizes the amplifier working point feeding the PHY model with the parameters recovered following the methodology described in Sect. 3.3. The result of the optimization process following Eq. 3.6 as a cost function is reported in Tab. 4.2, with the aim of homogeneously optimizing and flattening the profile GSNR throughout the band considering the fiber and amplifier propagation model. All integrated amplifiers within each ROADM (BST and PRE) are set to work in fixed output power mode. Instead, the ILAs are set in fixed gain mode. Adjustment of the amplifier working point takes place for each individual OLS by modifying the target parameters of the device, such as total output power, gain, or tilt, consulting the PHY-DT for each extracted configuration and evaluating the resulting GSNR profile at the PRE output of the considered OLS.

The evaluation of the network transmission performance obtained following the described cognitive approach is performed by setting the amplifier working point and estimating the GSNR of each CUT for both the LPs based on the measured BER. Each GSNR estimation is compared to the value of GSNR predicted by GNPy, determining the related resulting margin. The latter is calculated without considering any other contribution, as if the system worked at zero margin. The summary of the experimental measurement campaign is presented in Tab. 4.3. The measure of the BER using the DP-16QAM modulation format has been possible only for the case of the short path, *Path 1*. Observing the results, the fact that DCO TRXs provide larger margins than ACO is remarkable, which presents higher intrinsic device robustness. This difference in margin between the two TRX types is mainly due to the different implementation of the receiver DSP and their ability to mitigate optical transmission

Table 4.2 Triangular topology optical network: EDFA optimal target parameter configurations of each OLS.

OLS	AMPLIFIER	G_{tar} [dB]	T_{tar} [dB]	$P_{OUT,tar}$ [dBm]
1	BST	–	–	21.8
	ILA 1	15.0	-0.1	–
	ILA 2	15.0	-1.4	–
	ILA 3	15.0	0.0	–
	ILA 4	15.0	0.6	–
	ILA 5	15.7	-1.0	–
	PRE	–	–	20.0
2A	BST	–	–	21.8
	ILA 1	23.3	-5.0	–
	ILA 2	22.1	-5.0	–
	ILA 3	21.6	-1.9	–
	ILA 4	22.9	-1.0	–
	PRE	–	–	23.0
2B	BST	–	–	19.2
	ILA 1	22.0	-5.0	–
	ILA 2	22.2	-4.8	–
	ILA 3	23.3	-1.9	–
	ILA 4	23.0	-1.4	–
	PRE	–	–	20.0

penalties (e.g. CD, PMD) [88]. The latter cannot be taken into account during the TRX B2B characterization of the TRX as optical propagation is not involved in the process. The presence of these penalties is evident in both TRX types, observing a reduction of the margins in the case of the longer path with respect to the shorter one. Comparing the results inherent to *Path 1* for the different modulation formats, it is observed that the estimated GSNR for the ACO modules are comparable, as expected given that the degradation introduced by the network does not change. Instead, there is a non-negligible variation for the DCO TRXs changing the modulation format. Since the QoT is very high for these TRXs, this can be explained by the location of the working point within the B2B curve, which is affected by greater uncertainty during the characterization phase. The GNPy GSNR prediction is conservative in all cases, obtaining a satisfactory result working with zero margin. Given these considerations, the degree of flatness of the measured QoT also corresponds to the prediction based on the optimization criterion.

Table 4.3 Triangular topology optical network: : transmission performance validation results.

		Path 1 (A –>C)				**Path 2 (A –>B –>C)**			
		CUT 1 DCO (192 THz)	**CUT 2 ACO (193 THz)**	**CUT 3 DCO (194 THz)**	**CUT 4 ACO (195 THz)**	**CUT 1 DCO (192 THz)**	**CUT 2 ACO (193 THz)**	**CUT 3 DCO (194 THz)**	**CUT 4 ACO (195 THz)**
GNPy Prediction [dB]		24.0	23.7	23.7	23.6	18.4	17.8	18.1	17.6
QPSK (100G)	**BER**	1.6e-08	9.5e-08	1.2e-08	8.6e-08	4.2e-05	1.9e-04	3.5e-05	1.4e-04
	GSNR [dB]	27.1	24.6	27.5	24.7	19.1	17.7	19.2	18.0
	Margin [dB]	3.1	0.9	3.7	1.1	0.6	0.0	1.1	0.4
16-QAM (200G)	**BER**	3.9e-03	9.9e-03	4.2e-03	1.1e-02	–	–	–	–
	GSNR [dB]	26.3	25.0	26.0	24.7	–	–	–	–
	Margin [dB]	2.3	1.3	2.2	1.0	–	–	–	–

4.3 Linear Topology Optical Network

In this section, another proof-of-concept based on a linear topology demonstrates the functionality of the proposed cognitive optical control plane within the general open optical network architecture. The experimental setup is similar to the previous experiment, varying the assembly of the elements and the analyzed use-case.

4.3.1 Experimental Setup

The experimental setup implements the optical network scheme depicted in Fig. 4.5 and in the following only the difference with respect to Sect. 4.2.1 will be described, considering the remaining part unchanged with respect to the previous setup. Line 1 is composed by 6 spans, each based on a commercial EDFA operating in constant gain mode and followed by a SSMF of 65 km nominal length. Similarly, line 2 is composed by 10 amplified SSMFs spans of about 100 km each. Each line has a different commercial EDFA model provided by a different vendor, sized for the fiber span used. Three commercial ROADMs (from Lumentum) are used to emulate network nodes: ROADM 1 is configured to add the 75 channels and to route them at the line 1 input (Fig. 4.6-a); ROADM 2 drops two CUT (CUT 1 and CUT 2), so that their BER can be evaluated at the end of line 1. The 73 remaining channels are then propagated through line 2 (Fig. 4.6-b) and ROADM 3 finally drops CUT 3 and CUT 4 at the end of line 2 (Fig. 4.6-c). The SD network controller, ONOS, controls the ROADMs and the Cassini packet optical boxes using the NETCONF

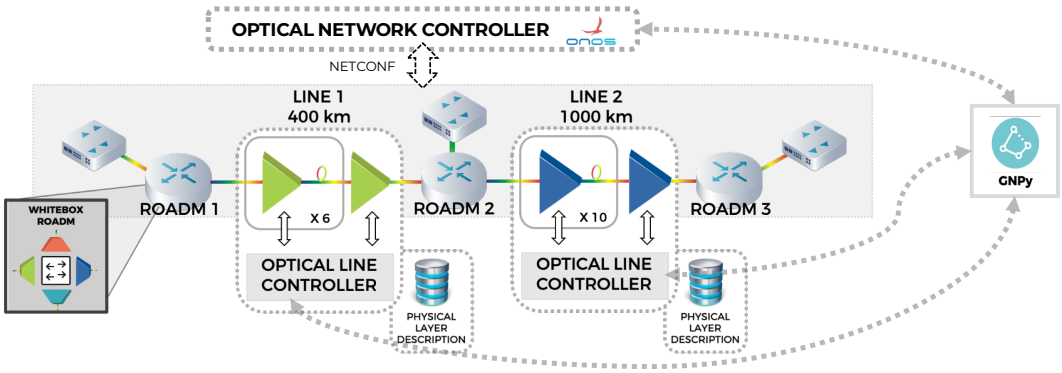

Fig. 4.5 Linear topology optical network experimental setup hosting two OLSs and three ROADMs.

protocol [187]. The drivers for controlling such devices were already available in the ONOS master code branch, but significant extensions have been implemented for this deployment. Specifically, the OcNOS operating system installed on the Cassini boxes uses a YANG model not compliant with the OpenConfig model. So, the extended driver applies to the proprietary OcNOS YANG model and provides the following features: device and port discovery, tuning of the laser frequency, modulation format and output power configuration, and pre-FEC BER monitoring. Moreover, the ONOS Command-Line Interface (CLI) has been extended to allow the configuration of a single cross-connection on ROADM devices. For the purposes of the experiment, 75 intents are established in the network with explicit path and wavelength assignment: four of them are used for propagation of modulated traffic, the others for ASE noise propagation. To deal with the configuration of the noise intents, 2 emulated OpenConfig transponders are added to the network topology.

4.3.2 Results

As preliminary steps to the experiment, a single amplifier of each EDFA model involved in the experiment undergoes a characterization process, which allows to map the effective gain and ASE noise generated by the corresponding settings. A B2B characterization of the DCO modules hosted in Cassini is carried out for each modulation format and different received power levels, deriving the corresponding BER vs. SNR characteristic curves. Once the experimental setup is established, the fiber spans of both OLSs are characterized to abstract their physical layer properties according to the methodology presented in Sect. 3.3. Also, the working point of the amplifiers of both lines is individually optimized by maximizing and flattening the GSNR at their output following the cost function expressed by Eq. 3.6. The proper operation of the presented proof-of-concept is experimentally verified measuring the real pre-FEC BER of the dropped modulated channels using the Cassini at each line terminal and translating them into the corresponding GSNR value by means of the previously obtained B2B characteristic curves. The measurements are performed on CUT 1 and CUT 2 dropped by the ROADM 2 using both the DP-QPSK and DP-16-QAM modulation formats and on CUT 3 and 4 after the ROADM 3 only in DP-QPSK.

The results obtained in terms of GNPy predictions and experimental measurements are reported both graphically and in a table in Fig. 4.6-d and Tab. 4.4, respec-

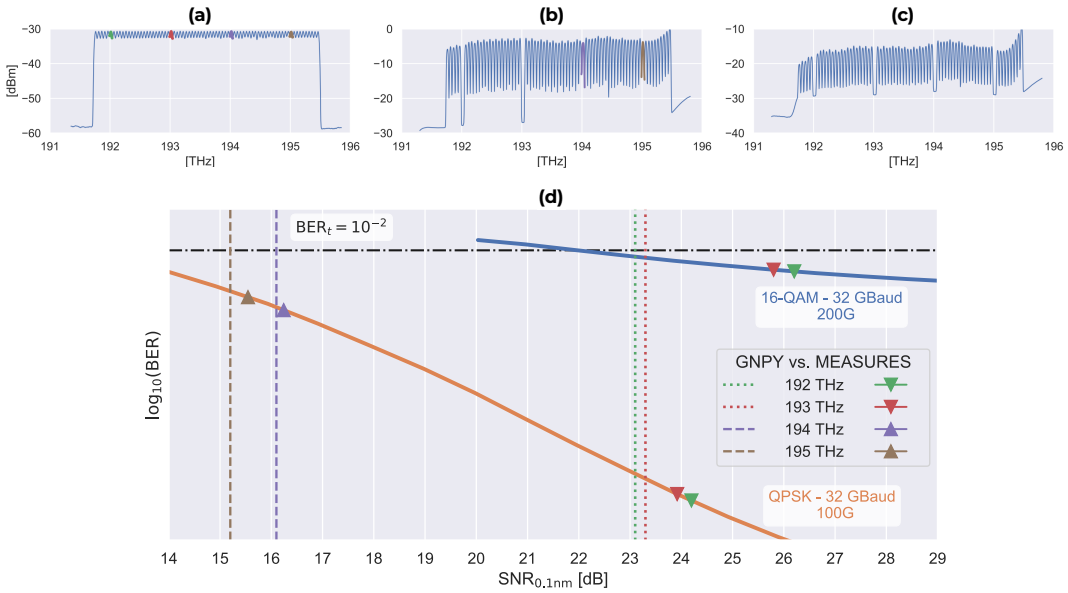

Fig. 4.6 Linear topology optical network: (a) propagating WDM comb at line 1 input after ROADM 1, (b) line 2 input after ROADM 2, (c) line 2 output after ROADM 3. Comparison between GNPy predictions and experimental measurements.

tively. GNPy estimations are in all cases conservative with respect to the experimental values. When comparing them with respect to the DP-QPSK measurements, the deviation is within 1.1 dB. Focusing on the CUT 1 and 2, we observe a larger GNPy/measured-GSNR gap on DP-16QAM with respect to DP-QPSK. Furthermore, the GSNR trend versus CUT frequency between GNPy predictions and measurements is opposite with respect to both measured modulation formats. The first aspect is related to a pejorative characterization of the amplifiers, since the transmission

Table 4.4 Linear topology optical network: comparison between GNPy predictions and experimental measurements.

		GNPy prediction [dB]	QPSK		16-QAM	
			GSNR [dB]	BER	GSNR [dB]	BER
LINE 1	CUT 1 (192 THz)	23.1	24.2	9.1e-09	26.2	3.1e-03
	CUT 2 (193 THz)	23.3	23.9	1.3e-04	25.8	3.4e-03
LINE 1+2	CUT 3 (194 THz)	16.1	16.2	3.6e-04	–	–
	CUT 4 (195 THz)	15.2	15.5	7.4e-04	–	–

quality is not yet degraded by optical propagation after about 400 km. Given the almost flat prediction, the BER measurements reflect this statement, presenting values that are considerably similar. The opposite trend is instead related to the uncertainty associated with the measurement and the fiber span characterizations. In any case, assuming a BER threshold of 10^{-2}, GNPy prediction sustains and ensures the possibility of using DP-16-QAM connections for both CUTs. Taking into account the case of CUT 3 and CUT 4, GNPy prediction is extremely accurate with respect to the measurements obtained after about 1400 km of optical propagation.

4.4 Concluding Remarks

In this chapter, the case of the optical network has been addressed following an open, disaggregated SDN management approach, in which the task performed by the central network controller is supported by the intervention of the DT of the network. In this context, the architecture is defined starting from the existence of open interfaces in which standard protocols and shared structures are used. The exchange of data between the intelligence unit and the various NEs in terms of telemetry information and operational configurations of the NEs allows the physical models to evolve into the form of the DT, updating the parameters with which they are fed during the execution of the various engines.

This situation represents one of the highest stages in which it is possible to apply cognitive methodologies in a natural way, in which it is possible to derive the characteristics of the physical system by probing its behavior, optimizing its functioning, and predicting its behavior in other work regions, also leading to the definition of the margins and countermeasures in case of failure. All this with an accuracy that usually depends on the telemetry data available, both in terms of type (which metrics are evaluated) and quantity (collection of datasets for application of artificial intelligence).

Ultimately, the automation of the infrastructure combined with the definition of shared data structures paves the way for the orchestration of the optical infrastructure in a modular way, introducing the characteristics of scalability, multi-vendor, interoperability and flexibility to the system. Starting from the proposed architecture and the two shown experiments, in the field of long-haul open optical networks, it

is clear that there is still a lot of room to implement new functionalities, integrate different devices, and experiment new engines and algorithms.

Chapter 5

Conclusion & Future Work

In conclusion, this work has explored the application of cognition and automation in the physical layer of optical networks, with the aim of defining vendor-agnostic control procedures and architectures that can autonomously maximize the capacity of the optical infrastructure.

As reviewed in Chap. 1, the use of an open SDN approach combined with NFV has been identified as an efficient solution to increase service capacity and system management in response to the increasing demand for Internet data traffic. Moreover, the ability of the infrastructure to be agnostic with respect to the adopted vendor equipment has been highlighted as an important characteristic for an efficient usage of optical networks. In particular, the two-step cognitive optimization process applied during the provisioning phase of an optical network, based on the joint use of a physical layer model capable of simulating the behavior of the system and information retrieved from the installed NEs, has been shown to be effective in maximizing the capacity of the system considered. This has been achieved through the development of novel vendor-agnostic control procedures and architectures, which have been successfully applied to different use-cases.

In Chap. 2, the case of optical DRA has been investigated having available different monitoring elements, integrated photodiodes and OCMs, and different transmission conditions, single and multiband. For each scenario, an architecture of the cognitive local controller of the amplifier has been defined, and consequently procedures have been defined which lead to the regulation of the pump power levels

so that the optical propagation of the WDM signal corresponds to the specifications required by the central control system.

Looking at possible future improvements, the optimization of DRA can be extended by considering the introduced ASE noise, and thus the noise figure of the amplifier. In this perspective, the fulcrum of optimization would become the OSNR, which is also affected by the high gains of the Rayleigh backscattering triggered by the Raman pumps [188]. In a larger context where multiple fiber spans or entire ROADM-to-ROADM links are considered, joint optimization of EDFAs and DRAs can be performed, similar to the process that will be described in the next chapter considering as reference metric the GSNR.

In Chap. 3, the research has focused on the optimization of the performance of a ROADM-to-ROADM optical link composed of a sequence of EDFA-amplified fiber span, demonstrating that the QoT over all the channels propagating through the link can be maximized and flattened. This optimization takes place by exploiting a physical layer model fed with parameters derived in order to replicate the propagation behavior measured in the field by the available monitoring devices. Furthermore, the range of optimization strategies developed has been explored more widely through a simulation campaign by comparing two different approaches, a local one, defining the working point of each amplifier individually, and a global one, defining the working point of all the amplifiers jointly, using realistic modeling of the amplifiers and fiber spans. Then, exploiting a set of auxiliary TRXs, the possibility of iteratively refining the working point of the amplifiers according to the desired strategy was explored at a simulation level by introducing an ML agent which, using an iterative supervised learning approach, is capable of coping with uncertainties from the physical layer.

In forthcoming investigations, the focus revolves around the amplification of accessible telemetry for a designated OLS, together with the formulation of cognitive methodologies tailored to individual scenarios. These methodologies are intended to strengthen the central network control system during the transmission operation process. A primary ambition involves evaluating achievable accuracy while accommodating fluctuations across the distinct operational domains of OLS, spanning the linear, optimal, and non-linear regimes. Furthermore, an exploration of indispensable or minimal computational resources will be conducted in tandem. This collaborative effort aims to improve our understanding of OLS behaviors and

their interactions on the network, helping to improve the propagation performance and resource management paradigms.

In Chap. 4, after suitably defining an open SD optical network architecture, the cognitive techniques defined for an OLS were applied to two different network topologies, one triangular and one linear, experimentally verifying that the cognitive approach leads the control system to establish an optimal working point for the optical infrastructure.

As a continuation of the research activity, towards a more effective and sophisticated DT, future work can focus on improving the orchestration and the management of optical networks within the control system, increasing flexibility and adaptability with respect to several scenarios, in terms of available NEs, monitoring devices and WDM spectrum specifications. Investigation and implementation of ad hoc artificial intelligence techniques can be explored to enhance system reaction in case of soft/hard failures and support automatic re-optimization strategies, involving also a dynamic margin evaluation according to the current deployed LPs. In addition, continuous monitoring of the metrics of interest in an optical network operated by a carefully designed telemetry structure makes it possible to collect information directly or indirectly useful for characterizing phenomena that are difficult to quantify in the calibration or provisioning phase. This is the case of penalties related to the DSP operation on the receiver, such as CD, PMD or PDL, but also the penalties derived from the filtering undergone during propagation and component aging.

Since all the results presented relate to a full spectral load condition, a discussion of the working condition with variable spectral load is dutiful. The use of the latter is currently limited in optical networks to the case of single-band transmission with EDFA amplification. The reason lies in the fact that in distributed Raman amplification and multi-band transmission systems, the significant variation of the spectral load can lead to a difficult to control instability linked to the propagation of power transients inside the optical lines during the operation of a network. This is induced by the progressive introduction of channels into the spectral load, which modifies the response of the SRS and of the EDFAs, respectively. In general, the advantage of a network architecture which works in the variable spectral load condition lies in the simplicity of managing the WDM comb (use of modulated channels only) and, therefore, a lower cost both in terms of apparatus and control. The price to pay in terms of performance is represented by the fact that the GSNR is

no longer a static metric, as in the case of the full spectral load, but varies according to the history of the network. Therefore, assuming to bring the operation of the system to zero margin, it is necessary to increase the complexity of the model to take into account the phenomena mentioned above. In particular, it is necessary to accurately define the characteristics of an LP (i.e., bit rate, symbol rate and modulation format) considering both the constraints of the request from the network and the current transmission quality. In a single-band transmission context, the variable spectral load condition is used, but it is difficult to fully exploit the potential of the infrastructure, given that large margins are defined to compensate for inaccurate QoT-E. The application of cognitive techniques and artificial intelligence in this context assumes a position of absolute importance, but requires a highly automated framework that operates in an adaptive manner according to the type of devices available.

Overall, the findings of this research pave the way for the development of more efficient and effective optical networks capable of meeting the growing demand for Internet data traffic.

References

[1] Department of Economic United Nations and Population Division Social Affairs. World population prospects 2019, online edition. https://population.un.org/wpp/Download/Standard/Population/, 2021.

[2] Internet World Stats. World internet users and 2022 population stats. https://www.internetworldstats.com/stats.htm, 2022.

[3] McKinsey & Company. How covid-19 has pushed companies over the technology tipping point – and transformed business forever. *McKinsey & Company Insights*, 2021.

[4] Cisco. Cisco annual internet report (2018–2023). https://www.cisco.com/c/en/us/solutions/collateral/executive-perspectives/annual-internet-report/white-paper-c11-741490.html, 2021.

[5] Saleh. Evolution toward the next-generation core optical network. *Journal of lightwave Technology*, 24(9):3303–3321, 2006.

[6] Ioannis Tomkos, Biswanath Mukherjee, Steven K Korotky, Rodney S Tucker, and Leda M Lunardi. The evolution of optical networking. *Proc. IEEE*, 100(5):1017–1022, 2012.

[7] Adel AM Saleh and Jane M Simmons. All-optical networking—evolution, benefits, challenges, and future vision. *Proceedings of the IEEE*, 100(5):1105–1117, 2012.

[8] Patricia Layec, Annalisa Morea, Francesco Vacondio, Olivier Rival, and Jean-Christophe Antona. Elastic optical networks: The global evolution to software configurable optical networks. *Bell Labs Technical Journal*, 18(3):133–151, 2013.

[9] Jeff Hecht. A short history of laser development. *Applied optics*, 49(25):F99–F122, 2010.

[10] Charles K Kao. Nobel lecture: Sand from centuries past: Send future voices fast. *Reviews of Modern Physics*, 82(3):2299, 2010.

[11] Georgios I Papadimitriou, Chrisoula Papazoglou, and Andreas S Pomportsis. Optical switching: switch fabrics, techniques, and architectures. *Journal of lightwave technology*, 21(2):384–405, 2003.

[12] Renato Valentini. 15 settembre 1977, torino, prima stesura al mondo di una fibra ottica in esercizio. un record detenuto da tim. https://web.archive.org/web/20170917171214/http://archiviostorico.telecomitalia.com/italia-al-telefono-oltre/15-settembre-1977-torino-prima-stesura-al-mondo-di-fibra-ottica-in-esercizi, 2017.

[13] Jeff Hecht. *City of light: the story of fiber optics*. Oxford University Press on Demand, 2004.

[14] Stuart Abbott. Review of 20 years of undersea optical fiber transmission system development and deployment since tat-8. In *2008 34th European Conference on Optical Communication*, pages 1–4. IEEE, 2008.

[15] F Pirio and JB Thomine. The sea-me-we 3 undersea cable system. In *OFC'98. Optical Fiber Communication Conference and Exhibit. Technical Digest. Conference Edition. 1998 OSA Technical Digest Series Vol. 2 (IEEE Cat. No. 98CH36177)*, pages 273–274. IEEE, 1998.

[16] Ethernet Task Force. Ieee p802. 3ae 10gb/s, june 2002.

[17] C Cole. Ieee p802. 3ba. 40 gb/s and 100 gb/s ethernet task force public area. *http://www. ieee802. org/3/ba/public/may08/cole_01_0508. pdf*, 2008.

[18] Valey Kamalov, Ljupcho Jovanovski, Vijay Vusirikala, Eduardo Mateo, Yoshihisa Inada, Takaaki Ogata, Kenichi Yoneyama, Pascal Pecci, David Seguela, Olivier Rocher, et al. Faster open submarine cable. In *2017 European Conference on Optical Communication (ECOC)*, pages 1–3. IEEE, 2017.

[19] Valey Kamalov, Ljupcho Jovanovski, Vijay Vusirikala, Shaoliang Zhang, Fatih Yaman, Kohei Nakamura, Takanori Inoue, Eduardo Mateo, and Yoshihisa Inada. Evolution from 8qam live traffic to ps 64-qam with neural-network based nonlinearity compensation on 11000 km open subsea cable. In *Optical Fiber Communication Conference*, pages Th4D–5. Optica Publishing Group, 2018.

[20] Ronen Dar, Peter J Winzer, AR Chraplyvy, Szilard Zsigmond, K-Y Huang, Herve Fevrier, and Stephen Grubb. Cost-optimized submarine cables using massive spatial parallelism. *Journal of Lightwave technology*, 36(18):3855–3865, 2018.

[21] Hitoshi Takeshita, Masaki Sato, Yoshihisa Inada, Emmanuel Le Taillandier de Gabory, and Yuichi Nakamura. Past, current and future technologies for optical submarine cables. In *2019 IEEE/ACM Workshop on Photonics-Optics Technology Oriented Networking, Information and Computing Systems (PHOTONICS)*, pages 36–42. IEEE, 2019.

[22] Emmanuel Desurvire. Optical communications in 2025. In *2005 31st European Conference on Optical Communication, ECOC 2005*, volume 1, pages 5–6. IET, 2005.

[23] Daniel Kilper, Keren Bergman, Vincent WS Chan, Inder Monga, George Porter, and Kristin Rauschenbach. Optical networks come of age. *Optics and Photonics News*, 25(9):50–57, 2014.

[24] Kazuro Kikuchi. History of coherent optical communication and challenges for the future. In *2008 Digest of the IEEE/LEOS Summer Topical Meetings*, pages 107–108. IEEE, 2008.

[25] Han Sun, Kuang-Tsan Wu, and Kim Roberts. Real-time measurements of a 40 gb/s coherent system. *Optics express*, 16(2):873–879, 2008.

[26] Kim Roberts and Charles Laperle. Flexible transceivers. In *European Conference and Exhibition on Optical Communication*, pages We–3. Optica Publishing Group, 2012.

[27] Tie Sun, John Rogers, Mike Rogers, Ian Dedic, Mahdi Parvizi, Ying Zhao, Li Chen, Long Chen, and Ricardo Aroca. Silicon photonic mach-zehnder modulator driver for 800+ gb/s optical links. In *2021 IEEE BiCMOS and Compound Semiconductor Integrated Circuits and Technology Symposium (BCICTS)*, pages 1–5. IEEE, 2021.

[28] Po Dong, Jing Chen, Argishti Melikyan, Tianren Fan, Taylor Fryett, Changyi Li, Jiashu Chen, and Chris Koeppen. Silicon photonics for 800g and beyond. In *Optical Fiber Communication Conference*, pages M4H–1. Optica Publishing Group, 2022.

[29] Hideki Isono. Latest standardization trend and future prospects for 800g/1.6 t optical transceivers. In *Next-Generation Optical Communication: Components, Sub-Systems, and Systems XII*, volume 12429, pages 45–51. SPIE, 2023.

[30] CR Giles, Emmanuel Desurvire, John L Zyskind, and Jay R Simpson. Erbium-doped fiber amplifiers for high-speed fiber-optic communication systems. In *Fiber Laser Sources and Amplifiers*, volume 1171, pages 318–327. SPIE, 1990.

[31] AW Naji, Belal Ahmed Hamida, XS Cheng, Mohd Adzir Mahdi, S Harun, Sheroz Khan, WF Al-Khateeb, AA Zaidan, BB Zaidan, and Harith Ahmad. Review of erbium-doped fiber amplifier. *International Journal of the Physical Sciences*, 6(20):4674–4689, 2011.

[32] Hongyue Zhu and Biswanath Mukherjee. Online connection provisioning in metro optical wdm networks using reconfigurable oadms. *Journal of Lightwave Technology*, 23(10):2893, 2005.

[33] Benjamin J. Puttnam, Georg Rademacher, and Ruben S. Luís. Space-division multiplexing for optical fiber communications. *Optica*, 8(9):1186–1203, Sep 2021.

[34] Antonio Napoli, Nicola Calabretta, Johannes K Fischer, Nelson Costa, Silvio Abrate, Joao Pedro, Victor Lopez, Vittorio Curri, Darko Zibar, Erwan Pincemin, et al. Perspectives of multi-band optical communication systems. In *2018 23rd Opto-Electronics and Communications Conference (OECC)*, pages 1–2. IEEE, 2018.

[35] René-Jean Essiambre, Gerhard Kramer, Peter J Winzer, Gerard J Foschini, and Bernhard Goebel. Capacity limits of optical fiber networks. *Journal of Lightwave Technology*, 28(4):662–701, 2010.

[36] Rachel Won. Is it crunch time? *Nature Photonics*, 9(7):424–426, 2015.

[37] Peter J Winzer. Scaling optical networking technologies for next generation sdm. In *2018 Optical Fiber Communications Conference and Exposition (OFC)*, pages 1–57. IEEE, 2018.

[38] Ioannis Tomkos, Siamak Azodolmolky, Josep Sole-Pareta, Davide Careglio, and Eleni Palkopoulou. A tutorial on the flexible optical networking paradigm: State of the art, trends, and research challenges. *Proceedings of the IEEE*, 102(9):1317–1337, 2014.

[39] Peter J Winzer. Scaling optical fiber networks: Challenges and solutions. *Optics and Photonics News*, 26(3):28–35, 2015.

[40] AD Ellis, N Mac Suibhne, D Saad, and DN Payne. Communication networks beyond the capacity crunch, 2016.

[41] Mable P Fok, Zhexing Wang, Yanhua Deng, and Paul R Prucnal. Optical layer security in fiber-optic networks. *IEEE Transactions on Information Forensics and Security*, 6(3):725–736, 2011.

[42] Jennifer Gossels, Gagan Choudhury, and Jennifer Rexford. Robust network design for ip/optical backbones. *Journal of Optical Communications and Networking*, 11(8):478–490, 2019.

[43] ITU Website. https://www.itu.int, 2023.

[44] IEEE Standards Association. https://standards.ieee.org, 2023.

[45] IETF Website. https://www.ietf.org/standards, 2023.

[46] OIF Website. https://www.oiforum.com, 2023.

[47] ONF Website. https://www.opennetworking.org, 2023.

[48] TIP Website. https://www.telecominfraproject.com, 2023.

[49] Open ROADM MSA Website. www.openroadm.org, 2023.

[50] OpenConfig Website. http://www.openconfig.net, 2023.

[51] Nick McKeown, Tom Anderson, Hari Balakrishnan, Guru Parulkar, Larry Peterson, Jennifer Rexford, Scott Shenker, and Jonathan Turner. Openflow: enabling innovation in campus networks. *ACM SIGCOMM computer communication review*, 38(2):69–74, 2008.

[52] M. Bjorklund. YANG - a data modeling language for the network configuration protocol (NETCONF). IETF RFC 6020.

[53] M. Dallaglio, N. Sambo, F. Cugini, and P. Castoldi. Control and management of transponders with NETCONF and YANG. *IEEE/OSA JOCN*, 9(3):B43–B52, March 2017.

[54] Enns, Rob and Bjorklund, Martin and Schoenwaelder, Juergen and Bierman, Andy. Network Configuration Protocol (NETCONF). Technical report, Internet Engineering Task Force, 2011.

[55] Bjorklund, Martin. YANG - A Data Modeling Language for the Network Configuration Protocol (NETCONF). Technical report, Internet Engineering Task Force, 2010.

[56] R. Enns, M. Bjorklund, J. Schoenwaelder, and A. Bierman. Network configuration protocol (NETCONF). IETF RFC 6241, June 2011.

[57] CFP MSA Implementation Agreement. https://www.cfp-msa.org, 2017.

[58] Quad Small Form-factor Pluggable (QSFP) Transceiver Specification. https://www.optcore.net/wp-content/uploads/2017/04/QSFP-MSA.pdf, 2006.

[59] OSFP MSA Implementation Agreement. https://osfpmsa.org/, 2018.

[60] QSFP-DD MSA Common Management Interface Specification. http://www.qsfp-dd.com/, 2018.

[61] OpenZR+ Implementation Agreement. https://openzrplus.org/, 2020.

[62] Ilya Lyubomirsky and Brian Taylor. An open approach for switching, routing, and transport. https://code.facebook.com/posts/1977308282496021/an-open-approach-for-switching-routing-and-transport/, 2016.

[63] Emilio Riccardi, Paul Gunning, Oscar González de Dios, Marco Quagliotti, Víctor López, and Andrew Lord. An operator view on the introduction of white boxes into optical networks. *Journal of Lightwave Technology*, 36(15):3062–3072, 2018.

[64] Thomas Barnett, Shruti Jain, Usha Andra, and Taru Khurana. Cisco visual networking index (vni) complete forecast update, 2017–2022. *Americas/EMEAR Cisco Knowledge Network (CKN) Presentation*, pages 1–30, 2018.

[65] Akhilesh S Thyagaturu, Anu Mercian, Michael P McGarry, Martin Reisslein, and Wolfgang Kellerer. Software defined optical networks (sdons): A comprehensive survey. *IEEE Communications Surveys & Tutorials*, 18(4):2738–2786, 2016.

[66] Juliver Gil Herrera and Juan Felipe Botero. Resource allocation in nfv: A comprehensive survey. *IEEE Transactions on Network and Service Management*, 13(3):518–532, 2016.

[67] Jon Matias, Jokin Garay, Nerea Toledo, Juanjo Unzilla, and Eduardo Jacob. Toward an sdn-enabled nfv architecture. *IEEE Communications Magazine*, 53(4):187–193, 2015.

[68] Diego Kreutz, Fernando MV Ramos, Paulo Esteves Verissimo, Christian Esteve Rothenberg, Siamak Azodolmolky, and Steve Uhlig. Software-defined networking: A comprehensive survey. *Proceedings of the IEEE*, 103(1):14–76, 2014.

[69] Doan B Hoang and Minh Pham. On software-defined networking and the design of sdn controllers. In *2015 6th International Conference on the Network of the Future (NOF)*, pages 1–3. IEEE, 2015.

[70] Siamak Azodolmolky, Reza Nejabati, Eduard Escalona, Ramanujam Jayakumar, Nikolaos Efstathiou, and Dimitra Simeonidou. Integrated openflow–gmpls control plane: an overlay model for software defined packet over optical networks. *Optics express*, 19(26):B421–B428, 2011.

[71] Ignacio Iglesias-Castreño, Miquel Garrich Alabarce, Manu Hernández-Bastida, and Pablo Pavón Mariño. Towards an open-source framework for jointly emulating control and data planes of disaggregated optical networks. In *2020 22nd International Conference on Transparent Optical Networks (ICTON)*, pages 1–4. IEEE, 2020.

[72] Pankaj Berde, Matteo Gerola, Jonathan Hart, Yuta Higuchi, Masayoshi Kobayashi, Toshio Koide, Bob Lantz, Brian O'Connor, Pavlin Radoslavov, William Snow, et al. Onos: towards an open, distributed sdn os. In *Proceedings of the third workshop on Hot topics in software defined networking*, pages 1–6, 2014.

[73] Jan Medved, Robert Varga, Anton Tkacik, and Ken Gray. Opendaylight: Towards a model-driven sdn controller architecture. In *Proceeding of IEEE international symposium on a world of wireless, mobile and multimedia networks 2014*, pages 1–6. IEEE, 2014.

[74] Takeshi Hoshida, Vittorio Curri, Lidia Galdino, David T Neilson, Wladek Forysiak, Johannes K Fischer, Tomoyuki Kato, and Pierluigi Poggiolini. Ultrawideband systems and networks: Beyond c+ l-band. *Proceedings of the IEEE*, 110(11):1725–1741, 2022.

[75] Ori Gerstel, Masahiko Jinno, Andrew Lord, and SJ Ben Yoo. Elastic optical networking: A new dawn for the optical layer? *IEEE communications Magazine*, 50(2):s12–s20, 2012.

[76] Bijoy Chand Chatterjee, Nityananda Sarma, and Eiji Oki. Routing and spectrum allocation in elastic optical networks: A tutorial. *IEEE Communications Surveys & Tutorials*, 17(3):1776–1800, 2015.

[77] Luis Velasco, Alba P Vela, Fernando Morales, and Marc Ruiz. Designing, operating, and reoptimizing elastic optical networks. *Journal of Lightwave Technology*, 35(3):513–526, 2016.

[78] Mattia Cantono. *Physical layer aware optical networks*. PhD thesis, Politecnico di Torino Turin, Italy, 2018.

[79] Georgios S Zervas and Dimitra Simeonidou. Cognitive optical networks: Need, requirements and architecture. In *2010 12th International Conference on Transparent Optical Networks*, pages 1–4. IEEE, 2010.

[80] Wei Wei, Chonggang Wang, and Jianjun Yu. Cognitive optical networks: key drivers, enabling techniques, and adaptive bandwidth services. *IEEE Communications magazine*, 50(1):106–113, 2012.

[81] Vincent W. S. Chan. Cognitive optical networks. In *2018 IEEE International Conference on Communications (ICC)*, pages 1–6, 2018.

[82] Ignacio de Miguel, Ramón J. Durán, Tamara Jiménez, Natalia Fernández, Juan Carlos Aguado, Rubén M. Lorenzo, Antonio Caballero, Idelfonso Tafur Monroy, Yabin Ye, Andrzej Tymecki, Ioannis Tomkos, Marianna Angelou, Dimitrios Klonidis, Antonio Francescon, Domenico Siracusa, and Elio Salvadori. Cognitive dynamic optical networks [invited]. *J. Opt. Commun. Netw.*, 5(10):A107–A118, Oct 2013.

[83] Francesco Paolucci and Andrea Sgambelluri. Telemetry in disaggregated optical networks. In *2020 International Conference on Optical Network Design and Modeling (ONDM)*, pages 1–3. IEEE, 2020.

[84] Byrav Ramamurthy, Helena Feng, Debasish Datta, Jonathan P Heritage, and Biswanath Mukherjee. Transparent vs. opaque vs. translucent wavelength-routed optical networks. In *OFC/IOOC. Technical Digest. Optical Fiber Communication Conference, 1999, and the International Conference on Integrated Optics and Optical Fiber Communication*, volume 1, pages 59–61. IEEE, 1999.

[85] Dominic A Schupke and Didier Sellier. Lightpath configuration of transparent and static wdm networks for ip traffic. In *ICC 2001. IEEE International Conference on Communications. Conference Record (Cat. No. 01CH37240)*, volume 2, pages 494–498. IEEE, 2001.

[86] Nicola Sambo, Yvan Pointurier, Filippo Cugini, Luca Valcarenghi, Piero Castoldi, and Ioannis Tomkos. Lightpath establishment assisted by offline qot estimation in transparent optical networks. *Journal of Optical Communications and Networking*, 2(11):928–937, 2010.

[87] Mark Filer, Mattia Cantono, Alessio Ferrari, Gert Grammel, Gabriele Galimberti, and Vittorio Curri. Multi-vendor experimental validation of an open source qot estimator for optical networks. *Journal of Lightwave Technology*, 36(15):3073–3082, 2018.

[88] Vittorio Curri. Gnpy model of the physical layer for open and disaggregated optical networking. *Journal of optical communications and networking*, 14(6):C92–C104, 2022.

[89] G Bosco, A Carena, V Curri, P Poggiolini, E Torrengo, and F Forghieri. Investigation on the robustness of a nyquist-wdm terabit superchannel to transmitter and receiver non-idealities. In *36th European Conference and Exhibition on Optical Communication*, pages 1–3. IEEE, 2010.

[90] Maxim Kuschnerov, Fabian N Hauske, Kittipong Piyawanno, Bernhard Spinnler, Mohammad S Alfiad, Antonio Napoli, and Berthold Lankl. Dsp for coherent single-carrier receivers. *Journal of lightwave technology*, 27(16):3614–3622, 2009.

[91] Yvan Pointurier. Design of low-margin optical networks. *Journal of Optical Communications and Networking*, 9(1):A9–A17, 2017.

[92] Danshi Wang, Zhiguo Zhang, Min Zhang, Meixia Fu, Jin Li, Shanyong Cai, Chunyu Zhang, and Xue Chen. The role of digital twin in optical communication: fault management, hardware configuration, and transmission simulation. *IEEE Communications Magazine*, 59(1):133–139, 2021.

[93] Ricard Vilalta, Ramon Casellas, Ll Gifre, Raul Muñoz, Ricardo Martínez, A Pastor, D López, and JP Fernández-Palacios. Architecture to deploy and operate a digital twin optical network. In *Optical Fiber Communication Conference*, pages W1F–4. Optica Publishing Group, 2022.

[94] Giacomo Borraccini, Renato Ambrosone, Alessio Giorgetti, Stefano Straullu, Francesco Aquilino, Emanuele Virgillito, Andrea D'Amico, Rocco D'Ingillo, Nicola Sambo, Filippo Cugini, et al. Disaggregated optical network orchestration based on the physical layer digital twin. In *2023 Optical Fiber Communications Conference and Exhibition (OFC)*, pages 1–3. IEEE, 2023.

[95] Jin Li, Danshi Wang, Min Zhang, and Siheng Cui. Digital twin-enabled self-evolved optical transceiver using deep reinforcement learning. *Optics Letters*, 45(16):4654–4657, 2020.

[96] Alessio Ferrari, Mark Filer, Karthikeyan Balasubramanian, Yawei Yin, Esther Le Rouzic, Jan Kundrát, Gert Grammel, Gabriele Galimberti, and Vittorio Curri. Gnpy: an open source application for physical layer aware open optical networks. *Journal of Optical Communications and Networking*, 12(6):C31–C40, 2020.

[97] Andrea D'Amico, Elliot London, Bertrand Le Guyader, Florian Frank, Esther Le Rouzic, Erwan Pincemin, Nicolas Brochier, and Vittorio Curri. Experimental validation of gnpy in a multi-vendor flex-grid flex-rate wdm optical transport scenario. *Journal of Optical Communications and Networking*, 14(3):79–88, 2022.

[98] Mohammed N Islam. Raman amplifiers for telecommunications. *IEEE Journal of selected topics in Quantum Electronics*, 8(1):548–559, 2002.

[99] Jake Bromage. Raman amplification for fiber communications systems. *Journal of Lightwave Technology*, 22(2):79, 2004.

[100] Vittorio Curri. System advantages of raman amplifiers. *Proc. NFOEC 2000*, 1:35–46, 2000.

[101] Vittorio Curri and Andrea Carena. Merit of raman pumping in uniform and uncompensated links supporting nywdm transmission. *Journal of Lightwave Technology*, 34(2):554–565, 2015.

[102] Wayne S Pelouch. Raman amplification: An enabling technology for long-haul coherent transmission systems. *Journal of Lightwave Technology*, 34(1):6–19, 2015.

[103] Mingming Tan, Paweł Rosa, Son Thai Le, Ian D Phillips, and Paul Harper. Evaluation of 100g dp-qpsk long-haul transmission performance using second order co-pumped raman laser based amplification. *Optics express*, 23(17):22181–22189, 2015.

[104] Shu Namiki and Yoshihiro Emori. Ultrabroad-band raman amplifiers pumped and gain-equalized by wavelength-division-multiplexed high-power laser diodes. *IEEE Journal of Selected Topics in Quantum Electronics*, 7(1):3–16, 2001.

[105] Victor E Perlin and Herbert G Winful. On distributed raman amplification for ultrabroad-band long-haul wdm systems. *Journal of lightwave technology*, 20(3):409, 2002.

[106] Andrea Carena, Vittorio Curri, and Pierluigi Poggiolini. On the optimization of hybrid raman/erbium-doped fiber amplifiers. *IEEE Photonics Technology Letters*, 13(11):1170–1172, 2001.

[107] Tiejun J Xia, Herve Fevrier, Ting Wang, and Toshio Morioka. Introduction of spectrally and spatially flexible optical networks. *IEEE Communications Magazine*, 53(2):24–33, 2015.

[108] M-S Kao and Jingshown Wu. Signal light amplification by stimulated raman scattering in an n-channel wdm optical fiber communication system. *Journal of lightwave Technology*, 7(9):1290–1299, 1989.

[109] Y Emori, K Tanaka, and S Namiki. 100 nm bandwidth flat-gain raman amplifiers pumped and gain-equalised by 12-wavelength-channel wdm laser diode unit. *Electronics Letters*, 35(16):1355–1356, 1999.

[110] Victor E Perlin and Herbert G Winful. Optimal design of flat-gain wide-band fiber raman amplifiers. *Journal of lightwave technology*, 20(2):250, 2002.

[111] Xueming Liu and Yanhe Li. Optimizing the bandwidth and noise performance of distributed multi-pump raman amplifiers. *Optics communications*, 230(4-6):425–431, 2004.

[112] B Neto, AL J Teixeira, N Wada, and PS André. Efficient use of hybrid genetic algorithms in the gain optimization of distributed raman amplifiers. *Optics express*, 15(26):17520–17528, 2007.

[113] Xiaoxue Zhao, Vijay Vusirikala, Bikash Koley, Valey Kamalov, and Tad Hofmeister. The prospect of inter-data-center optical networks. *IEEE Communications Magazine*, 51(9):32–38, 2013.

[114] Xiaoxue Zhao, Vijay Vusirikala, Bikash Koley, Tad Hofmeister, Valey Kamalov, and Vinayak Dangui. Optical transport sdn for high-capacity inter-datacenter networks. In *Photonics in Switching*, pages PM3C–1. Optical Society of America, 2014.

[115] Antonio Caballero, Robert Borkowski, Darko Zibar, and Idelfonso Tafur Monroy. Performance monitoring techniques supporting cognitive optical networking. In *2013 15th International Conference on Transparent Optical Networks (ICTON)*, pages 1–4. IEEE, 2013.

[116] Robert Borkowski, Ramon J Duran, Christoforos Kachris, Domenico Siracusa, Antonio Caballero, Natalia Fernandez, Dimitrios Klonidis, Antonio Francescon, Tamara Jimenez, Juan Carlos Aguado, et al. Cognitive optical network testbed: Eu project chron. *Journal of Optical Communications and Networking*, 7(2):A344–A355, 2015.

[117] Darko Zibar, A Ferrari, V Curri, and A Carena. Machine learning-based raman amplifier design. In *Optical Fiber Communication Conference*, pages M1J–1. Optical Society of America, 2019.

[118] Darko Zibar, Ann Margareth Rosa Brusin, Uiara Celine Moura, Vittorio Curri, and Andrea Carena. Inverse system design using machine learning: the raman amplifier case. *Journal of Lightwave Technology*, 2019.

[119] A Margareth Rosa Brusin, Uiara C De Moura, Andrea D'Amico, Vittorio Curri, Darko Zibar, and Andrea Carena. Load aware raman gain profile prediction in dynamic multi-band optical networks. In *2020 Optical Fiber Communications Conference and Exhibition (OFC)*, pages 1–3. IEEE, 2020.

[120] Uiara C de Moura, Darko Zibar, A Margareth Rosa Brusin, Andrea Carena, and Francesco Da Ros. Fiber-agnostic machine learning-based raman amplifier models. *Journal of Lightwave Technology*, 41(1):83–95, 2022.

[121] Uiara C de Moura, Francesco Da Ros, A Margareth Rosa Brusin, Andrea Carena, and Darko Zibar. Experimental characterization of raman amplifier optimization through inverse system design. *Journal of Lightwave Technology*, 39(4):1162–1170, 2020.

[122] Uiara Celine De Moura, Md Asif Iqbal, Morteza Kamalian, Lukasz Krzczanowicz, Francesco Da Ros, Ann Margareth Rosa Brusin, Andrea Carena, Wladek Forysiak, Sergei Turitsyn, and Darko Zibar. Multi–band programmable gain raman amplifier. *Journal of Lightwave Technology*, 39(2):429–438, 2020.

[123] Giacomo Borraccini, Stefano Straullu, Alessio Ferrari, Stefano Piciaccia, Gabriele Galimberti, and Vittorio Curri. Flexible and autonomous multi-band raman amplifiers. In *2020 IEEE Photonics Conference (IPC)*, pages 1–2. IEEE, 2020.

[124] Giacomo Borraccini, Alessio Ferrari, Stefano Straullu, Antonino Nespola, Andrea D'Amico, Stefano Piciaccia, Gabriele Galimberti, Alberto Tanzi, Silvia Turolla, and Vittorio Curri. Softwarized and autonomous raman amplifiers in multi-band open optical networks. In *2020 International Conference on Optical Network Design and Modeling (ONDM)*, pages 1–6. IEEE, 2020.

[125] Giacomo Borraccini, Stefano Staullu, Alessio Ferrari, Stefano Piciaccia, Gabriele Galimberti, Alberto Tanzi, and Vittorio Curri. Autonomous raman amplifiers in software-defined optical transport networks. In *GLOBECOM 2020-2020 IEEE Global Communications Conference*, pages 1–6. IEEE, 2020.

[126] Giacomo Borraccini, Stefano Straullu, Stefano Piciaccia, Alberto Tanzi, Antonino Nespola, Gabriele Galimberti, and Vittorio Curri. Autonomous raman amplifiers using standard integrated network equipment. *IEEE Photonics Technology Letters*, 33(16):868–871, 2021.

[127] Giacomo Borraccini, Stefano Straullu, Andrea D'Amico, Antonino Nespola, Stefano Piciaccia, Alberto Tanzi, Gabriele Galimberti, and Vittorio Curri. Autonomous raman amplifiers in multi-band software-defined optical transport networks. *Journal of Optical Communications and Networking*, 13(10):E53–E62, 2021.

[128] Giacomo Borraccini, Stefano Straullu, Stefano Piciaccia, Alberto Tanzi, Gabriele Galimberti, and Vittorio Curri. Cognitive raman amplifier control using an evolutionary optimization strategy. *IEEE Photonics Technology Letters*, 34(4):223–226, 2022.

[129] Salim Tariq and Joseph C Palais. A computer model of non-dispersion-limited stimulated raman scattering in optical fiber multiple-channel communications. *Journal of lightwave technology*, 11(12):1914–1924, 1993.

[130] Govind Agrawal. *Nonlinear Fiber Optics*. Academic Press, Boston, fifth edition, 2013.

[131] Andrea D'Amico, Bruno Correia, Elliot London, Emanuele Virgillito, Giacomo Borraccini, Antonio Napoli, and Vittorio Curri. Scalable and disaggregated ggn approximation applied to a c+l+s optical network. *J. Lightwave Technol.*, 40(11):3499–3511, Jun 2022.

[132] Tingye Li. *Optical fiber communications: fiber fabrication*. Elsevier, 2012.

[133] S Walker. Rapid modeling and estimation of total spectral loss in optical fibers. *J. Lightw. Technol.*, 4(8):1125–1131, 8 1986.

[134] Erwan Pincemin, Didier Grot, Laurence Bathany, Stéphane Gosselin, Michel Joindot, Sylvain Bordais, Yves Jaouen, and Jean-Marc Delavaux. Raman gain efficiencies of modern terrestrial transmission fibers in S-, C-and L-band. In *Nonlinear Guided Waves and Their Applications*, page NLTuC2. Optical Society of America, 2002.

[135] Karsten Rottwitt, Jake Bromage, Andrew J Stentz, Lufeng Leng, Malcolm E Lines, and Henrik Smith. Scaling of the Raman gain coefficient: applications to germanosilicate fibers. *Journal of lightwave technology*, 21(7):1652, 2003.

[136] Pauli Virtanen, Ralf Gommers, Travis E. Oliphant, Matt Haberland, Tyler Reddy, David Cournapeau, Evgeni Burovski, Pearu Peterson, Warren Weckesser, Jonathan Bright, Stéfan J. van der Walt, Matthew Brett, Joshua Wilson, K. Jarrod Millman, Nikolay Mayorov, Andrew R. J. Nelson, Eric Jones, Robert Kern, Eric Larson, C J Carey, İlhan Polat, Yu Feng, Eric W. Moore, Jake VanderPlas, Denis Laxalde, Josef Perktold, Robert Cimrman, Ian Henriksen, E. A. Quintero, Charles R. Harris, Anne M. Archibald, Antônio H. Ribeiro, Fabian Pedregosa, Paul van Mulbregt, and SciPy 1.0 Contributors. SciPy 1.0: Fundamental Algorithms for Scientific Computing in Python. *Nature Methods*, 17:261–272, 2020.

[137] Jake Bromage, Karsten Rottwitt, and ME Lines. A method to predict the raman gain spectra of germanosilicate fibers with arbitrary index profiles. *IEEE Photonics Technology Letters*, 14(1):24–26, 2002.

[138] PB Hansen, L Eskildsen, J Stentz, TA Strasser, J Judkins, JJ DeMarco, R Pedrazzani, and DJ DiGiovanni. Rayleigh scattering limitations in distributed raman pre-amplifiers. *IEEE Photonics Technology Letters*, 10(1):159–161, 1998.

[139] Nikolaus Hansen, Youhei Akimoto, and Petr Baudis. CMA-ES/pycma on Github. Zenodo, DOI:10.5281/zenodo.2559634, February 2019.

[140] Giacomo Borraccini, Andrea D'Amico, Stefano Straullu, Antonino Nespola, Stefano Piciaccia, Alberto Tanzi, Gabriele Galimberti, Stefano Bottacchi, Scott Swail, and Vittorio Curri. Cognitive and autonomous qot-driven optical line controller. *Journal of Optical Communications and Networking*, 13(10):E23–E31, 2021.

[141] Giacomo Borraccini, Stefano Straullu, Alessio Ferrari, Emanuele Virgillito, Stefano Bottacchi, Scott Swail, Stefano Piciaccia, Gabriele Galimberti, Gert Grammel, and Vittorio Curri. Using qot-e for open line controlling and modulation format deployment: an experimental proof of concept. In *2020 European Conference on Optical Communications (ECOC)*, pages 1–4. IEEE, 2020.

[142] Giacomo Borraccini, Stefano Straullu, Andrea D'Amico, Emanuele Virgillito, Lalit Kumar, Stefano Piciaccia, Stefano Bottacchi, Scott Swail, Gabriele Galimberti, and Vittorio Curri. Qot-e driven optimized amplifier control in disaggregated optical networks. In *2021 Optical Fiber Communications Conference and Exhibition (OFC)*, pages 1–3. IEEE, 2021.

[143] Giacomo Borraccini, Stefano Straullu, Andrea D'Amico, Antonino Nespola, Stefano Piciaccia, Alberto Tanzi, Gabriele Galimberti, and Vittorio Curri. Autonomous physical layer characterization in cognitive optical line systems. In *2021 Optical Fiber Communications Conference and Exhibition (OFC)*, pages 1–3. IEEE, 2021.

[144] Giacomo Borraccini, Andrea D'Amico, Stefano Straullu, Fehmida Usmani, Arsalan Ahmad, and Vittorio Curri. Iterative supervised learning approach using transceiver bit-error-rate measurements for optical line system optimization. *Journal of Optical Communications and Networking*, 15(2):111–118, 2023.

[145] Giacomo Borraccini, Andrea D'Amico, Stefano Straullu, Francesco Aquilino, Stefano Piciaccia, Alberto Tanzi, Gabriele Galimberti, and Vittorio Curri. Local vs. global optimization for optical line system control in disaggregated networks. In *2023 International Conference on Optical Network Design and Modeling (ONDM)*, pages 1–3. IEEE, 2023.

[146] Andrea D'Amico, Giacomo Borraccini, Stefano Straullu, Francesco Aquilino, Stefano Piciaccia, Alberto Tanzi, Gabriele Galimberti, and Vittorio Curri. Experimental probing and modeling of the pdl impact on the optical signal-to-noise ratio. In *Optical Fiber Communication Conference*, pages W1E–6. Optica Publishing Group, 2023.

[147] Talha Rahman, Antonio Napoli, Danish Rafique, Bernhard Spinnler, Maxim Kuschnerov, Iveth Lobato, Benoit Clouet, Marc Bohn, Chigo Okonkwo, and Huug de Waardt. On the mitigation of optical filtering penalties originating from roadm cascade. *IEEE Photonics Technology Letters*, 26(2):154–157, 2013.

[148] Ezra Ip and Joseph M Kahn. Digital equalization of chromatic dispersion and polarization mode dispersion. *Journal of Lightwave Technology*, 25(8):2033–2043, 2007.

[149] Govind P Agrawal. *Fiber-optic communication systems*. John Wiley & Sons, 2012.

[150] Emmanuel Desurvire. Analysis of noise figure spectral distribution in erbium doped fiber amplifiers pumped near 980 and 1480 nm. *Applied optics*, 29(21):3118–3125, 1990.

[151] Emmanuel Desurvire and Michael N Zervas. Erbium-doped fiber amplifiers: principles and applications. *Physics Today*, 48(2):56–58, 1995.

[152] Emmanuel Desurvire, Jay R Simpson, and PC Becker. High-gain erbium-doped traveling-wave fiber amplifier. *Optics letters*, 12(11):888–890, 1987.

[153] M Birk, AK Srivastava, G Wilson, J Ye, L Chen, Y Cao, I White, P Lu, M Santo, A Carra, et al. System margin enhancement in terabit capacity 40 gb/s systems using an integrated edfa with dynamic gain equalizer. In *Optical Fiber Communication Conference*, page ThGG101. Optica Publishing Group, 2002.

[154] Douglas M Baney, Philippe Gallion, and Rodney S Tucker. Theory and measurement techniques for the noise figure of optical amplifiers. *Optical fiber technology*, 6(2):122–154, 2000.

[155] Ankush Mahajan, Konstantinos Christodoulopoulos, Ricardo Martínez, Salvatore Spadaro, and Raul Muñoz. Modeling edfa gain ripple and filter penalties with machine learning for accurate qot estimation. *Journal of Lightwave Technology*, 38(9):2616–2629, 2020.

[156] Metodi Plamenov Yankov, Pawel Marcin Kaminski, Henrik Enggaard Hansen, and Francesco Da Ros. Snr optimization of multi-span fiber optic communication systems employing edfas with non-flat gain and noise figure. *Journal of Lightwave Technology*, 39(21):6824–6832, 2021.

[157] Dag Bonnedal. Edfa gain described with a black box model. In *Optical Amplifiers and Their Applications*, page FAW4. Optica Publishing Group, 1996.

[158] John Kerr. Xl. a new relation between electricity and light: Dielectrified media birefringent. *The London, Edinburgh, and Dublin Philosophical Magazine and Journal of Science*, 50(332):337–348, 1875.

[159] John Kerr. Liv. a new relation between electricity and light: Dielectrified media birefringent (second paper). *The London, Edinburgh, and Dublin Philosophical Magazine and Journal of Science*, 50(333):446–458, 1875.

[160] Govind P Agrawal. Nonlinear fiber optics. In *Nonlinear Science at the Dawn of the 21st Century*, pages 195–211. Springer, 2000.

[161] Andrea D'Amico, Bruno Correia, Elliot London, Emanuele Virgillito, Giacomo Borraccini, Antonio Napoli, and Vittorio Curri. Scalable and disaggregated ggn approximation applied to a c+ l+ s optical network. *Journal of Lightwave Technology*, 40(11):3499–3511, 2022.

[162] Pierluigi Poggiolini. The gn model of non-linear propagation in uncompensated coherent optical systems. *Journal of Lightwave Technology*, 30(24):3857–3879, 2012.

[163] Ian Roberts, Joseph M Kahn, James Harley, and David W Boertjes. Channel power optimization of wdm systems following gaussian noise nonlinearity model in presence of stimulated raman scattering. *Journal of Lightwave Technology*, 35(23):5237–5249, 2017.

[164] Daniel Semrau, Robert I Killey, and Polina Bayvel. The gaussian noise model in the presence of inter-channel stimulated raman scattering. *Journal of Lightwave Technology*, 36(14):3046–3055, 2018.

[165] Dany-Sebastien Ly-Gagnon, Satoshi Tsukamoto, Kazuhiro Katoh, and Kazuro Kikuchi. Coherent detection of optical quadrature phase-shift keying signals with carrier phase estimation. *Journal of lightwave technology*, 24(1):12, 2006.

[166] Seb J Savory. Digital coherent optical receivers: Algorithms and subsystems. *IEEE Journal of selected topics in quantum electronics*, 16(5):1164–1179, 2010.

[167] Michael G Taylor. Coherent detection method using dsp for demodulation of signal and subsequent equalization of propagation impairments. *IEEE Photonics Technology Letters*, 16(2):674–676, 2004.

[168] Georgios Tzimpragos, Christoforos Kachris, Ivan B Djordjevic, Milorad Cvijetic, Dimitrios Soudris, and Ioannis Tomkos. A survey on fec codes for 100 g and beyond optical networks. *IEEE Communications Surveys & Tutorials*, 18(1):209–221, 2014.

[169] Loren Berg. Demystifying transceiver and line characterization metrics. In *Optical Fiber Communication Conference*, pages W4H–3. Optical Society of America, 2019.

[170] Toru Mano, Andrea D'Amico, Emanuele Virgillito, Giacomo Borraccini, Yue-Kai Huang, Kei Kitamura, Kazuya Anazawa, Akira Masuda, Hideki Nishizawa, Ting Wang, et al. Accuracy of nonlinear interference estimation on launch power optimization in short-reach systems with field trial. In *2022 European Conference on Optical Communication (ECOC)*, pages 1–4. IEEE, 2022.

[171] Toru Mano, Andrea D'Amico, Emanuele Virgillito, Giacomo Borraccini, Yue-Kai Huang, Kazuya Anazawa, Hideki Nishizawa, Ting Wang, Koji Asahi, and Vittorio Curri. Modeling transceiver ber-osnr characteristic for qot estimation in short-reach systems. In *2023 International Conference on Optical Network Design and Modeling (ONDM)*, pages 1–3. IEEE, 2023.

[172] Andrea D'Amico, Le Guyader, Florian Frank, Esther Le Rouzic, Erwan Pincemin, Antonio Napoli, Han Sun, Bernhard Spinnler, Nicolas Brochier, and Vittorio Curri. Gnpy experimental validation for nyquist subcarriers flexible transmission up to 800 g. In *2022 Optical Fiber Communications Conference and Exhibition (OFC)*, pages 1–3. IEEE, 2022.

[173] A. Ferrari, K. Balasubramanian, M. Filer, Y. Yin, E. le Rouzic, J. Kundrát, G. Grammel, G. Galimberti, and V. Curri. Softwarized optical transport qot in production optical network: a brownfield validation. In *2020 European Conference on Optical Communications (ECOC)*, pages 1–4, 2020.

[174] Nikolaus Hansen, Sibylle D Müller, and Petros Koumoutsakos. Reducing the time complexity of the derandomized evolution strategy with covariance matrix adaptation (cma-es). *Evolutionary computation*, 11(1):1–18, 2003.

[175] Pierluigi Poggiolini, G Bosco, A Carena, R Cigliutti, V Curri, F Forghieri, R Pastorelli, and S Piciaccia. The logon strategy for low-complexity control plane implementation in new-generation flexible networks. In *2013 Optical Fiber Communication Conference and Exposition and the National Fiber Optic Engineers Conference (OFC/NFOEC)*, pages 1–3. IEEE, 2013.

[176] Vittorio Curri, Andrea Carena, Andrea Arduino, Gabriella Bosco, Pierluigi Poggiolini, Antonino Nespola, and Fabrizio Forghieri. Design strategies and merit of system parameters for uniform uncompensated links supporting nyquist-wdm transmission. *Journal of Lightwave Technology*, 33(18):3921–3932, 2015.

[177] Yuren You, Zhiping Jiang, and Christopher Janz. Machine learning-based edfa gain model. In *2018 European Conference on Optical Communication (ECOC)*, pages 1–3. IEEE, 2018.

[178] Jiakai Yu, Shengxiang Zhu, Craig L Gutterman, Gil Zussman, and Daniel C Kilper. Machine-learning-based edfa gain estimation. *Journal of Optical Communications and Networking*, 13(4):B83–B91, 2021.

[179] https://www.tensorflow.org/.

[180] Maxim Bolshtyansky. Spectral hole burning in erbium-doped fiber amplifiers. *Journal of lightwave technology*, 21(4):1032–1038, 2003.

[181] Giacomo Borraccini, Stefano Straullu, Alessio Giorgetti, Rocco D'Ingillo, Davide Scano, Andrea D'Amico, Emanuele Virgillito, Antonino Nespola, Nicola Sambo, Filippo Cugini, et al. Qot-driven optical control and data plane in multi-vendor disaggregated networks. In *Optical Fiber Communication Conference*, pages M4F–5. Optica Publishing Group, 2022.

[182] Giacomo Borraccini, Stefano Straullu, Alessio Giorgetti, Renato Ambrosone, Emanuele Virgillito, Andrea D'Amico, Rocco D'Ingillo, Francesco Aquilino, Antonino Nespola, Nicola Sambo, et al. Experimental demonstration of

partially disaggregated optical network control using the physical layer digital twin. *arXiv preprint arXiv:2212.11874*, 2022.

[183] Giacomo Borraccini, Renato Ambrosone, Alessio Giorgetti, Stefano Straullu, Francesco Aquilino, Emanuele Virgillito, Andrea D'Amico, Rocco D'Ingillo, Nicola Sambo, Filippo Cugini, et al. Disaggregated optical network orchestration based on the physical layer digital twin. In *Optical Fiber Communication Conference*, pages Tu3D–4. Optica Publishing Group, 2023.

[184] Quan Pham-Van, Victor López, Arturo Mayoral Lopez-de Lerma, Rafał Szwedowski, Konrad Mrówka, Sebastian Auer, Huu-Trung Thieu, Quang-Huy Tran, Dominique Verchere, Gary Atkinson, et al. Demonstration of alarm correlation in partially disaggregated optical networks. In *Optical Fiber Communication Conference*, pages M3Z–6. Optica Publishing Group, 2020.

[185] Andrea D'Amico, Stefano Straullu, Giacomo Borraccini, Elliot London, Stefano Bottacchi, Stefano Piciaccia, Alberto Tanzi, Antonino Nespola, Gabriele Galimberti, Scott Swail, and Vittorio Curri. Enhancing lightpath qot computation with machine learning in partially disaggregated optical networks. *IEEE Open Journal of the Communications Society*, 2:564–574, 2021.

[186] Open Optical & Packet Transport (OOPT). https://telecominfraproject.com/open-optical-packet-transport, 2021.

[187] Alessio Giorgetti, Andrea Sgambelluri, Ramon Casellas, Roberto Morro, Andrea Campanella, and Piero Castoldi. Control of open and disaggregated transport networks using the open network operating system (ONOS). *Journal of Optical Communications and Networking*, 12(2):A171–A181, 2020.

[188] Victor E Perlin and Hervert G Winful. Optimizing the noise performance of broad-band wdm systems with distributed raman amplification. *IEEE Photonics Technology Letters*, 14(8):1199–1201, 2002.